QUANTUM CHAOS WITH A BOSE-EINSTEIN CONDENSATE

By

GHAZAL BEHIN AEIN

Bachelor of Science
SHIRAZ University
Shiraz, Iran
1996

Submitted to the Faculty of the
Graduate College of the
Oklahoma State University
in partial fulfillment of
the requirements for
the Degree of
DOCTOR OF PHILOSOPHY
July, 2007

QUANTUM CHAOS WITH A BOSE-EINSTEIN CONDENSATE

Thesis Approved:

Dr. Gil Summy

Thesis Advisor

Dr. G. Agarwal

Dr. X. Xie

Dr. A. Cheville

Dr. A. Gordon Emslie

Dean of the Graduate College

ACKNOWLEDGMENTS

I would like to thank my advisor Dr. Gil Summy. Gil is a remarkable individual who has the rare ability among physicists to create an atmosphere where students are intrigued to do great physics as well as have a life, as impossible as that may seem. Learning physics and doing research along side Gil has been a great opportunity. He is an exceptional scientist with great insight whom when discussing scientific matters, sees you as an equal giving you the freedom to explore and the surest chance to genuinely learn.

During the past four years I have worked with Brian, Peyman, Vijay, and recently Ishan, in the lab. Brian is the go to guy with anything technical. Needless to say that's why he silently retreated to two floors above us when it was apparent he couldn't write a single sentence of his thesis due to our constant questions, all of which he patiently replied to. Although I might add that only put him through the trouble of having to walk up and down the stairs, we have a notoriously slow elevator. Vijay must be one of the most patient and persistent people I have ever met when it comes to doing an experiment. Nothing seems to bother him, no matter how many times for whatever bizarre reason we had to redo things or whatever broke down or what ever result we weren't getting he kept his cool while I was eating myself up. I didn't get a chance to work with Ishan that much but his up tone mood was a nice addition to our underground bunker. Last but not the least is Peyman, who is also my significant other. And believe it or not we actually enjoy seeing each other 24/7, at least that's the story we're sticking to. Brian and he set up the experiment and the rest of us naturally reaped the best of their efforts. Peyman is very enthusiastic about his research and his vast knowledge accompanied by his continuous readiness

to explain anything to you, even for the tenth time, even if you aren't his wife, was and is a true blessing.

The Physics department at Oklahoma State University has unique group of people. All of which are always trying to help the students in anyway they can. The faculty, with their dedication to the educational growth of their students and the staff with almost every other request the students have, even when it's not their job. I still believe that Susan, Cindy, and Stephanie are among the nicest people you can ever hope to work with. Their office is a frequent refuge for the stressed out physics students and if you just step inside the office and say hi, you'll understand why. And of course Warren our technician who provides the graduate students with a multitude of services is not forgotten. We are also lucky to have a great group working in our machine shop led by Mike Lucas who along with his skills, his creativity has helped build many needed equipment.

I would like to make a special note to our graduate coordinator, Professor Paul Westhaus for the unlimited support he provides for the graduate students. Coming to the US as an international student, it is a true blessing to be welcomed by someone as patient, helpful, and welcoming as Paul Westhaus.

I would like to acknowledge the contribution of my dissertation committee members which includes: Dr. G. Summy, Dr. G. Agarwal, Dr. X. Xie, Dr. A. Cheville.

I would like to thank all of the above people and all my fellow graduate students that I hope to preserve my friendship with for making the the past seven years (yeah it took that long!), an experience that will remain in my memory as one of the toughest and nicest.

In the end I would like to again give a special thanks to Peyman for his support, love and enduring patience with me. I am very grateful for having him in my life.

TABLE OF CONTENTS

LIST OF FIGURES

CHAPTER 1

INTRODUCTION

"The very first of all, **CHOAS** came into being." Hesiod, *Theogeny* 116

In July 1687 the first complete edition of Newton's *Principia* was published. In these books Newton managed to formulate the science of mechanics in terms of just three basic laws. He also included a systematic mathematical framework for exploring the implications of these laws. With the advent of this work science began an exponential growth, with scientists having a tool to predict the behavior of mechanical objects. Newton's laws were such a success that the overriding view of every phenomena occurring in nature became one which was inherently deterministic. Although Newton's equations are the correct starting point of mechanics, in general they only allow for predicting long time behavior of *integrable* mechanical systems. Unfortunately nature does not contain many of examples like this, and so for the most part, Newton's laws are useful in only predicting the short time behavior of a system.

Maybe more than anything else it was hoped that Newton's laws be able to help understand the solar system. Questions of the stability and evolution of the solar system have been circling in the scientific community for a long time. Its apparent clock-like regularity and the accuracy with which the planetary motions could be computed attracted the curiosity of many scientist and led to the question of the stability of the solar system. The question was so pressing that in 1885 as part of a contest organized by Mittag-Leffler, in honor of King Oscar II of Sweden and Norway, Weierstrass posed a question for which the answer could potentially solve the stability problem. The question reads as follows "*For an arbitrary system of mass points* *which attract each other according to Newton's laws, assuming that no two points ever collide, give the coordinates of the individual points for all time as the sum of a uniformly convergent series whose terms are made up of known functions*" [1]. At the time, Newtonian mechanics was still giving an accurate description of the motion of the bodies in the solar system. The discovery of Neptune was prompted by an attempt to explain a discrepancy between the predicted and observed trajectories of Uranus. Although solving the problem of the dynamics of three gravitationally interacting bodies even today is not analytically possible in a general form, many predictions of planetary locations were performed by considering only the interaction of each planet with the sun, and then taking into account the perturbations due to the interactions of the planets with each other. Henry Poincaré entered the contest and won the prize for solving the problem twice. He first submitted a complex and innovative entry that demonstrated the stability in the three-body problem and claimed the winning entry. After its publication it was pointed out that Poincaré had made a significant error in his proof. Mittag-Leffler gave a dramatic response, requiring that every copy of the *Acta Mathematica* where the proof had appeared be recalled and destroyed. Subsequently, Poincaré revised his proof and again won the prize; however, this time his work contained the opposite conclusion: the stability of the solar system could not be guaranteed. Poincaré later indicated that minute differences in the initial condition of a system could lead to wildly different outcomes. Small and inevitable errors in knowing the state of a dynamical system necessarily forbid accurate, long-term predictions of the system's evolution; this is the corner stone of chaotic systems. In other words even though it's possible to describe a chaotic system by a set of deterministic equations, its dynamics are inherently unpredictable, and appear to be random.

Several decades after Poincaré's proof, long term predictions in mechanics remained a seldom investigated research topic in Physics. No further progress was made on the problem until the 1950's and 1960's when the stability problem was independently revisited by A.N. Kolmogorov, V.I. Arnold, and J. Moser. Their research led to the important KAM theorem [2–4] stating essentially that series expansions describing the motion of some orbits in many-body systems are convergent provided the natural frequencies associated with these orbits are not close to resonance. With their results, the solar system was found stable in certain configurations and unstable in others. In addition, in the case of small perturbations most of the possible configurations are stable.

The invention of computers with high computational speeds boosted research on chaos because of the ability to simulate an inherent complex system. Simultaneously, with these hardware developments chaos has became increasingly intriguing for scientists of diverse disciplines. The reason for this may be two fold. Firstly, the study of chaos has provided new conceptual and theoretical tools with which we can now understand the behavior of complex systems. Secondly, chaotic behavior is wide spread in nature. It shows up in mechanical oscillators, electrical circuits, lasers, nonlinear optical systems, chemical reactions, nerve cells, heated fluids, and many other systems. Some examples are in the study of cardiac rhythms [5], chemical reactions [6], and disease epidemiology [7].

Before going any further we should first attempt to answer the question, "What is chaos and how should we define it?" Although the term chaos was introduced [8] to refer to "deterministic randomness" in dynamical systems, it is difficult to give a definition that is universally accepted. Regardless of how it is defined, all chaotic systems share a few important characteristics.

1. A dynamical instability leading to unpredictability is a central characteristic of chaos. This instability is exponential rather than linear in time, since if linear, predictability is possible even if there is a slight uncertainty provided a sufficiently long history of the system is known. On the other hand, in the exponential (chaotic)

case, knowing the system's history beyond the initial conditions does not add to the predictions of the system [9].

2. Chaos cannot be explained by external noise [9] since the instability is purely deterministic and intrinsic to the dynamics.

3. Chaotic behavior occurs for a range of conditions in phase space and is in this sense global. Also, the chaotic trajectories should be ergodic, so that they eventually wander throughout the possible range of chaotic trajectories. Noting that, it is also possible to find disconnected regions of chaos in weakly perturbed Hamiltonian systems and in dissipative systems.

4. The system should be in some sense bounded, to avoid trivial exponential separation of trajectories, as in $x(t) = x_0 exp(t)$ for different x_0. To keep the trajectories confined as they separate from each other, there must be some notion of "stretching and folding," as exemplified in the Smale horseshoe map [10]. Another related property is that each point on a chaotic trajectory should lie arbitrarily close to a periodic trajectory (i.e., a trajectory that repeats itself in finite time) [11].

5. The physical model of the system should be simple. It is surprising that simple systems such as the three-body problem can give rise to such complicated and unpredictable behavior, but complicated behavior is not surprising in a system with many degrees of freedom. So, for example, although Brownian motion is unpredictable, a deterministic physical model would include the collisional interactions of a macroscopic number of gas molecules; hence, we would not call this system chaotic. (Note that there are methods for analyzing data to distinguish low-dimensional chaos from such high-dimensional noise [12,13].)

1.1 Chaos in Quantum Mechanics

There is much debate over what is meant by quantum chaos. The differences between quantum mechanics and classical mechanics raise questions about whether chaotic behavior exists in quantum mechanics; how can it be defined and measured?

One can approach the problem of quantum chaos by asking what kinds of chaotic behaviors can be found in quantum systems. Part of the difficulty in carrying over classical chaos to quantum mechanics is that classical chaos is often defined in terms of the divergence of nearby trajectories, which does not have a straightforward quantum analog. However, to put it naively, the Heisenberg uncertainty principle makes it impossible to consider infinitesimal differences between initial conditions in the usual sense that we mean in classical mechanics. To illustrate this point, consider two states $|\alpha\rangle$ and $|\beta\rangle$ whose overlap at time $t = 0$ is $|\langle\alpha(0)|\beta(0)\rangle|^2 = 1 - \epsilon$, where ϵ is very small. If the time evolution is governed by a unitary operator,

$$\hat{U}(t)|\alpha(0)\rangle = |\alpha(t)\rangle \tag{1.1}$$

$$\hat{U}(t)|\beta(0)\rangle = |\beta(t)\rangle \tag{1.2}$$

The overlap at time t is

$$|\langle\alpha(t)|\beta(t)\rangle| = \langle\alpha(0)|\hat{U}^\dagger(t)\hat{U}(t)|\beta(0)\rangle \tag{1.3}$$

$$= \langle\alpha(0)|\hat{I}|\beta(0)\rangle \tag{1.4}$$

$$= \langle\alpha(0)|\beta(0)\rangle \tag{1.5}$$

Thus, if two nearly identical wave packets evolve, even in a nonintegrable system, the wave packets will remain close in the sense that their overlap integral is preserved under unitary time evolution. In other words, there is no exponential sensitivity to initial conditions in state space. However, if one uses this argument against chaos one could also apply it to the overlap integral of two classical phase space distributions evolving by the Liouville equation [10]. What if instead of proposing small perturbations to the quantum state we talked about sensitivity to parameter perturbations? In this case, taking two initially identical wave packets and allowing them to evolve under slightly different Hamiltonians will cause their overlap to drop exponentially under chaotic conditions, but remain large in the stable case, [14–16] since the quantum states associated with chaotic regions in phase space are sensitive to parameter perturbations. Schack et.al [17,18] extended this idea to study the sensitivity of wave-packet evolution under randomly perturbed Hamiltonians showing marked differences between stable and chaotic conditions. There is also the notion of finite time quantum chaos. For instance, in the initial diffusive phase of the quantum kicked rotor [19], focusing on the short-time dynamics, the behavior resembles that of classical chaos. Another case would be initially localized wave packets that show exponential instability for short times [20–22]. Further work in this area has been carried out by Chirikov [23]. Coupling a quantum system to a classical one can give rise to chaotic behavior. Some examples are the case of two-level atoms in a cavity coupled to a classical field [24], or more generally a quantum-mechanical oscillator coupled to a classical oscillator [25]. It has also been proposed that if a classical chaotic system is quantized, that is a quantum mechanical system is created from a classical one, chaos is possible. Blümel has proposed [26] three broad categories for quantum chaotic systems;

1) A purely quantum system which shows exponential sensitivity to initial conditions.

2) A semiclassical system in which both quantum and classical variables can behave chaotically due to the quantum coupling to at least one classical degree of freedom.

3) A quantum system for which the classical analog is chaotic. The last case is the most common one and will be considered in this thesis the in form of the quantum kicked accelerator.

To get a clearer idea of what chaos is and how it works let us point out some important characteristics of classically chaotic systems [10,27]. We will start off with the pendulum Hamiltonian, in order to demonstrate some basic principles of the phase space, often the main tool in studying chaos. Then we will give a brief overview of the delta-kicked rotor, a much studied classical chaotic system and subsequently look into what the delta-kicked rotor would show us if studied under quantum mechanical conditions.

1.2 The Pendulum Phase Space

Any N-degree of freedom Hamiltonian system which has N constants of motion is completely integrable. In other words, those dynamical systems which have as many constants of the motion as degrees of freedom are integrable. Therefore, any 1-degree of freedom, autonomous system (like the pendulum, for example) has the Hamiltonian as a constant of the motion, and is therefore integrable. A useful tool in studying a system's different types of motion is a phase space plot. Such a plot consists of the canonical coordinates $p(t)$ vs. $q(t)$ for all t and for a given set of initial conditions. Fig. 1.1 shows a phase space plot for a pendulum depicting all the possible types of motion of the system. The importance of understanding this plot is due to the fact that the pendulum plays a central role in the analysis of near-integrable systems [28]. The phase space plot shows three different energy/momentum regimes each corresponding to a type of motion represented by a trajectory in the phase space. The first type shows the effect of the potential on the free motion of the pendulum, and the last two are related to the hyperbolic and elliptical fixed points of the system. The trajectory labeled A in Fig. 1.1 is the first type; it occurs at large momentum values where the total energy is larger than the maximum potential energy and shows unbounded rotation. As can be seen in the plot, with the growth of the kinetic energy, the effect of the potential is that it just perturbs the free motion of the pendulum, shown by the flattening of the trajectories. The normal resting point of the pendulum, an elliptical or stable fixed point at the center (labeled B in Fig. 1.1), shows the second type of motion. Small amplitude swinging or vibration of the pendulum gives rise to the closed contours surrounding this point. This collection of closed curves is called an island for that fixed point. On each curve, p and q oscillate with exactly the same frequency. As we get closer to the fixed point at the center, this frequency approaches that of a harmonic oscillator, $\omega = K^{1/2}$. Moving toward the edge, ω approaches zero. The boundry of the island is the last type of motion noted by C. This is the trajectory which connects the hyperbolic or unstable fixed points

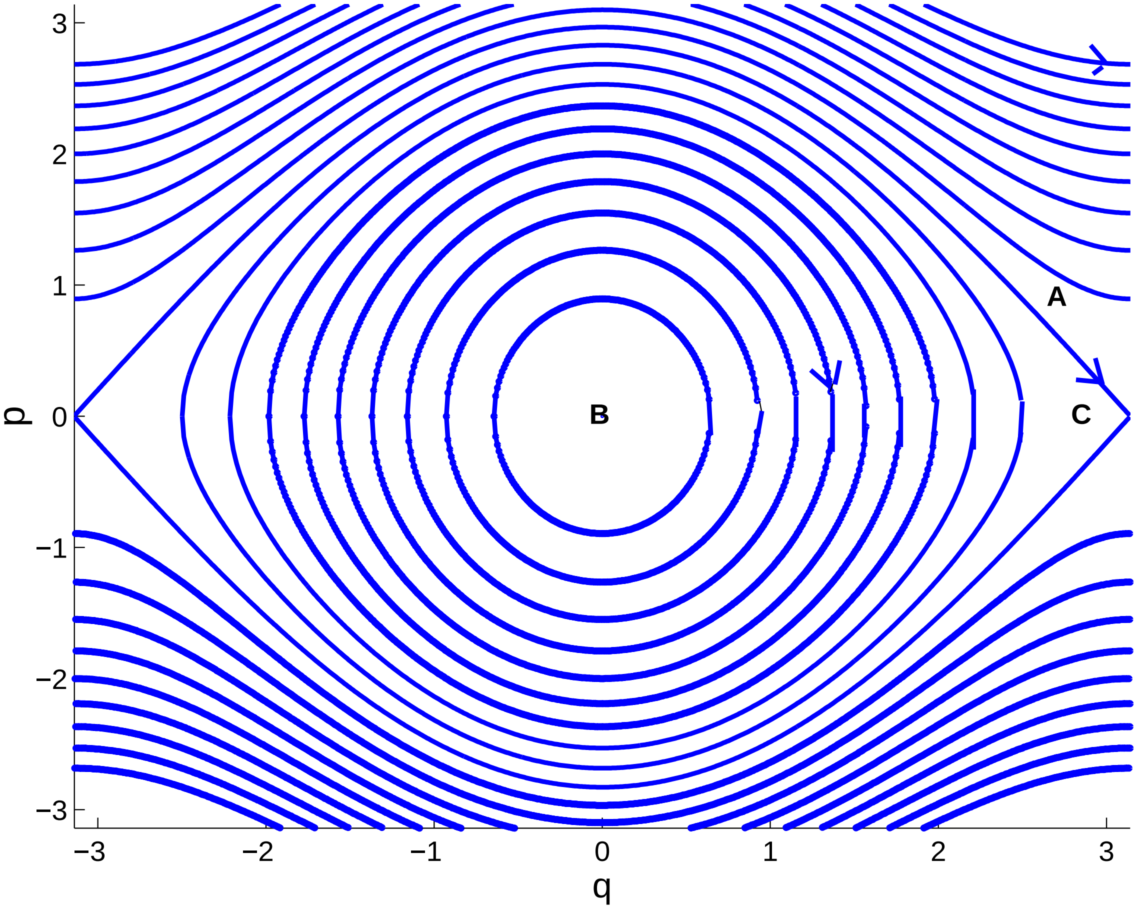

Figure 1.1. Example of a classical pendulum phase space. The trajectories near A show unbounded rotation in q. Trajectories near B show the stable oscillations that make up the island around the central stable fixed point. The points at C are the unstable fixed points which are the limit points for separatrix trajectories.

on either side of the stable fixed point, we call this trajectory the *separatrix*. This trajectory divides the two previous regions and the unstable nature of its endpoints provides the necessary conditions for the growth of stochastic behavior even under slight perturbations. Two other aspects of this figure are worthy of note. Firstly, the arrows on each trajectory represent the direction of the flow and the trajectories do not intersect each other due to the deterministic nature of the motion. Secondly, the trajectories of any set of points within a closed curve, will remain inside the trajectory of the closed curve and the area spanned by these points will remain constant as they flow in the phase space.

It should be noted here that another plot frequently used when studying chaos is Poincaré's surface of section plot. This is a very useful tool getting an idea of a system's integrability. On such a plot the points of intersection of a trajectory with a plane through phase space are plotted. If the phase space only consists of closed curves or periodic points it implies integrability where as a phase space including seemingly randomly scattered points indicates global chaos. A plot showing a mixture of the two above cases indicates a non-integrable system with regions of both chaotic and regular (quasiperiodic) dynamics. For a one-dimensional time dependent system, this takes the form of a strobe plot, a plot where the coordinate and canonically conjugate momentum are plotted against each other periodically in time.

1.3 The Delta-Kicked Rotor

To study the properties of the transition to chaos, the models most used are nonlinear one dimensional systems that are driven by an external field. The importance of these systems is due to the fact that the location and size of resonances can be controlled by changing the frequency and amplitude of the external field. One model that has played an important role in understanding some aspects of the transition to chaos in classical or quantum systems is the delta-kicked rotor (DKR) [27,29]. The DKR is an attractive system to study for several reasons, the most important being that it is simple enough to be reproduced both experimentally and numerically. Mathematically it can be described by a discrete map called the *standard map* where properties can be used to study general characteristics of chaotic behavior near a perturbed resonance. We will start by studying the classical case and subsequently investigate what physical attributes it will have in the quantum regime.

1.3.1 The Classical Delta-Kicked Rotor

Figure 1.2 shows a pendulum, a freely rotating rigid mass where the constant force of gravity provides torque. In the DKR the difference is that this gravitational force is turned on at discrete times independent of the position of the rotor. Thus a force is applied which depends on where the rotor is when the kick begins. If the rotor moves little between pulses, its position will be very predictable and will look like the pendulum, in the limit of continuous small pulses. However, if a single kick is large enough to change the momentum enough to make the position change significantly before the next kick, then the angular dependence allows the subsequent kick to be completely different in size. That is, series of such kicks will have the appearance of a random walk in phase space. This explains why the degree of chaos depends both on the well depth and the period since both conspire to increase the displacement between kicks. The dynamics for such a system are generated by the following Hamiltonian.

$$H = \frac{J^2}{2I} + K\cos(\varphi)\sum_n \delta(t - nT), \tag{1.6}$$

where J is the angular momentum of the rotor, φ is its angular position, and I is its moment of inertia. The parameter, K, is just the strength of the kicks, also called the stochasticity parameter and is proportional to V_0T (in the MKS system), where V_0 is the well depth of the potential and T is the period of kicking. We can now write the resulting Hamilton's equations of motion

$$\frac{dJ}{dt} = -\frac{\partial H}{\partial \varphi} = K\sin(\varphi)\sum_n \delta(t - nT) \tag{1.7}$$

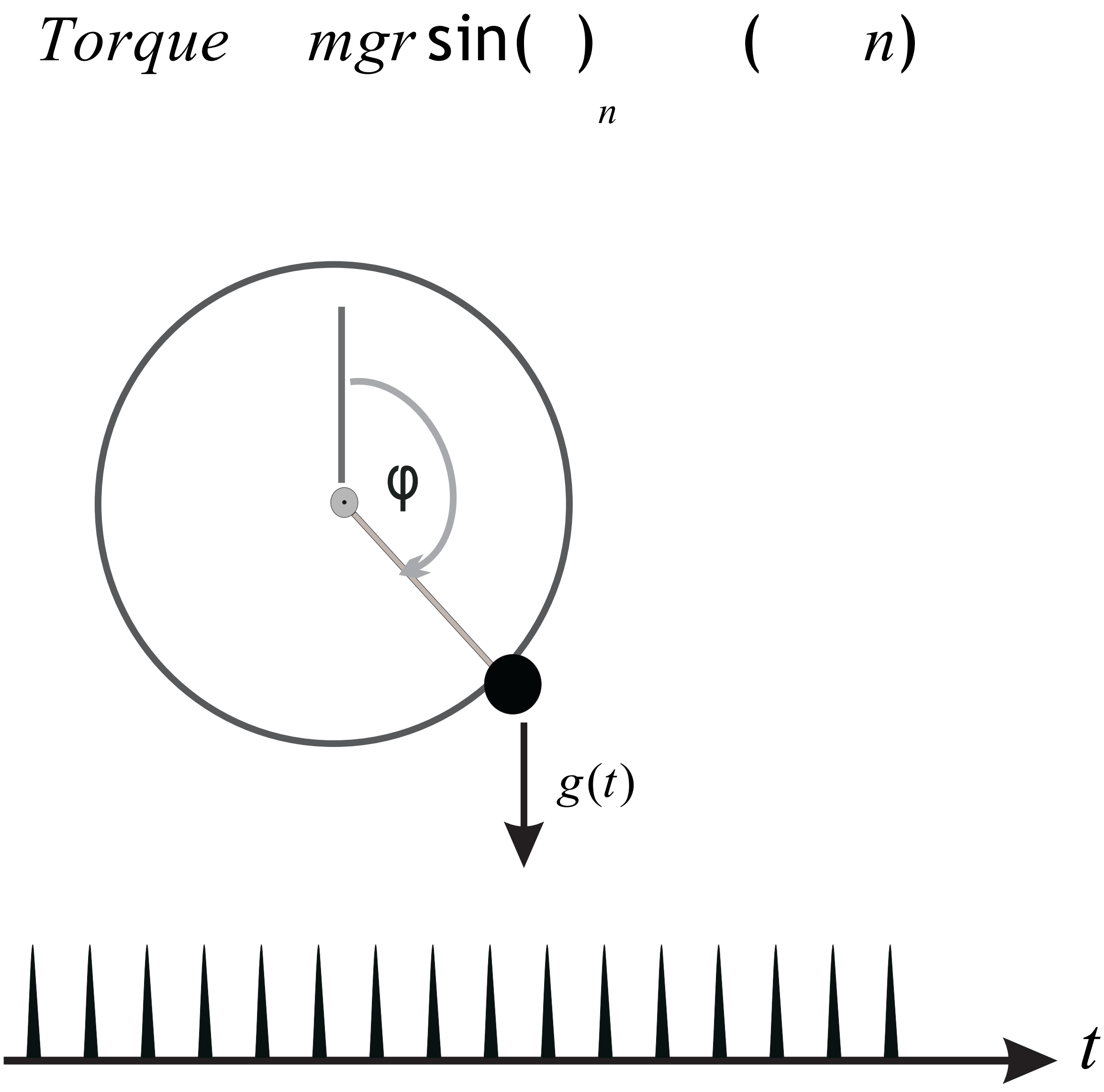

Figure 1.2. The physical picture of a rotor can provide intuition on many of the characteristics of the delta kicked rotor.

$$\frac{d\varphi}{dt} = \frac{\partial H}{\partial J} = \frac{J}{I} \tag{1.8}$$

The rotor is given a delta function kick at times $t = nT$. However, between the kicks no force acts so the rotor evolves freely. Therefore, between the kicks J is constant, and φ evolves linearly. At the kick, J changes discontinuously so that the rate of growth of φ between different kicks will differ. Let us now integrate Eqs. 1.7 and 1.8 from a time just before the kick at $t = nT$ to a time just before the kick at $t = (n+1)T$. The only contribution form the force comes at $t = nT$. Thus,

$$\begin{aligned} J_{n+1} - J_n &= \int_{nt^-}^{((n+1)T)^-} dt \frac{dJ}{dt} \qquad (1.9) \\ &= \int_{nt^-}^{((n+1)T)^-} dt K \sin(\varphi)\delta(t - nT) = K \sin(\varphi_n) \\ \varphi_{n+1} - \varphi_n &= \int_{nt^-}^{((n+1)T)^-} dt \frac{d\varphi}{dt} = \int_{nt^-}^{((n+1)T)^-} dt \frac{J_{n+1}}{I} = \frac{J_{n+1}T}{I} \qquad (1.10) \end{aligned}$$

If we set $I = 1$ and $T = 1$, we obtain

$$\begin{aligned} J_{n+1} &= J_n + K \sin(\varphi_n) \qquad (1.11) \\ \varphi_{n+1} &= \varphi_n + J_{n+1} \qquad (1.12) \end{aligned}$$

This is the *standard map* which was used to generate Fig. 1.3, and other surfaces of section for the DKR in Chapter 4. Notice that the single parameter K completely determines the behavior of this system, and thus its phase space, as shown in Fig. 1.3. For $K = 0$ we see lines of constant momentum (KAM-tori) corresponding to the free rotor. Then, as we increase K, we see the KAM-tori distort and break apart as resonances form. By $K = 2$ we see large regions of chaos with isolated islands. At $K \approx 4$ the primary island becomes unstable, making the phase space for $K > 4$ predominantly chaotic. Our experiments work around $K = 2$, where the island size is big enough that the linear momentum gain (changing with kick number) for atoms with initial conditions overlapping with the stability islands is observable.

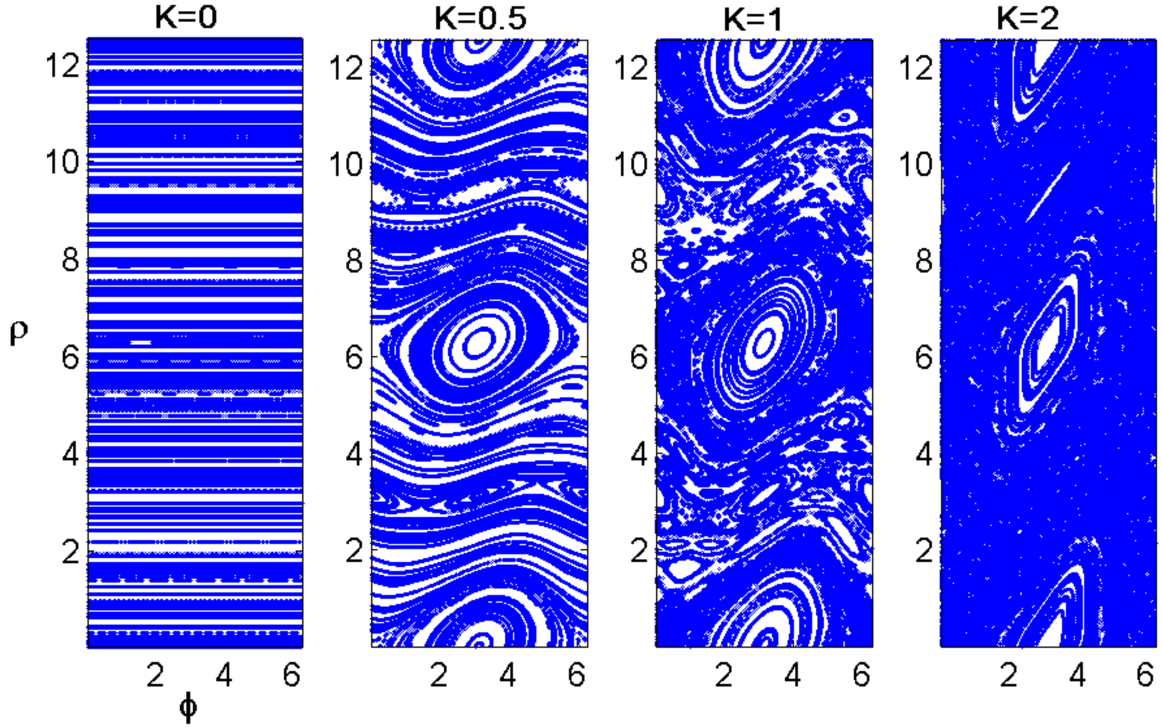

Figure 1.3. Evolution of DKR phase space as a function of the stochasticity parameter, K. $K \approx 1$ marks the onset of global chaos which is seen at $K = 2$ by the diffused "sea of chaos" surrounding the stable islands, allowing unbounded transport through the phase space. Note that each tile is 2π wide in ϕ, and 4π high in ρ.

1.3.2 The Quantum Delta-Kicked Rotor

The *quantum* delta-kicked rotor (QDKR) has played an important role in the field of quantum chaos. It has been studied in some detail by various authors [30–32] and a wide range of effects have been predicted [27]. To arrive at the quantum model of the DKR we start by quantizing Eq. 1.6. This system is easily achieved with an angular momentum operator given by, $\hat{J} = \imath\hbar\frac{\partial}{\partial\varphi}$. Thus the Schrödinger equation is,

$$\imath\hbar\frac{\partial\psi(\varphi,t)}{\partial t} = -\frac{\hbar^2}{2I}\frac{\partial^2\psi(\varphi,t)}{\partial\varphi^2} + K\cos(\varphi)\sum_n \delta(t-nT)\psi(\varphi,t), \tag{1.13}$$

where $\psi(\varphi,t)$ is the probability amplitude to find the rotor at angle φ, and at time t. Let us now write the state of the system at time $t=0$, just after the first kick as a superposition of plane waves of momentum n,

$$\psi(\varphi,0) = \sum_n \psi_n(0)e^{\imath n\varphi}. \tag{1.14}$$

Then between successive kicks, which we choose as $0 < t < T$, where T is the time right before the kick at time $t = T$, the system evolves freely and the state of the system is described as

$$\psi(\varphi,t) = \sum_n \psi_n(0)e^{\imath n\varphi}e^{-\frac{\imath\hbar n^2 t}{2I}}, \quad (0 < t < T). \tag{1.15}$$

What we want now is the state of the system just after the kick at time $t = T$. If we integrate Eq. 1.6 across the kick,

$$\imath\hbar\int_{T-\epsilon}^{T+\epsilon} dt\frac{\partial\psi}{\partial t} + \frac{\hbar^2}{2I}\int_{T-\epsilon}^{T+\epsilon} dt\frac{\partial^2\psi}{\partial\varphi^2} - K\int_{T-\epsilon}^{T+\epsilon} dt\cos(\varphi)\sum_n \delta(t-nT)\psi = 0 \tag{1.16}$$

Then as $\epsilon \to 0$ the contribution of the middle term is zero and the change in the state of the system is determined by the equation

$$\imath\hbar\frac{\partial\psi}{\partial t} = K\cos(\varphi)\sum_n \delta(t-nT)\psi \quad at \quad t = T(T^- < t < T^+), \tag{1.17}$$

where the solution is

$$\psi(\varphi,T^+) = e^{-\imath\frac{K}{\hbar}\cos(\varphi)}\psi(\varphi,T^-). \tag{1.18}$$

Now if we combine Eqs. 1.15 and 1.18, we obtain

$$\psi(\varphi, T^{+}) = e^{-\imath \frac{K}{\hbar} \cos(\varphi)} \sum_{n} \psi_n(0) e^{\imath n \varphi} e^{-\frac{\imath \hbar n^2 t}{2I}} \tag{1.19}$$

Eq. 1.19 relates the state of the rotor at time $t = T$ to its state at $t = 0$.

1.4 Experiments in Quantum Chaos

Progress in the field of quantum chaos has been heavily theoretical but during the past few decades many experiments have been carried out to complement the theoretical advances. In this section we give a glimpse of the experimental work in quantum chaos, demonstrating its importance in a variety of systems. Experiments done by Bayfield and Koch in 1974 on multi-photon ionization of highly excited hydrogen atoms provided the basis for work which later lead to evidence of dynamical localization. Specifically, under certain experimental conditions the classical theory no longer agreed with the data while the analytical theory of localization was in agreement with the experimental results [33–35]. Rydberg atom ionization experiments have given rise to a variety of interesting phenomena [36], such as scarring effects [35,37] and effects due to "metamorphoses" of classical resonances as the field strength is varied [38]. Spectroscopy of atoms in external fields also provided a frequency-domain arena for tests of quantum chaos, including level statistics [39,40] and the influence of periodic orbits [41–43]. The statistics of resonances in atoms, molecules, and nuclei have also been shown to exhibit level-repulsion effects [14]. As mentioned before, mesoscopic semiconductor structures provide an important arena for the study of quantum chaos [44]. Conductance measurements of semiconductor billiard structures show "universal conductance fluctuations" and weak localization effects with the application of strong magnetic fields [44,45]. The tunneling current through quantum-well heterostructures ("resonant tunneling diodes") can also be understood in terms of unstable periodic orbits in a chaotic regime [46] and show effects due to scarring [47]. Semiconductor antidot lattices provide a different setting for studying conductance fluctuations with applied magnetic fields [48,49], giving an experimental realization of the Lorentz gas [44]. Another related billiard-like system is the "quantum corral" [50], where a scanning tunneling microscope (STM) can be used to move individual atoms on a surface to build a confining structure for electrons. A different class of experiments explores the area of "wave chaos," exploiting the formal equivalence of various other wave equations to the Schrödinger equation under certain circumstances. Perhaps the most notable among these are the microwave-cavity billiard experiments [44], in which such topics as level statistics [51], scarring [52], dynamical localization [53], chaos-assisted tunneling [54], and a trace formula [55] have been studied. This line of analysis has been extended to the study of deformed micro-disk cavity lasers, which act as open billiard systems in the optical domain [56]. A similar realization of wave chaos occurs with the mechanical vibrations of aluminum blocks [57] or rigid plates [44,58], and billiard type experiments can be carried out using surface waves [59,60] or ultrasonic waves [61] in fluids. Many of these billiard-type experiments are reviewed in [44]. Finally, the equivalence of the electromagnetic equation in the paraxial approximation with the Schrödinger equation can be exploited to create an optical realization of the kicked rotor [62,63]. Atomic physics has also been an active front in quantum chaos research. In the following we will give a more detailed review of our groups contribution in this area.

1.5 Quantum Chaos in atomic physics

Theoretical work on this subject had largely concentrated on the investigation of idealized systems such as the quantum delta-kicked rotor (QDKR) which was already well known from extensive work in the classical regime [28]. The experimental study of this system gained new impetus through its realization using laser cooled atoms exposed to a corrugated potential from a pulsed off-resonant standing light wave [64]. This system has subsequently led to many discoveries in the field of quantum chaos including observation of quantum resonances [64,65], dynamical localization [66,67] and quantum diffusion [68,69].

The delta kicked accelerator is another example which has been widely used in studying aspects of the transition to chaos in classical and quantum systems [27]. Again advanced cooling and trapping techniques has brought the study of the quantum delta kicked accelerator (QDKA) to the experimental frontiers. Experimentally, the QDKA was first realized in the Oxford group in 1999 by exposing a sample of laser cooled atoms to a pulsed off-resonant standing wave of light in the direction of gravity [70]. The most striking feature of this experiment was the observation of quantum accelerator modes (QAMs) which are characterized by their linear momentum gain with pulse number. Quantum accelerator modes appeared close to quantum resonance times which are integer multiples of the half-Talbot time [70]. At the Talbot time, plane waves with certain initial momenta in the kicking direction acquire a phase factor of 2π. QAMs have applications in the fields of quantum chaos [71,72], atomic physics [73,74] and nonlinear dynamics [75].

In order to understand the observed behavior of the quantum accelerator modes, Godun *et. al* [73] developed a model based on the interference (referred to as interference model hereafter) between different momentum states populated by diffraction of the matter waves from the diffraction gradient created by the pulsing standing wave light.

Soon after, Fishman, Guarneri, and Rebuzzini (FGR) [76] developed a pseudo-classical method to study the QDKA (ϵ-classical model hereafter). They showed that for time intervals between kicks close to a resonance, a classical treatment of the QDKA is possible. Using this approach they attributed the QAMs to the stability islands that appear in the underlying pseudo-classical phase space of the QDKA.

In the experiments conducted at Oxford, the cold atomic samples had a momentum distribution significantly wider than two recoil momentum and therefore one could not observe the discreteness of the atomic wavefunction after applying standing waves. This experimental limitation prevented further investigation of the creation mechanism of the QAMs. Furthermore, this technical limitation has also made it difficult to quantitatively validate either of the theoretical models and their predictions. However, the fact that the interference model failed to predict higher order QAMs has played in favor of the ϵ-classical theory such that it has been adopted by the subsequent research efforts related to QAMs.

A straightforward way to over come this limitation would be to use a sample of atoms with much lower temperatures than the laser cooled atoms utilized in the Oxford group. A Bose-Einstein condensate (BEC) seemed to be an excellent candidate for such experiments with the additional advantage of being a pure quantum mechanical system with macroscopic size. To this end a BEC was realized at OSU in 2004 using and optical trap [77]

1.6 A Brief History of the Realization of the Bose-Einstein Condensate

At the time when our lab was established there were two approaches towards realizing a BEC. The first method was very well known, using magnetic traps and rf evaporative cooling. This method was developed by Eric Cornell, Carl Wieman and co-workers at JILA in a remarkable series of experiments leading to the first production of BEC in a dilute gas of Rubidium atoms using a TOP trap in 1995 [78]. Shortly thereafter Wolfgang Ketterle and co-workers at MIT created a BEC of sodium atoms also in a magnetic trap [79]. An interesting review of the historical development of laser cooling and the achievement of BEC can be found in review articles by Phillips [80] and Cornell *et al.*,[81]. In short, the steps leading to the realization of BEC within these groups consisted of pre-cooling the atomic vapor using laser cooling techniques to sub-mK temeratures , transferring these atoms to a magnetic trap and subsequently cooling to the BEC transition with evaporative cooling induced by energy an selective spin transition. While their method was ingenious, it was also slow, requiring evaporative times on the order of minutes. The system needed to be very well isolated from stray rf and optical fields. Having an alternative rapid technique for producing BEC thus became a desirable goal.

In a different approach, all-optical methods of reaching the BEC phase transition have been pursued since the early days of laser cooling. Despite many impressive developments beyond the limits set by Doppler cooling, including polarization gradient cooling [82], velocity selective coherent population trapping [83], Raman cooling [84–86], and evaporative cooling in optical dipole traps [87–91], the best results, as far as the phase space density was concerned, was a factor of 10 away from the BEC transition [90,91]. Hence, optical traps played only an auxiliary role in BEC experiments. For example, a group at MIT used a magnetic trap with an optical dipole to reversibly condense a magnetically confined cloud of atoms restoratively cooled to just above the BEC transition [92]. Additionally, Bose condensates created in magnetic traps had been successfully transferred to shallow optical traps for further investigations [93–96]. Finally, it was Michael Chapman's group at Georgia Institute of Technology that announced the first creation of a BEC using an all-optical method in 2001 [97]. Soon after, the Grimm group at Innsbruck condensed Cesium atoms using an all-optical technique [98]. In spite of the successful demonstration of the all-optical approach, there was little known about how the method worked. In a surprising coincidence, our group and the Weiss group at Pennsylvania state university independently realized that an important factor in efficient loading of an optical trap was its volume. These efforts led to the invention of time averaged optical traps [77] by our group and the compressible crossed dipole trap technique [99] for creating BEC by the Weiss group. These techniques have streamlined achieving BEC using the all-optical approach and have become a robust method for the creation of condensates.

1.7 Organization

The following chapters describe the work I carried out in the BEC laboratory at Oklahoma State University. The broad aim was to study quantum accelerator modes utilizing a BEC of Rb87 atoms, in which only optical methods were used. However before this research could be carried out it was necessary to develop a new set of techniques for creating the condensate. This involved upgrade the existing setup which used a crossed beam optical trap to one that used a single beam. This would make the experiment much more robust and allow for the production of larger condensates. In accordance with these goals this dissertation has been organized as follows.

In Chapter 2 a review of the Physics of laser cooling and trapping of neutral atoms is presented. The steps required to make a BEC starting from preparing magneto-optical traps as a source of cold atoms, loading them into a wide optical trap, and compressing these traps into tighter ones for efficient evaporative cooling will be explained.

The experimental setup will be briefly reviewed in chapter 3. The theoretical models for QAM's will be studied in Chapter 4. There are essentially two prevailing models for QAM studies and in this chapter we will see the fundamental equivalency of the two. Further development of the interference model will be also pursued in order to explain the higher order QAMs. Generalization of those concepts allow the prediction of the existence of QAM's at higher order quantum resonances. Our results are in very good agrement with our observations.

Chapter 5 is dedicated to a detailed experimental study of QAMs in the context of the $\epsilon-$classical model. This chapter demonstrates how using a BEC enables one to examine this model with an exquisite precision. And in the end, in Chapter 6 we highlight the possible new directions for this field of research.

CHAPTER 2

TECHNIQUES TO COOL AND TRAP NEUTRAL ATOMS FOR BOSE-EINSTEIN CONDENSATE

As mentioned in the introduction, BEC is our golden tool for the research presented in this dissertation. The technical approach for creating BEC is a fascinating endeavor, one where the final experimental set up is truly a fine built machine. To honestly appreciate this structure a thesis needs to be solely dedicated to how one can make a BEC. Fortunately for me, this task has already been carried out by Peyman Ahmadi [100], in his thesis, where he gives a highly detailed account of the experimental and setup. Therefore, here I will only briefly mention the physical conditions required for creating a BEC and will continue with a review of the theoretical foundations for different laser cooling techniques of neutral atoms.

The history of BEC began when attempts were made to calculate the black body spectrum. Satyendranath Bose, in 1924, formulated the distribution of identical particles (such as Plancks radiation quanta) in a way that allowed him to calculate the Planck spectrum using the method of statistical mechanics [101]. Einstein generalized Bose's new idea to include identical particles with discrete energies. The result was Bose-Einstein (BE) statistical mechanics. The BE distribution is written as

$$N(E) = 1/(\exp(\beta(E-\mu)) - 1), \tag{2.1}$$

where $\beta = 1/k_BT$, E is the energy of the particle and μ the chemical potential. Einstein applied the new concept of Bose statistics to an ideal sample of atoms or molecules that were at thermal equilibrium and trapped in a box. Based on this model he predicted that at sufficiently low temperatures the particles would accumulate in the lowest quantum state in the box, giving rise to a new state of matter with many unusual properties [102,103]. Conceptually, the effects of quantum statistics (which stems from the indistinguishability of the particles) arises if the mean inter-particle distance; $(V/N)^{1/3}$, where V is the volume of the system, is comparable to the mean thermal wavelength of the particles λ_{dB},

$$(\frac{V}{N})^{1/3} \approx \lambda_{dB},$$

or $n\lambda_{dB}^3 \approx 1$, which is refereed to as the "phase space density" - the number of atoms within a volume λ_{dB}^3. The process of increasing the phase space to the order of unity is what we know today as Bose-Einstein condensation.

The experimental realization of BEC has had a long history of its own dating to the first efforts of cooling atoms. The field picked up momentum with the advances in laser cooling. The understanding of how light exerts force on material objects goes back to the 18th century with Maxwell's calculation of the momentum flux density of light. In the early 19th century Lebedev [104] and Nichols and Hull [105] conducted the first laboratory experiments where they observed the light pressure on macroscopic objects which quantified the theories. Later in 1917 this phenomena was explained quantum mechanically by Einstein with momentum transfers through absorption and re-emission of photons by atoms. Frisch [106] in 1933 showed how an atomic sodium beam could be deflected with resonance radiation from a lamp, where the average change in momentum was due to scattering of one photon. With the invention of the laser, Ashkin [107] recognized the possibility of manipulation of atoms with this intense, narrow-band light. Ashkin called the radiative force the atoms experience the "scattering force" because it results when light strikes an object and a photon scatters with no preferred direction, comet tails being an example of such forces in nature. Another radiative force is the dipole force, which can be thought of as arising from the interaction between an induced dipole moment and the gradient of the incident light field. This force was fist introduced by Askar'yan [108] in 1962 in connection with both plasmas and neutral atoms. In 1968 this led to a proposal by Letokhov [109] that atoms might be confined along one dimension in a standing wave of light tuned far from an atomic transition. Two years later Ashkin trapped micron-sized particles with a pair of opposing, focused beams of laser light.

The idea of laser cooling which is basically the reduction of random thermal velocities using radiative forces was proposed in two independent papers by Hänsch and Schawlow [110] and Wineland and Dehmelt [111]. Three years later in 1978 Ashkin [112] described how an atomic beam of sodium could be slowed down using the radiation pressure of a laser beam tuned to an atomic resonance. Furthermore, after being slowed, they could be trapped in the focus of laser beams which would damp their motion until their temperature reached the micro-kelvin range.

These were the foundations that paved the way for Steve Chu, Claude Cohen Tannoudji and William D. Phillips to develop methods to cool and trap atoms with laser light for which they were awarded the Nobel prize in 1997. Their achievements led the way to the realization of a BEC (Bose-Einstein condensate) in 1995 by Eric.A. Cornell, Wolfgang Ketterle, and Carl E. Wieman. This achievement garnered the 2001 Nobel prize in physics.

Before discussing the details of how laser cooling works, the term “temperature” should be properly defined. When the word temperature is used in Physics the thermodynamic definition usually comes to mind. Here temperature is a parameter of state of a closed system in thermal equilibrium with its surroundings, which is in thermal contact with the environment. In laser cooling the atoms are always absorbing and scattering light and thus making major changes to their environment, additionally there is no heat exchange occurring since light, even though a form of energy, can not be considered heat. So although the system is in a steady-state situation, it is not in thermal equilibrium and hence using the word temperature in the thermodynamic sense is inaccurate.

Temperature is given as a label that describes how the average kinetic energy of an atomic sample with a well defined velocity distribution has been reduced, and is written as

$$N_D K_B \frac{T}{2} =< E_k >= \frac{m v_{rms}^2}{2}, \tag{2.2}$$

Where K_B is the Boltzman constant, N_D the number of dimensions, $< E_k >$ the average kinetic energy, and v_{rms} is the root-mean-squared of the velocity.

2.1 Laser cooling mechanism

The process that enables laser cooling is the exchange of energy and momentum between atoms and the light field. In order to get an intuitive understanding of how light slows atoms down, let us consider an atomic beam with velocity $\overrightarrow{v}$ that is irradiated by an opposing laser beam with frequency $\overrightarrow{\omega} = c\overrightarrow{k}$ (See Figure 2.1.) A ground-state atom that absorbs a photon gains energy $\hbar\omega$ and momentum $\overrightarrow{p}_{absorb} = \hbar\overrightarrow{k}$ due to energy and momentum conservation. The recoil $\overrightarrow{p}_{recoil} = \overrightarrow{p}_{absorb} = \hbar\overrightarrow{k}$ the atom experiences during this interaction is along the direction of the laser beam, which opposes the atoms motion. As a result the atom is slowed by $v_{recoil} = \hbar k/m$. In the excited state the atom no longer absorbs further photons. However, the atom eventually returns back to the ground state by spontaneously emitting a photon with momentum $\overrightarrow{p}_{emitted}$, recoiling in the opposite direction to the photon. The total change of momentum the atom receives in this sequence of events is therefore, $\Delta p = \overrightarrow{p}_{absorb} - \overrightarrow{p}_{emitted}$. Since the emission of photons is random and has no preferred direction, its contribution to the atom's momentum averages to zero for a large number, N, of scattering events. Consequently, the net force an atom experiences (for $N >> 1$) is $\overrightarrow{F}_{scatter} = N\overrightarrow{p}_{absorb}\gamma$, where γ is the scattering rate and $\overrightarrow{F}_{scatter}$ is referred to as the scattering force.

Although the average momentum transfer to an atom due to spontaneous emission is zero, its fluctuation is not. The random photon emission introduces an uncertainty $\hbar k$ in the atoms momentum because the direction of the recoil is unknown.

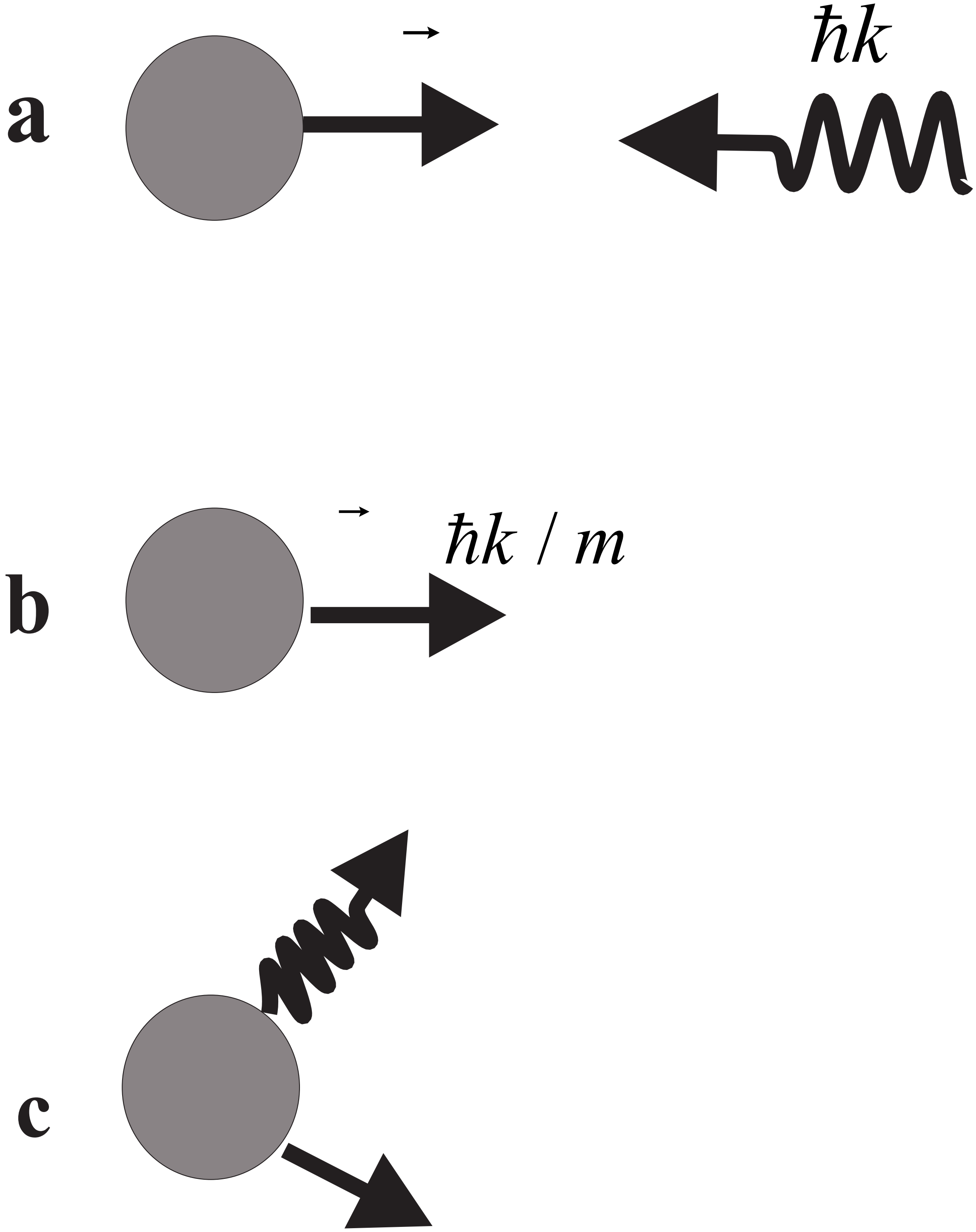

Figure 2.1. (a) An atom with velocity $\vec{v}$ encounters a photon with momentum $\hbar k$. (b) After absorbing the photon, the atom is slowed by $\hbar k/m$. (c) After re-radiation in a random direction , the atom is on average slower than (a).

Therefore using spontaneous emission as the cooling mechanism, the atoms momentum can at best be reduced to $p_{recoil} = \hbar k$, which corresponds to a temperature $T_{recoil} = \hbar^2 k^2/2mK_B$, called the recoil limit. In summary, spontaneous emission is both the dissipative process necessary for laser cooling and the factor which limits the temperature achievable to the recoil temperature.

2.2 Laser Cooling as a Random Walk

Since the energy and momentum exchange during the interaction is characterized by discrete finite momentum "kicks", one can describe the motion of the atom by a random walk through momentum space. A simple model to consider would be an atom moving only in one dimension and the effect of a standing plane wave. Here, the randomness arises from the spontaneous emission of a photon, and the uncertainty of the absorption direction. The steps of this walk are of size $\hbar k$ and are generally much smaller than the momentum of thermal atoms $mv_{rms} = K_B T^{1/2}$, as is easily seen by comparing the two.

$$\frac{\hbar k}{mv_{rms}} = \sqrt{\frac{T_{recoil}}{T}} << 1 \tag{2.3}$$

The recoil temperature $T_{recoil} = \hbar k/2mK_B$ is of the order of a μK for most laser cooled elements, whereas cryogenic temperatures, for instance liquid helium, are of the order of a few K. Thus, the scattering of a single photon has a negligible effect on the overall atomic motion, but many repeated scattering events can result in large changes in the atomic motion. For example, a typical sodium (^{23}Na) beam has a velocity $v = 10^5$ cm/s , whereas the recoil velocity due to the resonance light ($\lambda = 589$nm) used to cool sodium is only about $v_{recoil} = 3$ cm/s . Therefore a sodium atom has to undergo about 10^4 scattering events before coming to rest. Assuming a perfect 2-level atom in the steady state, the atom can remain at most half of the time in the excited state, which has a lifetime of about $t = 16$ns for this sodium transition. Consequently, the atom can scatter a photon about every 32ns bringing the atom to rest in about 1 ms. A two-level atom confined to motion in one a dimensional (1-D) standing wave is the simplest case to model which will be discussed here. At any time t, an atom with momentum p has the probability $\epsilon_+(p)$ to gain $\hbar k$ momentum and a probability $\epsilon_-(p)$ to gain $-\hbar k$. Note that the probabilities will depend on the momentum of the atom. The number of atoms with momentum p at time t is given by the momentum distribution of the atoms $W(p,t)$. After a typical scattering time Δt (Δt being the average time between two scattering events) the distribution will change according to

$$\begin{aligned} \triangle W &= W(p, t+\triangle t) - W(p,t) \qquad (2.4) \\ &= -[\epsilon_+(p)+\epsilon_-(p)]W(p,t) + \epsilon_+(p-\hbar k)W(p-\hbar k,t) + \epsilon_-(p+\hbar k)W(p+\hbar k,t). \end{aligned}$$

The first term on the right hand side is equal to the rate at which the atoms with momentum p receive a momentum kick in the + or − direction. The second (third) term gives the rate at which atoms with momentum $p \pm \hbar k$ jump toward the momentum p by receiving a momentum kick $\pm\hbar k$. As stated before, the momentum kicks are of order, $\hbar k$ and are generally much smaller than the momentum of a thermal atom $p = mv_{rms}$. Therefore the last two terms on the right hand side of Eq. (2.5) can be Taylor expanded as follows:

$$\begin{aligned} \epsilon_\pm(p \mp \hbar k)W(p \mp \hbar k) &= \epsilon_\pm(p)W(p,t) \mp \hbar k \frac{\partial}{\partial p}[\epsilon_\pm(p)W(p,t)] \\ &+ \frac{(hk)^2}{2}\frac{\partial^2}{\partial p^2}[\epsilon_\pm(p)W(p,t)] + O(\frac{\hbar k}{mv_{rms}})^3 \qquad (2.5) \end{aligned}$$

Inserting this expansion into Eq. (2.5) and neglecting terms of order of the last term in Eq. (2.5) (The validity of the approximation is explained above. See Eq. (2.3)), one gets

$$\Delta W = -\hbar k \frac{\partial}{\partial p}([\epsilon_+(p)-\epsilon_-(p)]W(p,t)) + \frac{1}{2}(\hbar k)^2 \frac{\partial^2([\epsilon_+(p)+\epsilon_-(p)]W(p,t))}{\partial p^2} \qquad (2.6)$$

Taking the limit for $\Delta t \to 0$, we get

$$lim_{\Delta t \to 0}\frac{\triangle W}{\triangle t} = \frac{\partial W(p,t)}{\partial p} = -\frac{\partial[M_1 W(p,t)]}{p} + \frac{1}{2}\frac{\partial^2[M_2 W(p,t)]}{\partial p^2} \qquad (2.7)$$

with

$$\begin{aligned} M_1 &= [\epsilon_+(p) - \epsilon_-(p)]\frac{\hbar k}{\triangle t} && (2.8) \\ M_2 &= [\epsilon_+(p) + \epsilon_-(p)]\frac{(\hbar k)^2}{\triangle t} && (2.9) \end{aligned}$$

The above equation, as expected, is of the same form as the Fokker-Planck equation:

$$\frac{\partial W(p,t)}{\partial p} = -\frac{\partial [F(p,t)W(p,t)]}{\partial p} + \frac{\partial^2 [D(p,t)W(p,t)]}{\partial p^2} \tag{2.10}$$

with the drift or damping force, $F(p,t) = M_1$ and the diffusion term, $D(p,t) = \frac{1}{2}M_2$. The stationary state distribution $W(p,t)$ of the process is found by setting

$$\frac{\partial W(p,t)}{\partial p} = 0. \tag{2.11}$$

For the case that both the force and the diffusion term are time-independent, the solution to the stationary state is given by

$$\overline{W}(p,t) = \frac{C}{D(p)} exp(\int_0^{\mu} \frac{F(p')}{D(p')} dp') \tag{2.12}$$

which can easily be solved once the force and diffusion coefficient are known.

2.3 The Rabi Two-Level Problem

Further investigation into the photon-atom interaction will reveal the exact nature of the damping force and diffusion term in a scattering event. The Hamiltonian for an atom interacting with a single frequency light field can be written as,

$$H = H_0 + H'(t), \tag{2.13}$$

where $H_0 = \sum_k \hbar\omega_k |\phi_k(\overrightarrow{r})\rangle\langle\phi_k(\overrightarrow{r})|$ is the field-free time independent atomic Hamiltonian with eigenvalues $\hbar\omega_k$ and eigenstates $|\phi_k(\overrightarrow{r})\rangle$, and $H'(t)$ is the atom-field interaction. To study how the wave function of the atom evolves we start with the time dependent Schrödinger equation for the total Hamiltonian, H, of the atom in a radiation field,

$$H\Psi(\overrightarrow{r},t) = i\hbar\frac{\partial |\Psi(\overrightarrow{r},t)\rangle}{\partial t}. \tag{2.14}$$

It will be apparent later that it is helpful to rewrite the above equation as

$$i\hbar\frac{dc_j(t)}{dt} = \sum_k c_k(t)H'_{jk}(t)e^{i\omega_{jk}t} \tag{2.15}$$

where $H'_{jk}(t) = \langle\phi_j(\overrightarrow{r})|H'(t)|\phi_k(\overrightarrow{r})\rangle$ and $\omega_{jk} = (\omega_j - \omega_k)$. To derive the above equation is simple; expand the wavefunction in terms of the eigenstates of the free atom

$$|\Psi(\overrightarrow{r},t)\rangle = \sum_k |\Psi(\overrightarrow{r},t)\rangle\langle\phi_k(\overrightarrow{r})|\phi_k(\overrightarrow{r})\rangle e^{-i\omega_k t} = \sum_k c_k(t)|\phi_k(\overrightarrow{r})\rangle e^{-i\omega_k t}, \tag{2.16}$$

and subsequently insert this sum into Eq. 2.14 a few further simple mathematical steps gives Eq. 2.15

The above manipulations involve no approximations. However, Eq. 2.15 cannot be solved for the general case of an atom in a radiation field, making approximations necessary. We start by truncating the sum in Eq. (2.15) to just two terms, the single ground; $(k = 1 \rightarrow g)$, and excited state; $(k = 2 \rightarrow e)$, connected by a laser field. This results in two coupled differential equations which can then be solved. This type of calculation was first studied in 1937 by Rabi in the context of magnetic resonances and thus is often referred to as the Rabi two-level problem. A two-level atom is illustrated in Fig. 2.2. The solution starts by absorbing the diagonal elements of $H'(t)$ into H_0. Keeping in mind that $H'_{ge}(t) = H'^{*}_{eg}(t)$, we arrive at the following coupled differential equations,

$$i\hbar\frac{dc_g(t)}{dt} = c_e(t)H'^{*}_{eg}(t)e^{-i\omega_0 t} \tag{2.17}$$

$$i\hbar\frac{dc_e(t)}{dt} = c_g(t)H'_{eg}(t)e^{i\omega_0 t}, \tag{2.18}$$

where $\omega_0 = \omega_{eg}$ is the atomic resonance frequency. It should be noted that the coefficients $c_e(t)$ and $c_g(t)$ can be interpreted as transition amplitudes, their squares $c_{e(g)}(t)^2 = c_{e(g)}(t)c^*_{e(g)}(t)$ giving the transition probabilities. $H'(t)$ describes the Coulomb interaction of the atom's electron at position $\overrightarrow{r}$, with the radiation field. In the case of laser cooling, this can be considered as a classical single mode electromagnetic field with an electric field vector $\overrightarrow{E}(\overrightarrow{r},t)$. To evaluate H' in the most

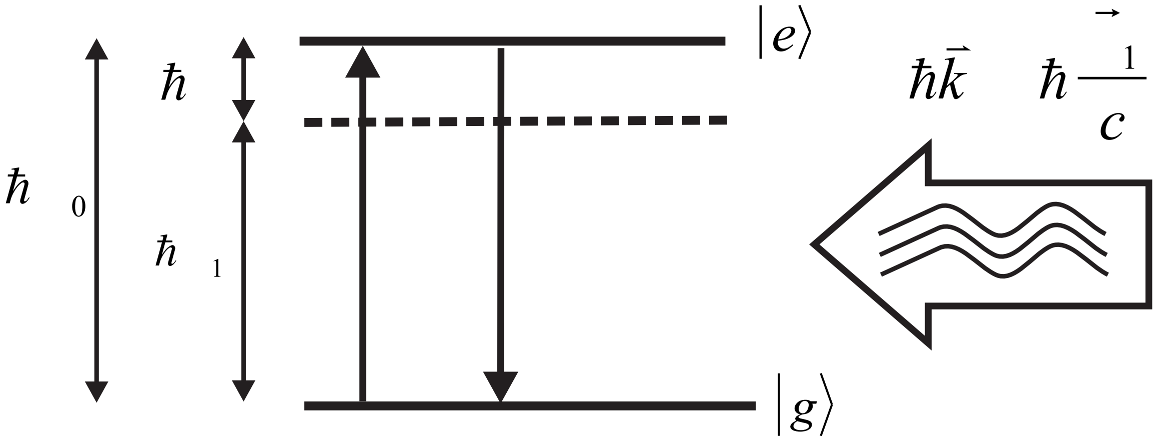

Figure 2.2. A two level atom interacting with a radiation field ω_l. As a result, the atom oscillates between the ground and excited state.

general form, we start by writing it as the sum of the kinetic energy and the Coulomb potential seen by the electron. After some manipulations, we arrive at the expression: $H'(t) = -e\overrightarrow{E}(\overrightarrow{r},t).\overrightarrow{r}$. Two further approximations are required to solve this problem. One is the rotating wave approximation (RWA), which assumes that the laser frequency, ω_l, is much larger than the detuning $\triangle = \omega_l - \omega_0$. This basically means that the incident light is close to resonance, $\omega_l \approx \omega_0$. The next is referred to as the electric dipole approximation, which assumes the electric field of the light $\overrightarrow{E}(\overrightarrow{r},t)$ is constant over the location of the electron. Since $\overrightarrow{E}(\overrightarrow{r},t)$ varies spatially as the wavelength of the incident light, typically several hundreds of nm, and the electron is almost entirely contained within a sphere of a radius typically smaller than 1 nm, this approximation is a good one. For a plane wave traveling in the positive z-direction, the electric field operator is $\overrightarrow{E}(\overrightarrow{r},t) = E_0 cos(kz - \omega_l t)\widehat{\epsilon}$ where E_0 is the amplitude of the light field and $\widehat{\epsilon}$ is the polarization direction. In case of a 2-level atom, the dipole moment; $e\overrightarrow{r}$ is parallel to the polarization field $\widehat{\epsilon}$ and the interaction element becomes $H'_{eg}(t) = \hbar\Omega cos(kz - \omega_l t)$, where Ω is the Rabi frequency defined as; $\Omega = -eE_0/\hbar\langle e|r|g\rangle$. Using these approximations the differential equations 2.17 and 2.18 can now be uncoupled and solved to give the evolution of the ground and excited state populations as,

$$\rho_g = |c_g(t)|^2 = cos^2\frac{\Omega' t}{2} + (\frac{\triangle}{\Omega'})^2 sin^2\frac{\Omega' t}{2} \tag{2.19}$$

$$\rho_e = |c_e(t)|^2 = (\frac{\Omega}{\Omega'})^2 sin^2\frac{\Omega' t}{2}, \tag{2.20}$$

where $\Omega' = \sqrt{\Omega^2 + \triangle^2}$. A brief look at these equations gives a general description of how the atom behaves in the radiation field showing how the atom oscillates between the ground and excited state with a frequency Ω' and a probability amplitude $(\Omega/\Omega')^2$. If the incident light is on resonance $\triangle = \omega_l - \omega_0 = 0$, the probability oscillates at the Rabi frequency Ω and its amplitude is 1.

2.4 The Optical Bloch Equations

In the above discussions the energy of the system, the combined applied radiation field and the atom, is conserved. This means that the equations only describe stimulated absorption and stimulated emission, both coherent processes. In these cases the energy is transferred from the radiation field to the atom (and vice versa) as the atom absorbs a photon from (emits a photon into) the radiation field and makes a transition from the ground to the excited state (from the excited to the ground state). Yet in order to cool the atom, energy must be dissipated. One such energy dissipating process is spontaneous emission, in which the photon is emitted into the vacuum (with random direction and a random polarization) instead of the applied radiation field. The spontaneously emitted photon is not part of the observed system, and therefore information about the emitted photon such as its direction of emission and polarization is lost. Because of this partial detection of the final state, the system is no longer in a pure state, but evolves into a statistical mixture. Formulating this dissipative process requires the use of the density matrix formalism. The time evolution of the density matrix ρ in a closed system, one where the system remains in a pure state, depends on the Hamiltonian according to the Von Neumann equation,

$$i\hbar\frac{d\rho}{dt} = [H, \rho]. \tag{2.21}$$

This formalism is equivalent to the Schrödinger description used earlier and will give the same solutions as before. When the atom undergoes spontaneous emission however, the emitted photon is not observed and it is necessary to take a statistical average over its possible directions and polarizations. This is done by tracing over the possible states of the emitted photon P. The density matrix for atom, A, then becomes $\rho_A = Tr_P(\rho_{AP})$. More precisely, the spontaneous emission of a photon can be regarded as the interaction of the atom with the vacuum state of the quantized electromagnetic field. The radiation field B, in which atom A is immersed, has many more degrees of freedom than the atom and therefore can be considered as a heat reservoir as defined by statistical mechanics. It is safe to assume that the reservoir obeys the Markov approximation; stays close to thermal equilibrium and has a very short relaxation time. We can now write the Hamiltonian of the total system as $H = H_A + H_F + H_{AF}$, where the first term on the left is the Hamiltonian for the free atom; $H_A = \sum_{k=g,a} \hbar\omega_k |k\rangle\langle k|$, the second term is the quantized radiation field; $H_F = \sum_{k=g,a} \hbar\omega_k a^{\dagger}_{k,\lambda} a_{k,\lambda}$, and the last term is the semi-classical atom-field interaction; $H_{AF} = -e\overrightarrow{E}(\overrightarrow{r}, t).\overrightarrow{r}$. After applying the RWA and assuming the atom to be at rest, the interaction term can be re-written as $H_{AF} = \sum_{k,\lambda} i\hbar(g_{k,\lambda} a_{k,\lambda}|e\rangle\langle g| + g^{*}_{k,\lambda} a^{\dagger}_{k,\lambda}|g\rangle\langle e|)$, where $g_{k,\lambda}$ is the coupling constant between the two states. The Master equation for the atom's density matrix ρ_A is found by starting with the Von Neumann equation for the total system, applying the Markov approximation, and tracing over the radiation field B. The time evolution for the atom's density matrix $\rho_A = Tr_B(\rho_{AB})$, as expected for a Markov process, has the form

$$\frac{d\rho_A}{dt} = -\frac{i}{\hbar}[H_s, \rho_A] + D(\rho_A), \tag{2.22}$$

where the Hamiltonian H_s describes the coherent evolution of the atom, such as stimulated emission and absorption. The Lindbladian dissipation term $D(\rho_A)$ accounts for spontaneous emission,

$$D(\rho_A) = \gamma_-(\sigma_-\rho_A\sigma_+ - \frac{1}{2}\{\sigma_+\sigma_-, \rho_A\}), \tag{2.23}$$

where $\sigma_+ = |e\rangle\langle g|$, $\sigma_- = |g\rangle\langle e|$, $\gamma_- = \gamma$ is the rate of spontaneous emission, also referred to as the linewidth of the transition. Note that the interaction with the vacuum field does not allow spontaneous absorption ($\gamma_+ = 0$). Solving this equation gives the following optical Bloch equations (OBE),

$$\begin{aligned}
\frac{d\rho_{gg}}{dt} &= +\gamma\rho_{gg} + \frac{i}{2}(\Omega^*\rho_{eg} - \Omega\rho_{ge}) && (2.24)\\
\frac{d\rho_{ee}}{dt} &= -\gamma\rho_{ee} - \frac{i}{2}(\Omega^*\rho_{eg} - \Omega\rho_{ge}) && (2.25)\\
\frac{d\rho_{ge}}{dt} &= -(\frac{\gamma}{2} + i\delta)\rho_{ge} + \frac{i}{2}\Omega^*(\rho_{ee} - \rho_{gg}) && (2.26)\\
\frac{d\rho_{ge}}{dt} &= -(\frac{\gamma}{2} + i\delta)\rho_{eg} + \frac{i}{2}\Omega^*(\rho_{gg} - \rho_{ee}) && (2.27)\\
& && (2.28)
\end{aligned}$$

where $\rho_{ij} = \langle i|\rho|j\rangle$, $\rho_{ge} = \rho_{ge}e^{-i\delta t}$, γ is the natural linewidth, Ω is the Rabi-frequency, and δ is the detuning of the incident laser field. Note that not all the parameters in the OBE are independent, since the population of a closed two-level system is conserved we have; $\rho_{ee} + \rho_{gg} = 1$. Furthermore this implies that $d\rho_{ee}/dt = -d\rho_{gg}/dt$.

We now wish to find the steady-state solutions of the OBE by setting the time derivatives to zero and additionally utilizing certain relationships among the real independent parameters of ρ for a two level system. As indicated above, the conservation of population eliminates one parameter, and two of the others are complex conjugates of one another; $\rho_{eg} = \rho_{ge}^*$. Defining the population difference $P \equiv \rho_{gg} - \rho_{ee}$, the OBE now reduce to

$$\begin{aligned}
\frac{d\rho_{eg}}{dt} &= -(\frac{\gamma}{2} - i\delta)\rho_{eg} + \frac{i}{2}\Omega P, && (2.29)\\
\frac{dP}{dt} &= -\gamma P - i(\Omega^*\rho_{eg} - \Omega\rho_{ge}) + \delta. && (2.30)
\end{aligned}$$

The steady-state case has $\frac{d\rho_{eg}}{dt} = \frac{dP}{dt} = 0$, hence the above equations can be solved for P and ρ_{eg},

$$P = \frac{1 + (2\delta/\gamma)^2}{1 + s_0(2\delta/\gamma)^2} \tag{2.31}$$

$$\rho_{eg} \quad = \quad \frac{i\Omega(1+(2\delta/\gamma)^2)}{2(\gamma/2-i\delta)(1+s_0(2\delta/\gamma)} \tag{2.32}$$

where $s_0 = 2(|\Omega|/\delta)^2$ is the on-resonance saturation parameter.

We started out this chapter with the partial aim of explaining laser cooling. Now with the optical Bloch equations we can calculate the total radiation pressure exerted by the light field on the atom and subsequently explain how the atoms are cooled.

Since the population in the excited state decays at a rate γ, and the excitation and decay rates are equal in the steady state, the total scattering rate for an atom at rest is given by $\gamma_{sc} = \gamma\rho_{ee}$. Where ρ_{ee} is calculated as,

$$\rho_{ee} = \frac{1}{2}(1-P) = \frac{s_0/2}{1+s_0+(2\delta/\gamma)^2}, \tag{2.33}$$

Recalling that in a single scattering event the atom gains on average a total momentum kick, $\triangle\overrightarrow{p} = \hbar\overrightarrow{k}$, the resulting average scattering force or radiation pressure exerted by the light field on the atom is given by $\overrightarrow{F}_{sc} = \Delta\overrightarrow{p} = \gamma_{sc}\hbar\overrightarrow{k}$. F_{sc} is simply the average force of absorption followed by spontaneous emission. The preceding discussions and calculations have been carried out for an atom at rest, however, if we wish to slow atoms down and therefore we need to consider atoms that are not at rest but have a velocity $\overrightarrow{v}$. Since these atoms are moving in the laser field they are subject to the Doppler effect and "see" the frequency of the laser Doppler shifted as, $\delta' = \delta - \overrightarrow{k}\overrightarrow{v}$. Substituting in the effective detuning, the (average) scattering force of a traveling monochromatic plane wave for a perfect two-level atom moving with velocity $\overrightarrow{v}$ is

$$\overrightarrow{F}_{sc} = \gamma\frac{s_0/2}{1+s_0+(2(\delta-\overrightarrow{k}.\overrightarrow{v})/\gamma)^2}\hbar\overrightarrow{k}. \tag{2.34}$$

This scattering force which is necessary for laser cooling, is the largest for $\delta' = 0$. Note that the force is dissipative in nature because the opposite of spontaneous emission is not possible, and therefore the action of the force cannot be reversed.

2.5 Doppler Cooling

In the quest for cooling atoms as much as possible the Doppler shift can be a useful tool. By irradiating a gas of atoms from both sides with laser beams tuned slightly below the atomic resonance frequency, $\delta = \omega_l - \omega_0 < 0$, a technique known as Doppler cooling can be realized. A schematic of the method is illustrated in Fig. 2.3. For an atom moving in this laser configuration, the laser beam opposing its motion is Doppler shifted toward the atomic resonance frequency, whereas the laser beam directed along its motion is Doppler shifted further from resonance. The atom therefore absorbs more strongly from the laser beam that opposes its motion and slows down. If one applies three pairs of orthogonal cooling beams, cooling will result in all three dimensions. This method has been coined "Doppler" cooling for obvious reasons.

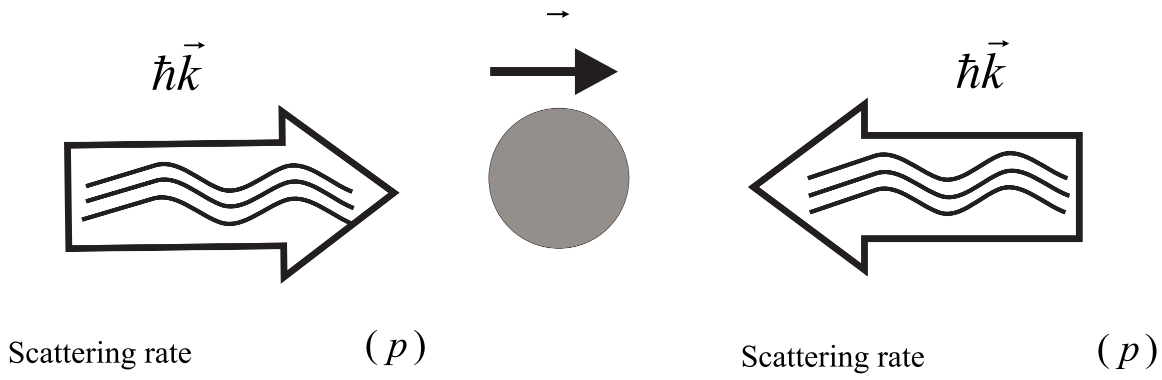

Figure 2.3. Schematic of doppler cooling.

To further study the behavior of an atom in such a laser field configuration we first assume that the two counter-propagating laser beams are independent, meaning no interference occurs between them and absorptions from one beam are not proceeded by stimulated emissions into the other. The total scattering rate due to a beam directed opposite to the atom's motion is

$$\gamma_{p\mp} = \gamma \frac{s_0/2}{1 + s_0 + (2(\delta \pm kv)/\gamma)^2} \tag{2.35}$$

In the low beam intensity limit. If we assume, $s_0 \ll 1$, which is often the case for most experimental conditions, the scattering rate can be further approximated as:

$$\gamma_{p\mp} = \gamma \frac{s_0/2}{1 + (2(\delta \pm kv)/\gamma)^2}. \tag{2.36}$$

Note that the scattering rate $\gamma_{p\mp}(v)$ is equivalent to the probability, $\epsilon_{\mp}(p)$, that the atom will receive a momentum kick $\mp\hbar k$. Hence, the random walk model developed earlier is most useful to describe the behavior of an atom irradiated by two counter-propagating laser beams. For a 1-dimensional system, taking into account all approximations made up to this point, the total average force on the atom is

$$F = [\epsilon_+(p) - \epsilon_-(p)]\hbar k = \frac{\hbar k\gamma}{2} s_0 \frac{kv}{\gamma} \frac{16\delta/\gamma}{1 + \frac{8}{\gamma^2}(\delta^2 + (kv)^2) + \frac{16}{\gamma^4}(\delta^2 - (kv)^2)^2} \tag{2.37}$$

Figure 2.4 plots this equation for the two conditions, (a) $\delta = -\gamma/2$, and (b) $\delta = -\gamma$. According to Eq. (2.37), if $\delta > 0$ the atoms will accelerate, hence from here on we will only consider laser detunings, $\delta < 0$ for which F becomes a frictional force. In the limit of small velocities for which, $|kv| << \delta$ or $|kv| << \gamma$, Eq. (2.37) is reduced to

$$F = 4\hbar k s_0 kv \frac{2\triangle/\Gamma}{[1 + (2\triangle/\Gamma)^2]^2} = -\alpha v. \tag{2.38}$$

The above equation now depicts F as a linear friction force where α is the damping coefficient. The dependency of the force on velocity, resulting in viscous damping has coined the term “optical molasses” for this technique. We can now find the dispersion as

$$D = \frac{1}{2}[\epsilon_+(p) + \epsilon_-(p)](\hbar k)^2 = (\hbar k)^2 \frac{\gamma}{2} \frac{s_0}{1 + (2\delta/\gamma)^2} = (\hbar k)^2 \gamma_{sc} = D_0, \tag{2.39}$$

which is a constant. Knowing α and D we can now solve Eq. (2.12) which results in

$$\overline{W}(p) \propto exp(\frac{\alpha p^2}{2D_0 m}), \tag{2.40}$$

where m is the mass of the atom. This distribution is Maxewellian where

$$v_{rms}^2 = \frac{p_{rms}^2}{m^2} = \frac{D_0}{\alpha m} = \frac{\hbar\gamma}{4m} \frac{1 + (2\delta\gamma)^2}{(2\delta/G)} \tag{2.41}$$

Furthermore, we know the cooled atoms can be characterized as having a thermal temperature of, $T = mv_{rms}^2/kB$. Hence from Eq. (2.41) we find the lowest temperature as $K_BT_D = \hbar\gamma/2$, often referred to as the Doppler temperature or Doppler limit. This is achieved for a detuning of $\delta = -\gamma/2$. Typically, this temperature is on the order of several hundred μK (120 μK for rubidium) and is 2-3 orders of magnitude above the recoil limit $T_{recoil} = \hbar k/m$, which is typically on the order of a few μK (1.2 μK for rubidium). It is necessary to emphasize that the Doppler temperature we derived here is technically only valid in the low intensity limit. However, even Doppler cooling models that incorporate higher intensities do not predict lower temperatures. As such, the Doppler temperature above is theoretically the lowest possible for Doppler cooling. What was surprising was experiments which showed much colder temperatures. This was specially unusual since the limits of an experiment are generally determined by technical noise and are therefore higher than the theoretical predictions. In response to the unexpected observations, two groups [113,114] developed models that explained the lower temperatures. In the previous calculations, for the sake of simplicity we assumed a two level atomic model. However it turns out the multiplicity of sublevels of an atomic state cannot be ignored. These so-called sub-Doppler mechanisms still rely on spontaneous emission as the dissipative process and therefore are ultimately bound by the recoil limit. This limit is introduced since the random emission of a photon introduces an uncertainty $\hbar k$ in the atom's momentum.

However, to observe the BEC transition, much lower temperatures ($\approx$ 200nK) are required. Going beyond the recoil limit required implementing other techniques, such as evaporative cooling or Raman cooling. Ultimately, evaporative cooling lead to the observation of the first BEC and other methods have yet to be proven successful. The following section will briefly review the working foundations of evaporative cooling.

2.6 Evaporative Cooling

Evaporative cooling was first suggested by Harold Hess [115] as an efficient way to cool trapped atoms [116,117] beyond the the limits of laser cooling techniques. His idea was based on the preferential removal of those atoms from a confined sample with energies higher than the average, followed by re-thermalization of the remaining atoms by elastic collisions. His original work was focused on trapped atomic hydrogen, but in 1994 the technique was extended to alkali atoms by combining evaporative cooling with laser cooling [118]. Very soon after the first implementation of this technique evaporative cooling was employed in the observation of the first BEC [78,119,120]. Cooling an atomic cloud through evaporation involves using either a magnetic trap or a far-off-resonant optical field. We will concentrate on the latter technique since this is what was used int he experiments presented here.

Far off-resonant optical dipole traps (FORTs) [121] rely on the principle that an off-resonant laser beam attracts or repels atoms depending on whether it is red or blue detuned. The trap depth depends on the ratio of the laser intensity divided by the detuning, whereas the spontaneous rate of light scattering scales as the intensity divided by the square of the detuning. Therefore, heating due to spontaneous scattering is considerably suppressed for higher detunings [122].

Different approaches modeling evaporative cooling have been introduced, a detailed simulation is given by Doyle and coworkers [123,124] which includes various cooling, heating and loss processes. Davis *et al.* [125] approximated evaporative cooling as a discrete series of truncation and rethermalization processes. Monte Carlo trajectory techniques were also used by Holland *et al.* [126], Wu, and Foot [127], to directly simulate the evaporation process. In general, most of the dynamics of evaporative cooling is modeled following simple considerations. Here we use the scaling law approach used by O'Hara and coworkers *et al.* [128] to see the effects of evaporation and lowering the potential on physical properties of the trapped atomic cloud.

Let us first assume zero energy to be at the bottom of the trap. The evaporating atoms will have an average energy of $U + \alpha K_B T$, where $\alpha = (\eta - 5)/(\eta - 4)$ [128] and η is the ratio of trap depth to thermal energy. The energy loss rate is then

$$\dot{E} = \dot{N}(U + \alpha K_B T) \tag{2.42}$$

where $\dot{N}$ is the rate at which atoms evaporate from the trap. If trap depth is adiabatically lowered at a rate $\dot{U}$, the total energy of the trap changes. Since the atoms vibrate in a harmonic potential, $E/2$ is the average potential energy. The result is the potential energy changing at a rate of $\frac{\dot{U}}{U}\frac{E}{2}$ with the total energy obeying the evolution equation,

$$\dot{E} = \dot{N}(U + \alpha K_B T) + \frac{\dot{U}}{U}\frac{E}{2}. \tag{2.43}$$

In the classical limit, $E = 3NK_BT$ is the total energy of the trapped gas. Therefore Eq. (2.43) can be rewritten as

$$3NK_B\dot{T} = \dot{N}(U + \alpha K_B T - 3K_BT) + \frac{1}{2}\frac{\dot{U}}{U}3NK_BT \tag{2.44}$$

Solving this equation with a fixed value for η where, $\dot{U} = \eta K_B \dot{T}$, the number of trapped atoms as a function of trap depth will be given by,

$$\frac{N}{N_i} = (\frac{U}{U_i})^{\frac{3}{2(\eta'-3)}}, \tag{2.45}$$

where i refers to the initial condition at $t = 0$ and $\eta' = \eta + \alpha$. As mentioned earlier, reducing the temperature alone is not sufficient for realizing BEC since we need to increase the phase space density as well. To our advantage, evaporative cooling also has the ability to achieve this goal. To illustrate how this works we study the evolution of the phase space density. In the classical regime, the phase space density is

$$\rho = \frac{N(h\nu)^3}{(K_BT)^3} \tag{2.46}$$

where $\nu(t) \propto \sqrt{U}$ is the geometric mean of the trap oscillation frequencies. Using Eq.(2.45) we get

$$\frac{\rho}{\rho_i} = (\frac{U_i}{U})^{\frac{3(\eta'-4)}{2(\eta'-3)}} = (\frac{N_i}{N})^{\eta'-4}. \tag{2.47}$$

The important result of Eq. (2.47) is that the phase space density increases even though particles leave the trap. This shows why evaporative cooling induced by a lowering of the potential depth achieves higher phase space densities. Figure 2.5 is a plot of Eq. (2.47) for $\rho_i = 3 \times 10^{-3}$ and demonstrates how lowering the well depth by a factor of 85, a reasonable factor for optical traps, yields a phase space density of unity. The initial phase space density that we have used in plotting Fig. 2.5 is approximately the same as the phase space density in an optical trap immediately after loading from a MOT. The phase space density versus number of atoms given by Eq. (2.47) is shown in Fig. 2.6. So as far as an experimentalist is concerned, the scaling laws allows one to start from the initial values present in an optical trap and use evaporative cooling to increase the phase space density and still have enough atoms to observe the BEC transition. We need to clarify that for evaporative cooling to work re-thermalization as determined by the elastic collision rate, must be faster than the time scale over which the potential changes. The scattering rate is given by $\gamma = n_0 \bar{v} \sigma$, where $\bar{v} = \sqrt{3K_B T/M}$, n_0 is the peak density, and σ is the scattering cross section. Since $n_0 = \rho/\lambda_{dB}^3$ and $\lambda_{dB} \propto T^{-1/2}$; $\gamma \propto \rho T^2$, therefore,

$$\frac{\gamma_f}{\gamma_i} = (\frac{U_f}{U_i})^{\eta'/2(\eta'-3)}. \tag{2.48}$$

Figure 2.7 shows the evolution of the scattering rate versus trap depth for $\eta = 10$. According to this plot, for the numbers used in this section, the elastic scattering rate reduces by a factor of over 20 by the end of the process. Ultimately this is how the speed of evaporative cooling is determined. This is convincing evidence that evaporative cooling is capable of increasing the phase space density despite the loss of a large fraction of atoms.

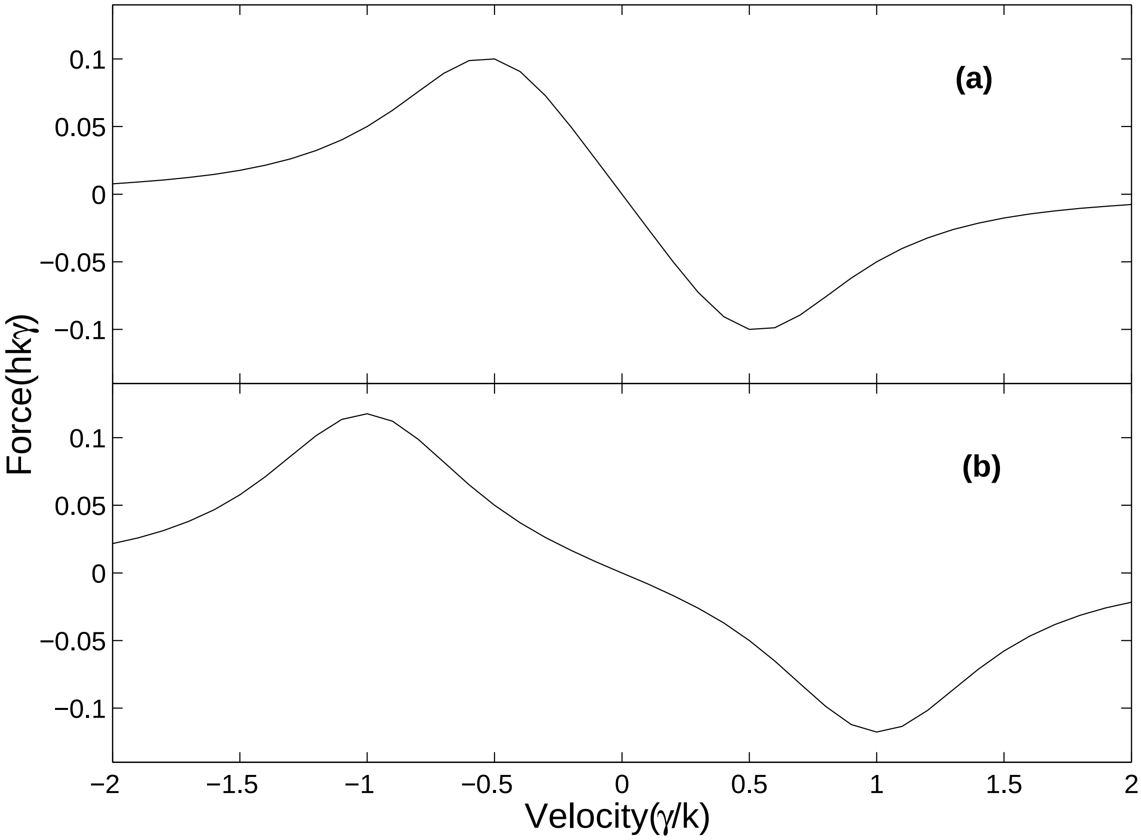

Figure 2.4. The scattering force versus the atom's velocity for (a) $\delta = -\gamma/2$ and (b) $\delta = -\gamma$ in the low intensity limit. Note that in the linear region $v = 0$

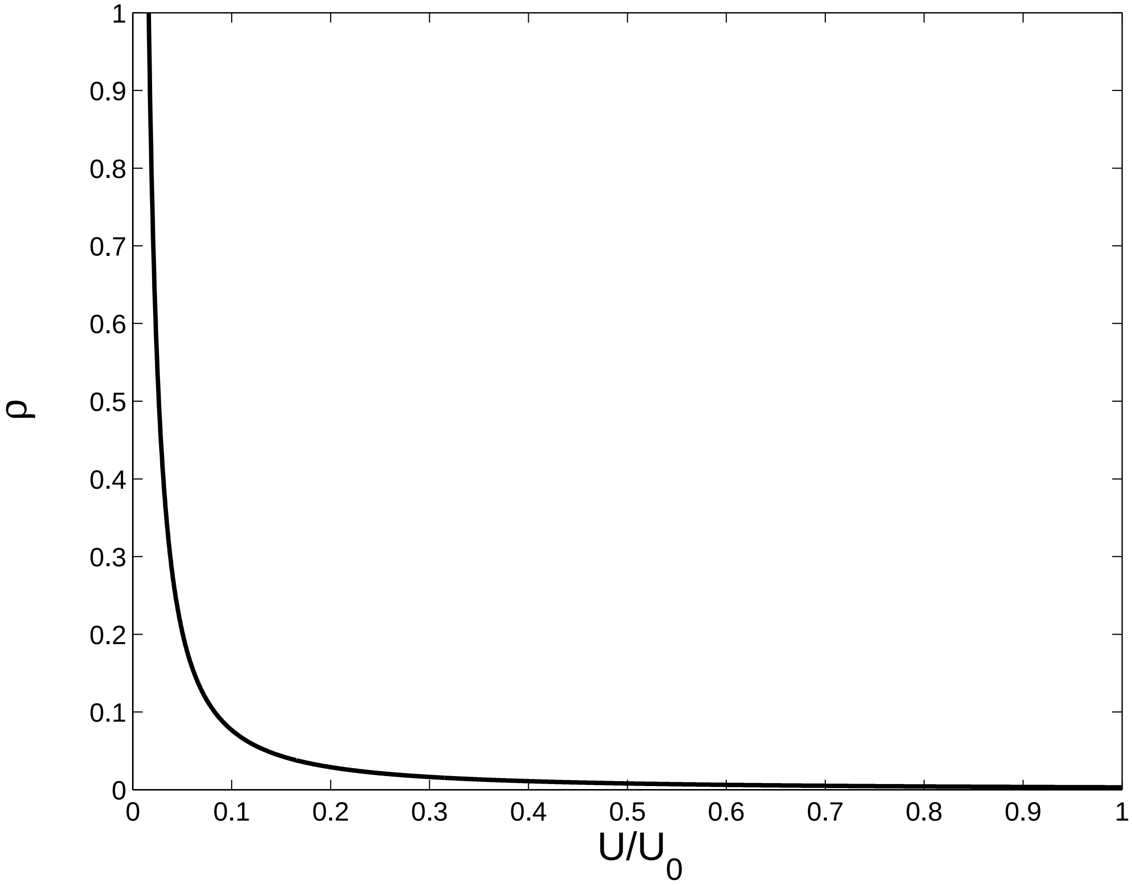

Figure 2.5. Phase space density versus potential depth with $\eta = 10$.

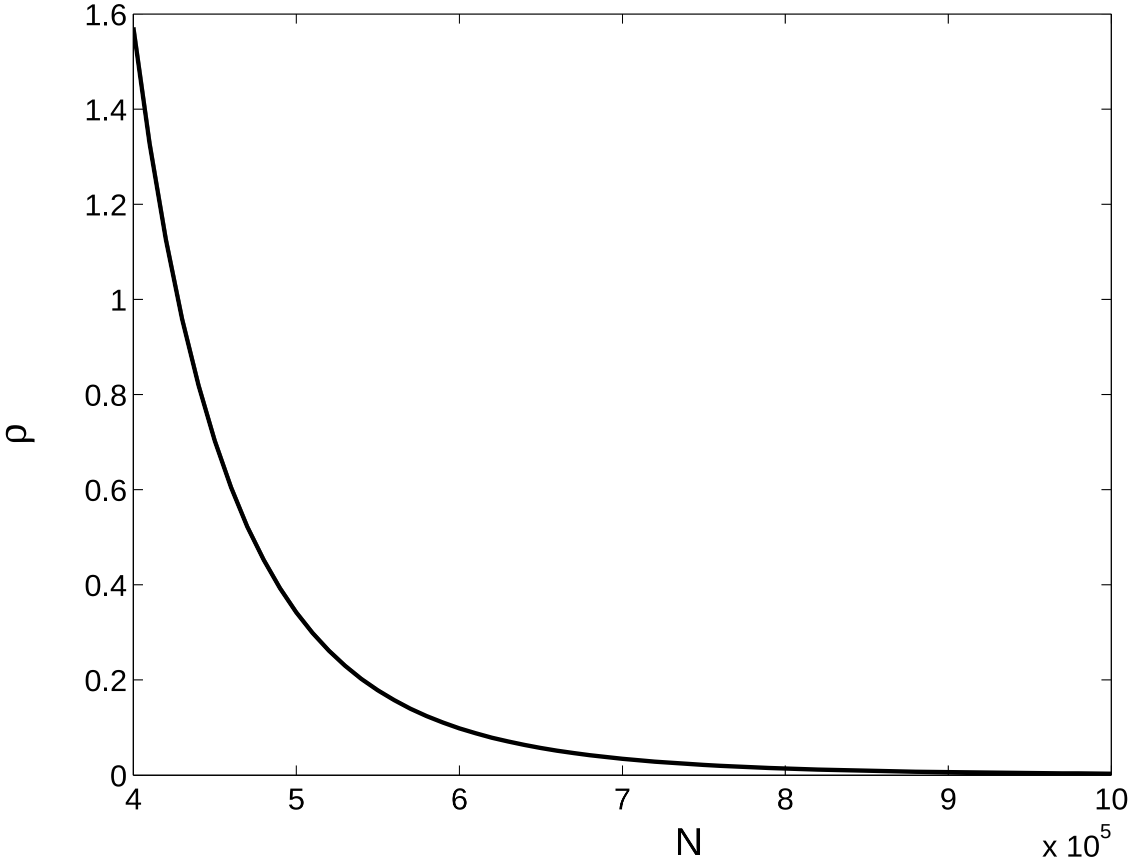

Figure 2.6. Phase space density versus number of atoms in the trap with $\eta = 10$.

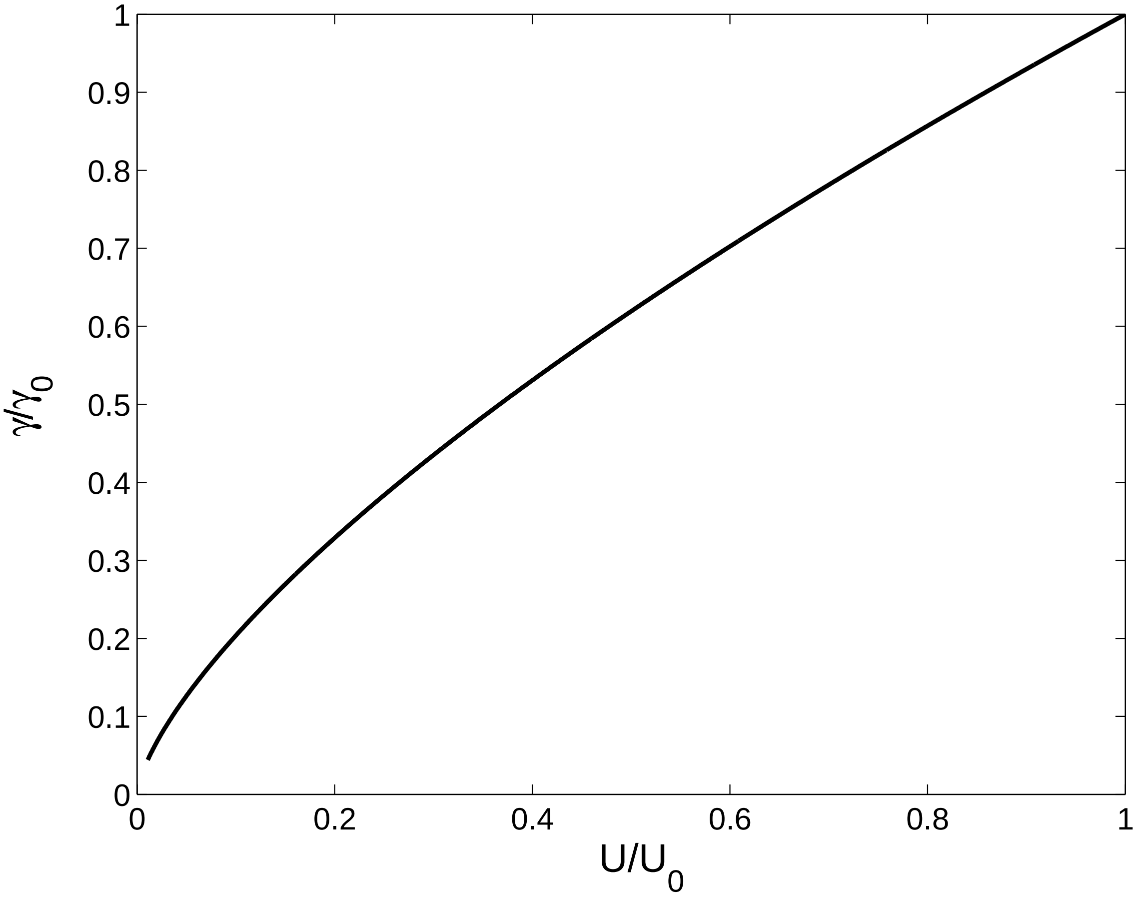

Figure 2.7. Scattering rate versus trap depth with $\eta = 10$.

CHAPTER 3

BOSE-EINSTEIN CONDENSATE

As mentioned in the introduction the main tool for conducting the chaos experiments was a BEC. This chapter will provide an over view of the experimental set up, continuing with a discussion on the important elements in the creation of an all optical BEC

3.1 Experimental set up

3.1.1 Vacuum system

Atoms are collected and cooled to the condensation temperature in a vacuum chamber. The chamber should provide an ultra-high vacuum along with a high number of optical ports that are essential for the experiment. Fig. 3.1 shows a schematic of our vacuum chamber which consists of a six-way cross with an octagonal multiport chamber attached to one of its flanges. Four quartz viewports were used for directing the MOT beams into the chamber and another ZnSe viewports allowed for the transmittance of the 10.6 μm light from a CO_2 laser.

Three Rubidium dispensers from SAES Getters (RB/NF/4.8/17FT10+10) are installed inside the vacuum chamber to provide the source for the Rubidium atoms. A current is applied to the dispenser to release the Rubidium atoms from the metal surface of the dispenser when it reaches a critical temperature. The vacuum gauge and the electric feed through supplying the current for the Rubidium dispenser are connected to a cluster flange. To achieve the ultra-high vacuums needed, one flange is used for the roughing and turbo pumps and another for the ion pump. First a

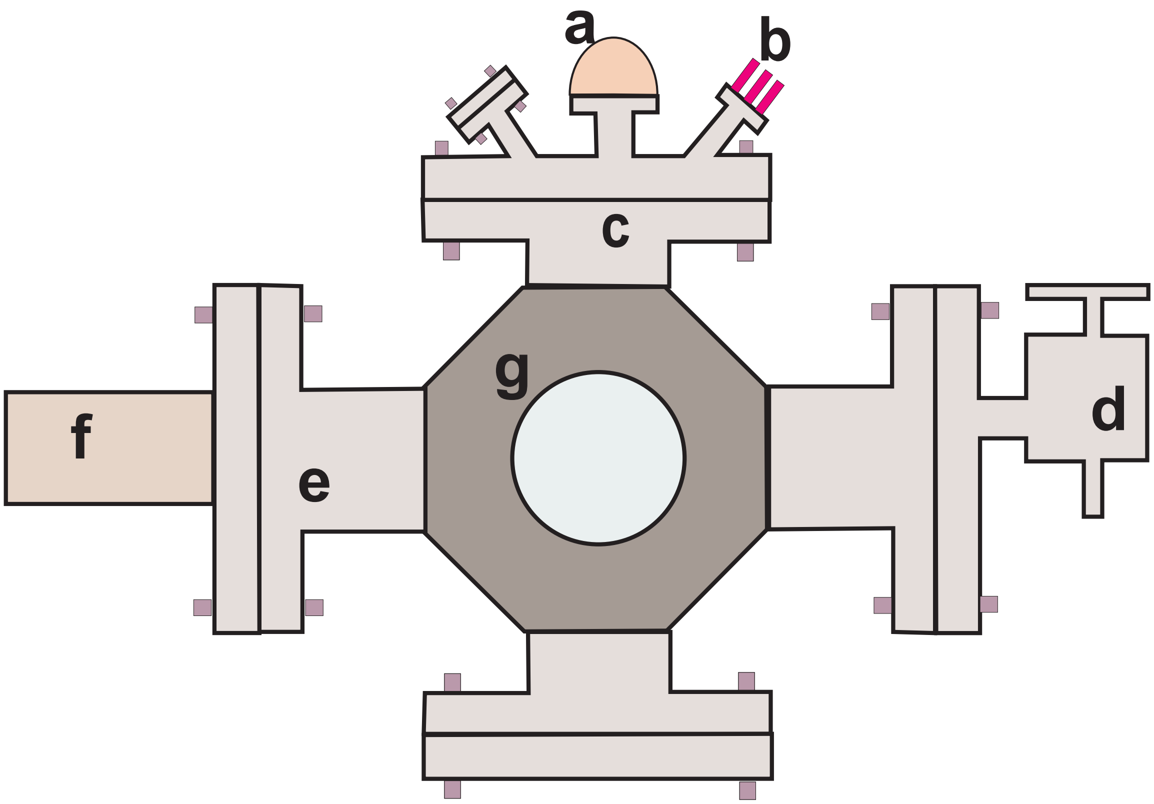

a) Vacuum Gauge

b) Electric feed through.
This supplies
the current through
the Rubidium dispensers.

c) Cluster flange

d) Pump valve

e) Six way cross

f) Ion pump

g) Octagonal chamber

Figure 3.1. Vacuum chamber apparatus.

Travac-b rotary vane pump was used as a roughing pump which brings the pressure down to about 0.1 Torr. Subsequently, a Turbo-molecular pump was switched on to bring the pressure down to the high-vacuum range. Simultaneously, we started a bake out where the chamber was thermally isolated and electric heaters were used to raise the temperature to 200^o C. The heating was continued for 3 days to ensure that water and other impurities outgassed from the chamber's walls. At this stage we were able to achieve a pressure of about 10^{-8} Torr. Finally, a Varian Valcon Plus 55 ion pump was used for further pumping the chamber which lowered the pressure to 10^{-11} Torr. The vacuum chamber was kept at this pressure for all the experiments conducted for this thesis.

3.1.2 Magneto-Optical Trap

The magneto-optical trap (MOT) has provided an efficient and straightforward way to capture and cool millions of atoms to the micro-Kelvin regime. In BEC experiments the MOT provides an increase in the atomic cloud density by a factor of over 10^9 from ambient conditions and provides favorable initial conditions for subsequent evaporation to quantum degeneracy. The standard MOT consists of three orthogonal pairs (making a total of six beams) of counter-propagating circularly polarized laser beams and a pair of anti-Hemholts coils. The laser beams are detuned to the red of the cycling transition by a few atomic linewidths for Doppler cooling. The anti-Hemholtz coils (MOT coils) create a spatially varying Zeeman shift for the laser cooled atoms. The combination of the MOT coils and cooling lasers creates a spatial-dependent and velocity dependent radiation pressure that provide both a restoring and viscous force for the atoms.

To create the MOT cooling beams a series of semiconductor laser diodes were used in a master-slave configuration. Figure 3.2 shows the diode laser setup to create the MOT. A grating stabilized "Toptica Photonics DL 100" diode laser with 15 mW

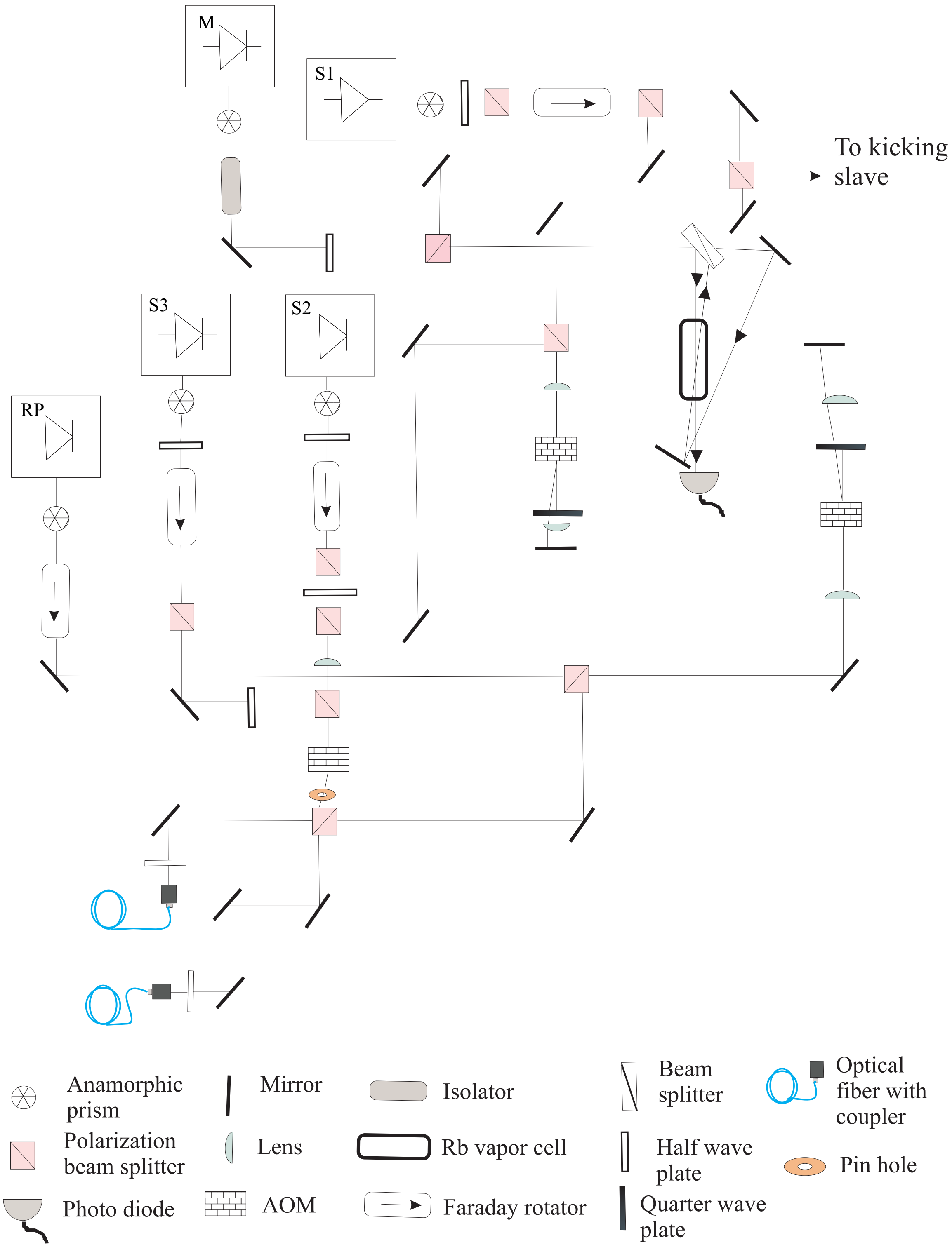

Figure 3.2. Diode laser setup for MOT creation. S1, S2, and S3 are slaves 1 to 3. M and RP are the master and repump lasers respectively

output power served as a master laser. This laser was locked to the cross-over transition close to the $F = 2 \rightarrow F' = 3$ and $F = 2 \rightarrow F' = 2$ transition of ^{87}Rb atoms. Figure 3.3 depicts the various transition lines used for our experiment. A homemade high power laser was used as a slave (slave 1) by having the master laser beam injected into it. Slave 1 had an output power of about 110 mW and was divided into two beams for two different experiments. One of these beams was used to injection lock another 110 mW diode laser (slave 2). Note that this beam was directed to the slave laser after passing through a single pass and a double pass Aqusto-Optic-modulator (AOM). The output of slave 2 passes through another single pass AOM before coupling to the optical fiber. The combination of these two AOMs brings the light near to the resonance with the $F = 2 \rightarrow F' = 3$ transition. By changing the frequency of the double pass AOM we can tune the frequency of the slave laser from on resonant to -90 MHz of the $F = 2 \rightarrow F' = 3$ transition. These frequencies are required for MOT loading, FORT loading and BEC imaging stages. Note that we have injection locked another diode laser (slave 3) to slave 2 laser in order to increase the available power for MOT creation. The laser beams from slave 2 and 3 are coupled to two separate optical fibers, after the single pass AOM, which transmits them onto the optical table where the vacuum chamber sits. These two beams are then divided into three beams which are then expanded into a beam of size 2.2 cm in diameter and directed into the vacuum chamber through the quartz view ports. The intersection region between the laser beams inside the chamber was the volume in which the MOT was realized which captures up to 10^7 rubidium atoms.

Although the MOT laser frequency is tuned close to the $F = 2 \rightarrow F' = 3$ transition, there is a small probability that the atoms can be excited to the $F' = 2$ state, which can spontaneously decay to the $F = 1$ ground state. Due to the large ground state hyperfine splitting (6.8 GHz), atoms in the $F = 1$ state are decoupled from the cooling light. To repump these atoms, a second laser resonant with the

$F = 1 \rightarrow F' = 2$ transition is added to optically pump the atoms back to the $F = 2$ state; this is referred to as the repump laser.

3.1.3 Magnetic coils for MOT

To provide the magnetic field required for the MOT, a set of water cooled anti-Helmholtz coils (main coils) were built. Each of the coils had a diameter of 22.5 cm with 86 turns of wire carrying 12 A of current. The separation between the coils was 12.5 cm. These coils made a magnetic field with a gradient of approximately 15 G/cm. To cancel out the effect of stray magnetic fields we used a pair of Helmholtz coils in each direction (nulling coils). We found that zeroing the B-field at the position of the optical trap is crucial for its optimal loading. The main coils were mounted on to translation stages to provide control over the position of the coils. The optimal position of the coils was determined by changing the nulling coil's current and monitoring the expansion of the MOT (by switching off the current on the main coils) to find the place where the MOT expands symmetrically after turning the B-field off.

3.1.4 Optical Dipole Trap

Figure 3.4 shows a schematic of the set up for the optical dipole trap. The light for the optical trap originated from a 50 Watt RF excited CO_2 laser. The output beam of the laser passed through an AOM where the zeroth order was directed to a beam dump. The first order was directed toward the vacuum chamber. Two ZnSe viewports were used to transmit the the CO_2 laser beam into and out of the vacuum chamber. We have mounted 4 aspheric ZnSe lenses with a 37 mm focal length inside the chamber in order to tightly focus the CO_2 for rapid evaporative cooling. The AOM is driven by amplified 40 MHz RF signals. The 40 MHz RF signal passed through two MiniCircuit electronics attenuators before entering the amplifier. The controllers of the attenuators were connected to separate analog terminals controlled by a computer. Depending on the voltage applied to the controllers the RF power

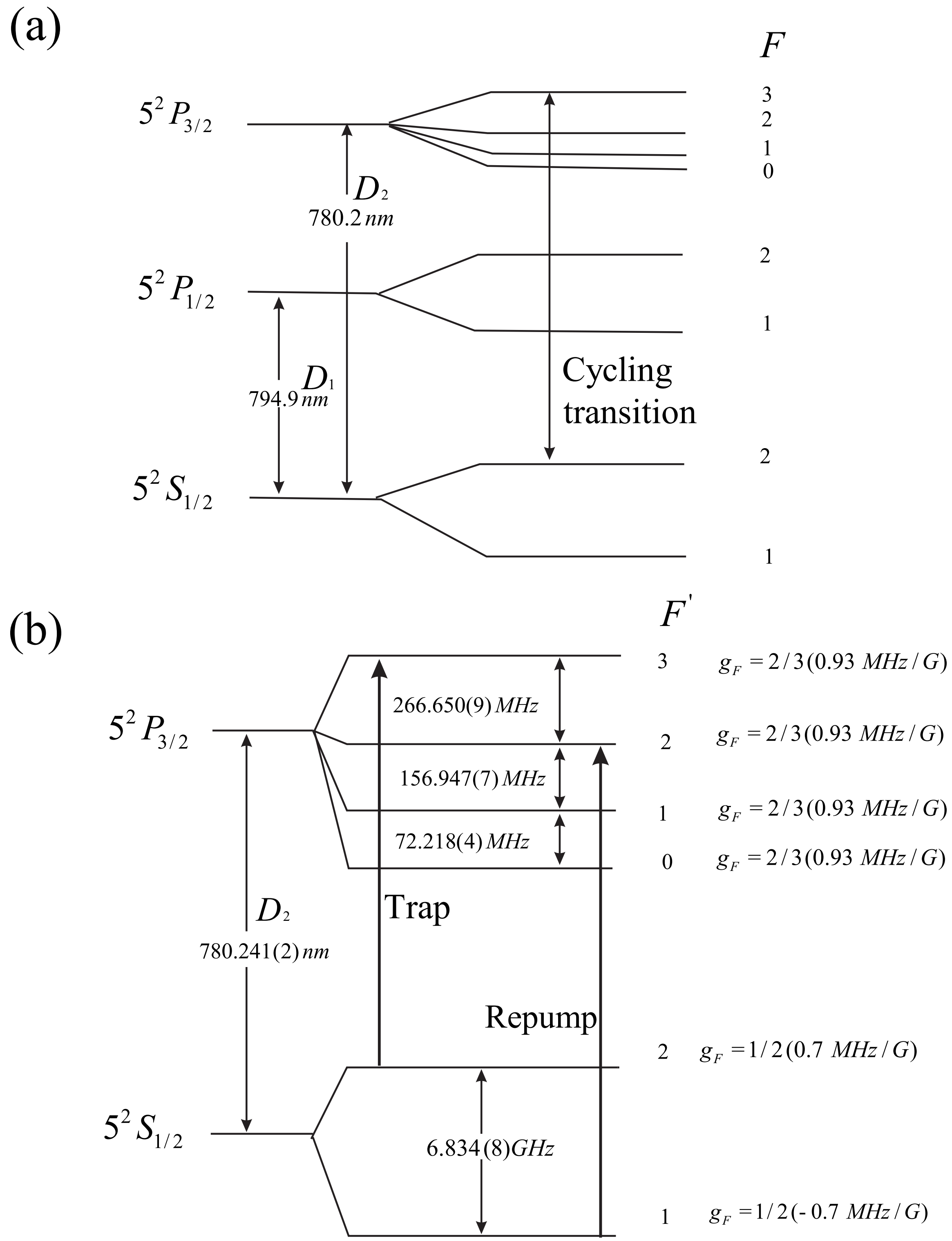

Figure 3.3. (a) ^{87}Rb Dtransition hyperfine structure. (b) Detailed D2 transition hyperfine structure. The master laser was locked to the cross-over transition of $F = 2 \rightarrow F' = 3$ where the repumper laser was locked to the cross-over transition of the $F = 1 \rightarrow F' = 2$.

changed, giving us computer control of the total power and hence the optical traps well depth. This enabled us to perform forced evaporative cooling of the trapped atoms. This attenuator was also used to switch off the optical trap in less than 1 μs. The CO_2 beam was directed horizontally into a vacuum chamber and passed through a 2× beam expander with the second lens mounted on a translational stage. The stage is an AeroTech ATS100-50 Motorized Linear Stage bought second hand from Surpluseq. The travel length is 4 inches long with a maximum speed of 30 mm/s and has a 101 SMB2-HM stepper motor. The stage was controlled with a motion controller called the Soloist MP bought from Aerotech. The Soloist has its own computer interface and also includes support for Labview, making the travel motion of the stage easily programable. A 3.8 cm focal length aspheric lens, mounted inside the vacuum chamber, focused this beam onto the MOT. Initially the telescope lens's separation was set to create an optical trap with a broad waist of a 100 μm to optimize the loading efficiency [77] (see Fig. 3.4 for a schematic of this set up).

Since the CO_2 beam frequency is far-off-resonant from the electronic transition frequency of the Rb atoms, it was very difficult to align the beam with the MOT. We developed the following alignment procedure to overlap the CO_2 laser trap with the MOT. Initially, a 780 nm laser beam (probe beam) is aligned on top of a He-Ne laser. The probe beam was aligned such that it destroyed the MOT when we allowed it into the chamber. By burning a hole in a piece of paper with the CO_2 laser beam, we could overlap the CO_2 beam along the same path as the He-Ne beam and therefore ensure the beam passed close to the MOT. Since the Rayleigh length of the optical trap is short and the focus is tight, this method does not locate the focus of the beam on the MOT at first try. For final alignment, the CO_2 beam was turned on and off periodically and the MOT was moved using the nulling coils until the fluorescence intensity changed in the MOT. This was monitored direclty on an inexpensive CCD camera that normally monitors the MOT. However this technique is not sufficient when the MOT was big enough to saturate the CCD camera. To overcome this problem the detuning of the MOT light was increased from resonance.

3.1.5 Kicking beam

For the experiments reported in Chapters 4 and 5 the BEC was subjected to a pulsing standing beam of light after the CO_2 light was turned off. Figure 3.5 shows the schematic of the setup. The image inside the chamber shows the effect of a single short pulse on the BEC. The standing wave beam was made with the light used to create the MOT beams. This was accomplished by directing the light into a different path using an (AOM). This light was 6.7 GHz red detuned from the $5S_{1/2}F = 1 \rightarrow 5P_{3/2}F = 2$ transition line of ^{87}Rb and was directed into the chamber at 41° relative to the vertical. The momentum distribution of the BEC after applying the kicks was measured by expanding the condensate for a controlled duration, typically 9 ms, and subsequently destructively imaging using an absorptive technique.

3.1.6 Atom Probe and Signal Collection

The atomic cloud is measured using absorption imaging techniques. A 1:1 imaging system is used to make an image of the cloud's shadow in front of a 4 × microscope objective. For imaging, a horizontal, weak probe laser beam is sent through the cloud and directed through the imaging optics to the cooled CCD camera. For imaging the cloud, the laser frequency and polarization are tuned to drive the $F = 2 \rightarrow F' = 3$ transition. To image the atoms in the F = 1 state, the repump laser is also pulsed during imaging.

3.2 Trap loading studies

The trapping of atoms using light that is far-detuned to the red of an atomic resonance has been the subject of study for almost a decade now [87,129]. Recently

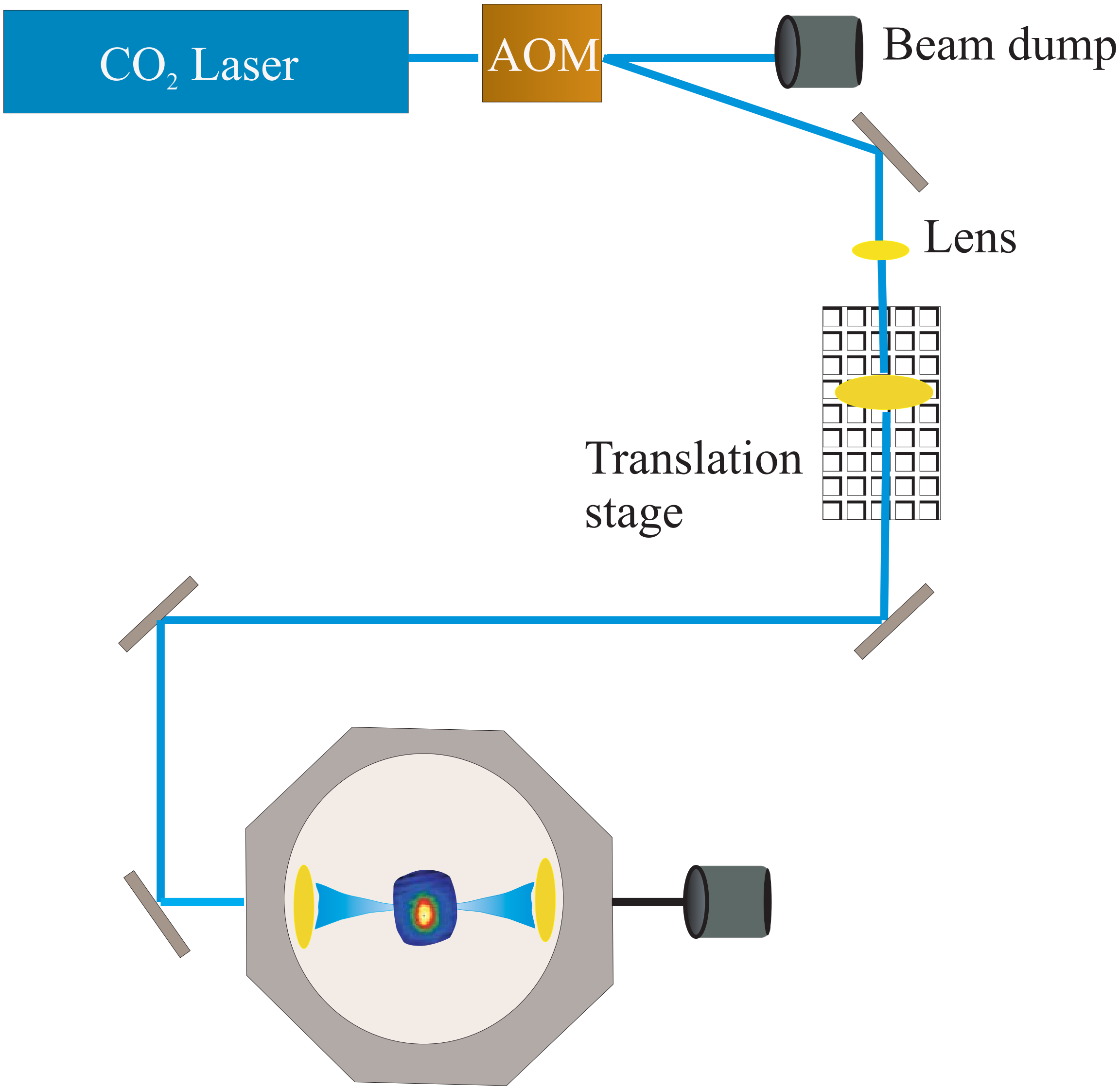

Figure 3.4. Schematic of the optical dipole trap. The CO$_2$ beam was directed into a vacuum chamber in the horizontal direction and passed through a 2× beam expander where the second lens was mounted on a translational stage.

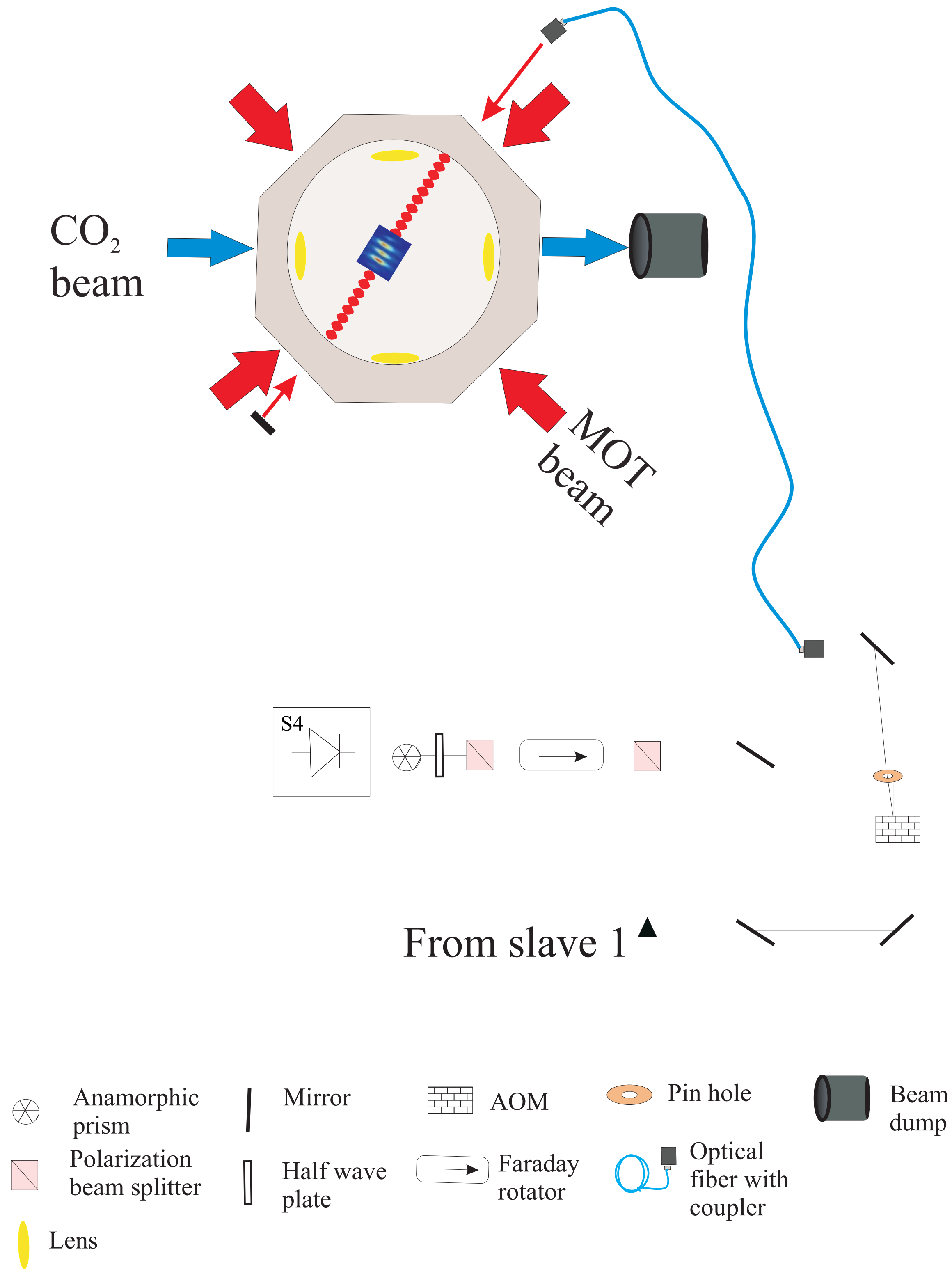

Figure 3.5. Experimental schematic for kicking beam setup.

a resurgence of interest in these far off-resonant optical trap's (FORTs) has led to the all-optical production of BECs of Rubidium [97], Cesium [98] and Ytterbium [130]. A FORT has also been used to produce a degenerate Fermi gas of Lithium [131] and has even formed the basis for the first all-optical atom laser [132]. These optical traps offer several advantages over the traditional magnetic traps that are used to produce BEC; the trapping is not limited to a particular Zeeman sub-state, and the geometry of the trap can be readily adjusted. Furthermore, the tight confinement achievable with a FORT produces high initial elastic collision rates leading to the possibility of rapid evaporative cooling. However, the efficient loading of a FORT still remains a challenge.

Typically in Rubidium FORT experiments, a far off-resonant laser beam from a CO_2 laser is focused onto a collection of atoms that accumulate in a MOT. Although much work has been done to understand the important mechanisms involving FORT loading [133], there are still many aspects of this process that are still unclear. In particular the role of the FORT geometry has received scant attention. As we will see, the FORT volume plays a critical role in determining the number of atoms loaded. However, increasing this volume can lead to reductions in the density and consequently a less useful trap for evaporative cooling. We suggest a way around this problem using a time-averaged potential [134,135].

Our experiment involved investigating the sensitivity of the FORT's loading efficiency to the total power and volume in the optical trap. We began by focusing the CO_2 laser beam into a $35 \pm 5\,\mu$m waist which coincided with the MOT center. Several experiments were performed in which the FORT was loaded with various CO_2 powers. The results of these experiments are shown in Fig. 3.6. This data clearly shows that the number of atoms trapped in the FORT increases slowly as the power becomes larger until about the 20 Watt level. Going beyond this power causes very little change in the number of atoms, since $U_0 \approx 2.5$ mK is much larger than the mean kinetic energy ($\approx 40\mu$K) of the atomic cloud. To observe the effect of the overlap volume on

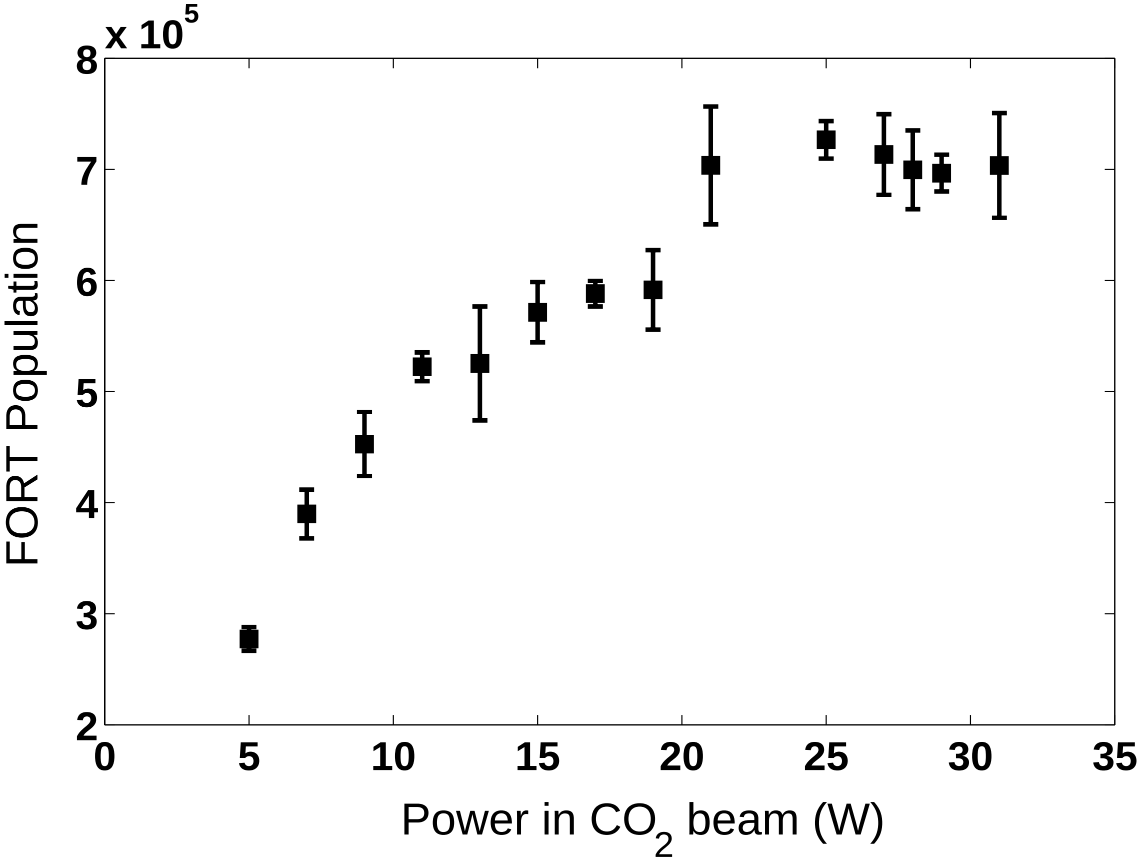

Figure 3.6. Experimental data showing the number of atoms contained in the FORT vs. power in the CO_2 beam. The power is focused to a $35 \pm 5\,\mu$m waist. The MOT population was $\approx 2 \times 10^7$

the FORT population we performed an experiment in which the number of atoms in the FORT was measured as a function of the beam waist of the laser beam. The CO_2 laser beam was passed through a beam expander before the vacuum chamber which consisted of two lenses with 6.35 and 12.7 cm focal lengths. The separation between the lenses were made variable by mounting the second lens on a translation stage. The ABCD matrix method [136] was used to calculate the beam waist corresponding to a specific separation of the lenses. To perform the experiment the lens separation was initially set to a minimum and the FORT was loaded. Subsequently, each data point was obtained by equal increments of the second lens's position. The experimental results are presented in Fig. 3.7. It is clear from these data that there is a significant reduction in the number of atoms trapped in the FORT for smaller beam waists.

3.3 Bose-Einstein condensate in a single beam trap

As mentioned previously, the key to reaching Bose condensation in an all-optical trap is efficient loading, followed by tight confinement for efficient evaporative cooling. This understanding led us to create condensates in a crossed beam trap, consisting of two orthogonal CO_2 laser beams. The tight confinement in the cross trap can lead to high densities and high collision rates, however, this comes at the cost of small trap volumes.

This trap volume limitation limits the initial number of atoms loaded into the trap, and eventually limits the final condensate size to around $5,000$ atoms in the cross trap. Therefore, a larger trap volume is desirable in order to create larger stable condensates. In the previous section we observed that a time averaged optical trap will increase the loading efficiency and damping the sweeping amplitude (adiabatically lowering the power in the CO_2 beams) will provide a tight trap for evaporative cooling. However this method increases the trap volume only in one dimension. A large-waist single focus trap is an ideal alternative for the time averaged traps as it is the simplest trap geometry, and provides a relatively large trap size in all three dimensions. In

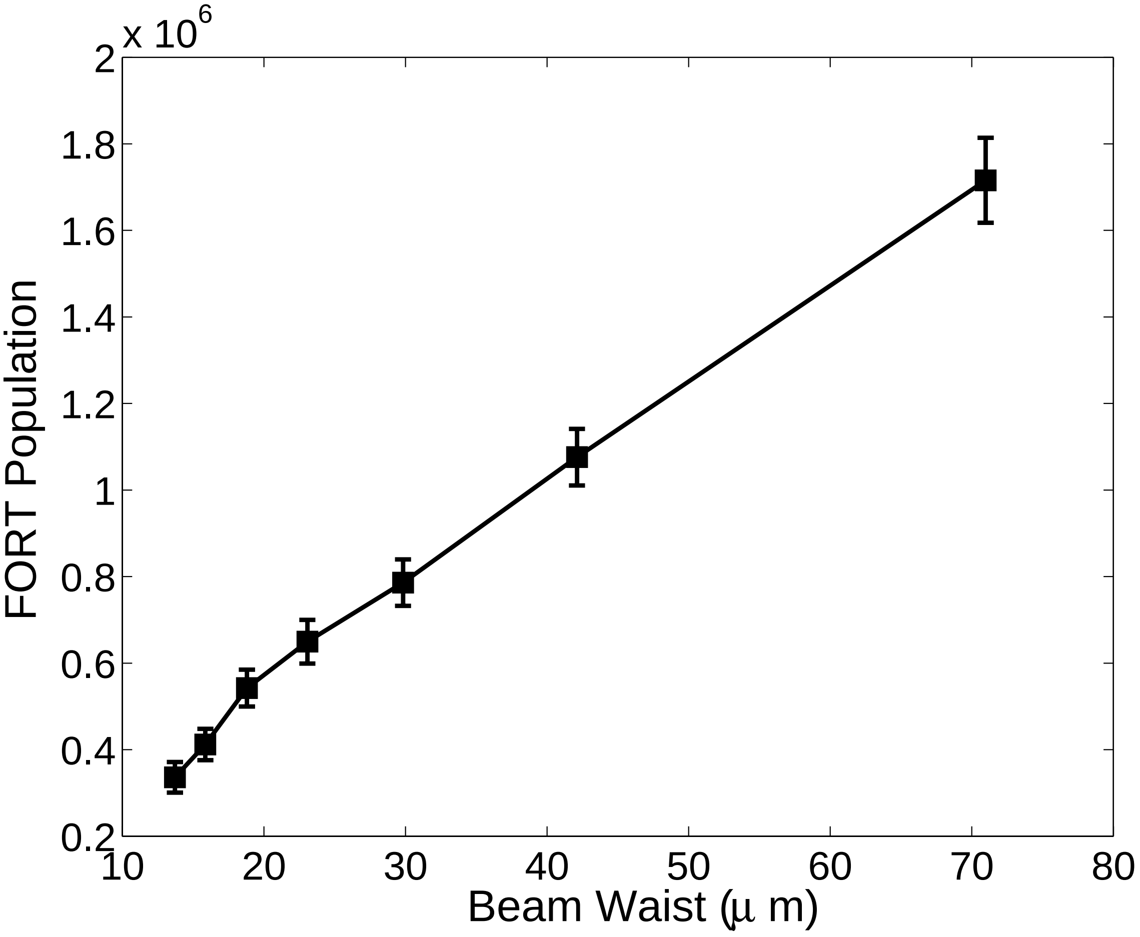

Figure 3.7. Experimental data showing the number of atoms vs. beam waist. The total power in CO_2 beam was 36 Watts.

a recent experiment by Cennini et al., a CO_2 laser was strongly focused to a beam waist of 27μm [137] from which a condensate was created directly in the single focus trap. This tight trap loaded 4×10^6 atoms with an initial density of 1×10^{13}cm^{-3}, and phase space density of 1×10^{-4}. A condensate of $12,000$ atoms was created in this single-focus trap after 7 s of forced evaporation. In a single focus trap, the trap volume scales strongly with the beam waist: $V = \pi w_0^2 z_R \propto w_0^4$, where w_0 is the beam waist at the trap location, $z_R = \pi w_0^2/\lambda$ the Raighly length and λ is the optical trap wave length. The mean trap frequency $\overline{\omega}$ scales as ${w_0}^{-7/3}$. This can be seen from the following relation. In the radial direction and in the harmonic approximation we have

$$\frac{1}{2} m\omega_x^2 w_0^2 = U_0 \propto \frac{1}{w_0^2} \Rightarrow \omega_x \propto {w_0}^{-2}. \tag{3.1}$$

where P is the optical trap's power. The same relation is valid for ω_y. In the propagation direction (z) the relation is

$$\frac{1}{2} m\omega_z^2 w_0^2 = U_0 \propto \frac{1}{z_R^2} \Rightarrow \omega_x \propto {w_0}^{-3} \tag{3.2}$$

therefore the mean frequency is given by,

$$\overline{\omega} = (\omega_x \times \omega_y \times \omega_z)^{\frac{1}{3}} \propto {w_0}^{-7/3} \tag{3.3}$$

Realizing a tight and large volume single focus optical trap seems contradictory at first glance. However, through the cross beam condensate experiment we learned that large volumes for efficient loading and tight confining potentials for efficient evaporative cooling can be separated in time. Therefore, by varying the beam waist w_0 in real time, it is possible to optimize both the efficient loading and the high collision rate in a single focus trap. Specifically, under circumstances where the compression is adiabatic (which is often the case in an optical trap due to its relatively high trap frequencies compared to the speed of compression) the density scales as $n \propto 1/V \propto 1/(w_0^2 \times z_R) \propto {w_0}^{-4}$. The elastic collision rate scales as,,

$$\gamma_{el} \propto n\overline{v} \propto {w_0}^{-4} \times (\frac{P}{w_0^2})^{\frac{1}{2}} \propto {w_0}^{-5}. \tag{3.4}$$

The beam waist of a focused Gaussian beam is given by the formula, $w_0 = \lambda f/(\pi R)$, where λ, f, and R are the wavelength, focal length of the lens, and input beam radius respectively [136]. Therefore, the beam waist can be varied by changing R and/or f. Changing the input beam size of the gaussian beam proves more practical, for it can be easily achieved via a zoom lens telescope. This trap compression technique was first developed by Weiss's group in a crossed YAG laser dipole trap [83], which we adopted to compress our single focus trap. As shown in Fig. 3.8(a), the optical trapping volume is maximized by minimizing the CO_2 beam diameter on the input side of the final lens (L3). The trap is compressed by increasing the beam diameter at L3, which is achieved by translating L2 as shown in Fig. 3.8(b), thus increasing the distance between L2 and L3 ($d_1 < d_2$). The experiment again begins by collecting up to 50×10^6 cold atoms in a MOT. The MOT is overlapped with a large volume single focus trap, formed by a 43 W CO_2 laser beam focused to a waist of 70μm. For better FORT loading efficiencies, the optical trap was left on while the MOT loaded. The repump power was subsequently reduced from 1.5 mW to 0.21 mW to create a temporal dark MOT [77]. After 50 ms the MOT beam detuning was shifted to -90 MHz with respect to the $5S_{1/2}F = 1 \rightarrow 5P_{1/2}F = 3$ transition. After another 50 ms the repump beam was extinguished to leave all of the atoms in the $5S_{1/2}F = 1$ state. After 15 ms the MOT beams and magnetic coils were turned off. Typically 4×10^6 atoms were trapped in the CO_2 beam using this procedure, with a density of $4 \times 10^{13}\text{cm}^{-3}$. Subsequently, the translation stage was moved 16 mm in 1 s so as to reduce the beam waist to 12 μm and compress the optical trap for efficient evaporative cooling [138]. The forced evaporative cooling was carried out by reducing the CO_2 laser beam's power in two steps. In the first step the power was reduced to 1 W exponentially with a decay constant of 0.3 s. The power was then reduced to 80 mW in about 3 s and maintained at this low level for 0.5 s. This created a pure condensate with 45000 atoms in the $5S_{1/2}F = 1, m_F = 0$ state. It is important to note that once the atoms are loaded into the trap, whether or not the evaporative cooling

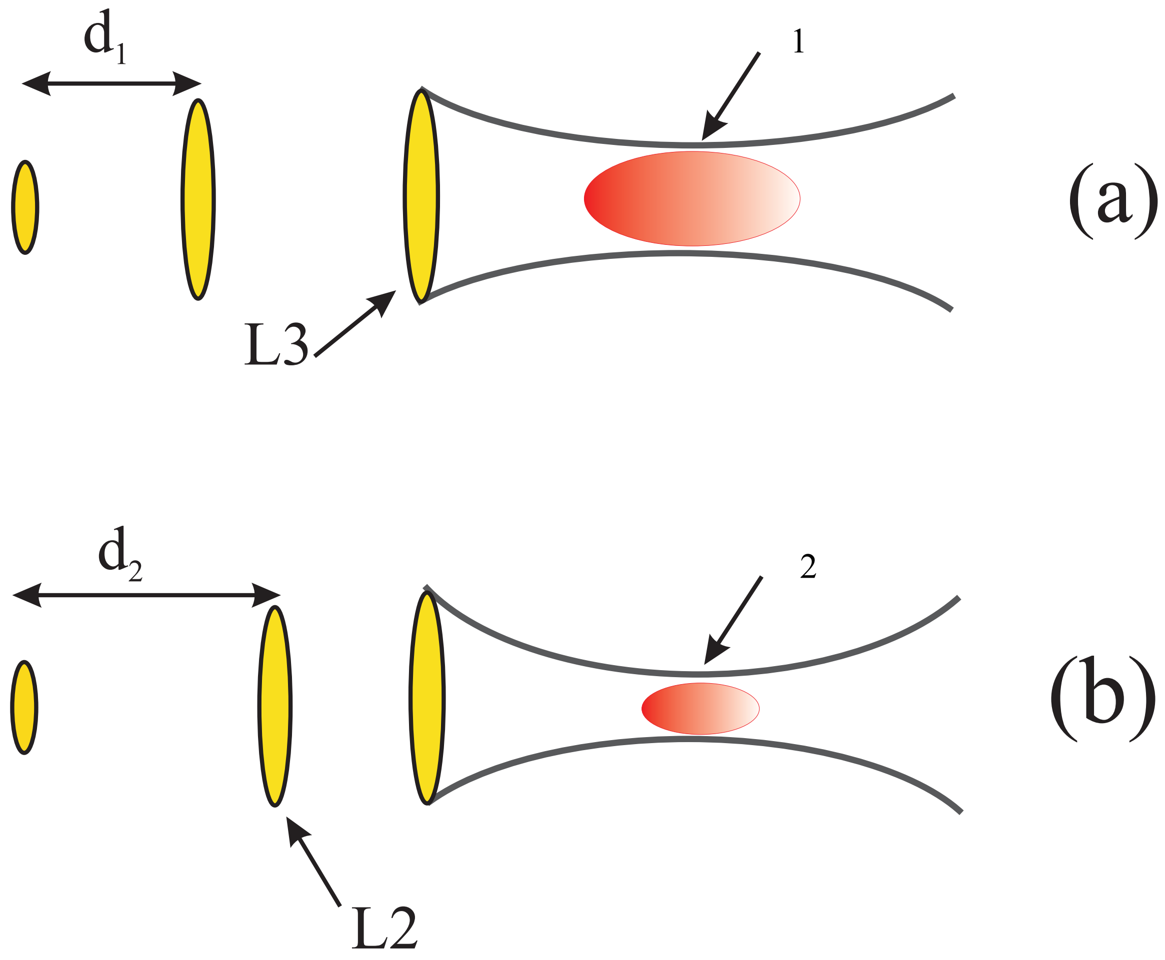

Figure 3.8. Experimental set up for optical trapping. (a) the telescope lens separation set for large trapping volume hence increasing the loading efficiency. (b) The lenses separation was reduced to compress the trapped atoms in the optical trap for efficient evaporative cooling.

is effective is determined by the ratio of elastic collisions amongst the trapped atoms versus other bad collisions such as collisions with untrapped background residual gas molecules. It is therefore crucial to achieve high elastic collision rates in a short time. The smooth changing of the laser focus immediately after loading accomplishes this task.The technique described above for achieving the BEC not only retains the simplicity and speed of our previous methods, but also produces condensates larger than the cross traps.

CHAPTER 4

THEORY OF QUANTUM ACCELERATED MODES

The delta-kicked accelerator (DKA), a periodically driven oscillator coupled to a linear potential, has been widely used to study differing aspects of the transition to chaos [27]. An interesting feature of the DKA was the prediction that there exists trajectories in their phase space that show linear momentum gain with the number of kicks applied to the oscillator. However, such "*accelerations*" appear for cases where the driving force frequency equals the natural frequency of the oscillator. This condition is known as a *resonance* and the result is a large amplitude oscillation.

What is called a quantum delta-kicked accelerator (QDKA) is an extension of the same idea into quantum mechanics where the driving force is applied on a quantum mechanical oscillator in the presence of an external linear potential. For a QDKA a *Quantum resonance* occurs if the plane waves in the kicking direction can acquire a phase factor equal to an integer multiple of 2π during a kicking interval. This concept was first introduced into chaos more than two decades ago with the work of Lichtenberg and Leiberman [139]. But it was not until ten years later that through advancements in laser cooling, quantum accelerator modes were experimentally observed [70]. In this experiment laser cooled atoms were exposed to a corrugated potential from a pulsed off-resonant standing light wave. The quantum accelerator modes then appeared as a fraction of laser cooled cesium atoms that are coherently accelerated by the kicked potential in the direction of gravity. The acceleration was either faster or slower than gravity, depending on the experimental parameters.

Two theoretical models have been developed to explain the observed behavior of the quantum delta-kicked accelerator and particularly to cast light on the creation mechanism of quantum accelerator modes. Godun and coworkers [73] developed a theory based on the interference of the matter-wave. In this model they showed that the corrugated potential acts as a diffraction grating on the matter wave. Therefore, effectively this potential populates different momentum state where the constructive interference between the neighboring momentum states subsequently gives rise to the QAMs. According to this model, only a few of the momentum states accumulate appropriate relative phases between each kick in order to maintain the condition for constructive interference. Although this theory's prediction for the average momentum of the QAMs is in excellent agreement with experiments, it was not possible to directly observe the QAM's momentum states structure due to the low momentum resolution of the experiments utilizing laser cooled atoms.

In a different approach to understand QAMs, Fishman, Guarneri, and Rebuzzini (FGR) [76] developed a pseudo-classical method to study the QDKA (ϵ-classical model hereafter). They showed that a parameter which plays the role of the Planck constant can be scaled with the time deviation of the pulse period from a quantum resonance. Hence for a time interval between kicks close to a resonance, a classical treatment of the QDKA is valid. Using this approach they attributed the QAMs to the stability islands in the Poincaré plot that appear in the underlying pseudo-classical phase space of the QDKA. The most celebrated feature of this model was the prediction of higher order QAMs which was confirmed experimentally shortly thereafter [72]. These were features that the interference model was unable to explain. For experiments utilizing cold atomic samples, the momentum distribution was significantly wider than two recoil momentum and therefore one could not observe the discreteness of the atomic wavefunction after applying standing waves. This experimental limitation and the fact that the interference model failed to predict higher order QAMs has played in favor of the ϵ-classical theory making it the theoretical backbone of QDKA research.

Recently we have been able to observe QAMs using a Bose-Einstein condensate (BEC) [138] (see Fig. 4.1 as an example of the QAM with BEC). The advantage of

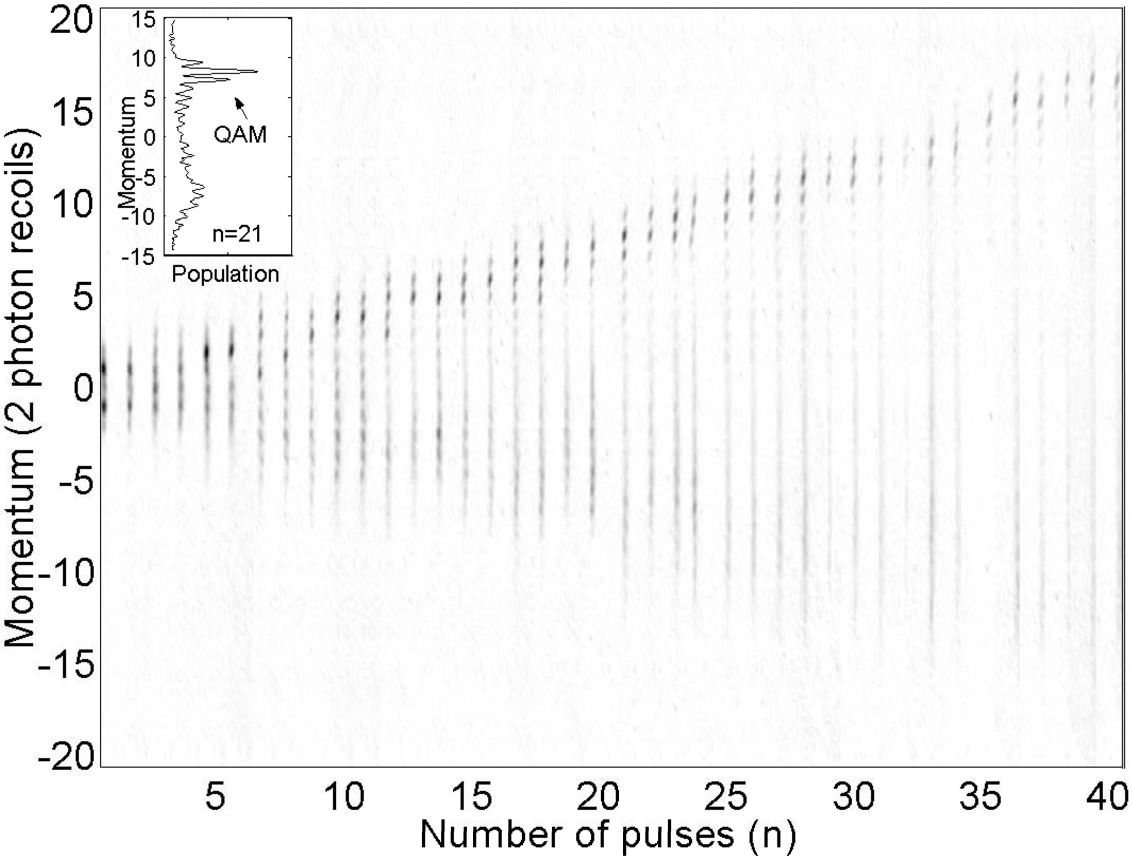

Figure 4.1. Experimental data showing the linear momentum gain of an accelerator mode with pulse number. The data shown was created by horizontally stacking 40 time of flight images of the condensate, each 8.9 ms after a certain number of kicks (horizontal axis) was applied to the BEC. The time interval between the kicks was 72 μs.

using a BEC over laser cooled atoms is that the BEC's initial state is confined inside a minimum-uncertainty box in the phase space. The very narrow momentum width of a BEC allows the observation of the discreteness of the momentum transferred to the atoms after each kick. These observations reveal that QAMs consist of a limited number of momentum states. Hence we are strongly motivated to revisit the interference model and generalize it to not only incorporate the higher order QAMs, but also to establish a better understanding of the relationship between the two theoretical pictures.

The format of this chapter is as follows. In Section 4.1 we briefly review both of the theories. In Sections 4.1.1 and 4.1.2 we discuss the classical and interference models originally presented in Ref. [73]. In Section 4.1.3 we review the ϵ-classical theory, and in 4.1.4 establish its relation to the interference model. This section ends with the generalization of the interference model to the higher order modes.

4.1 Theory

4.1.1 Classical Theory

To gain an understanding of the accelerator mode, we look first at the classical dynamics depicted in Fig. 4.2. Consider a particle moving in a vertical sinusoidal potential which is periodically switched on and off. In addition to the force of gravity, the particle will experience a force from the potential (and a consequent momentum change) if it is located in a region where the gradient of the potential is nonzero. We assume that the particle is initially placed at a position where it can experience a momentum change and that the particle does not move a significant distance within the potential during the time it is switched on. If the potential is given by $U = (U_{max}/2)[\cos(Gx)]$, where $2\pi/G$ is the spatial period, λ_G of the potential, the momentum change in a pulse is $\triangle p = -\overrightarrow{\nabla} U \triangle t$, where $\triangle t$ is the duration of the

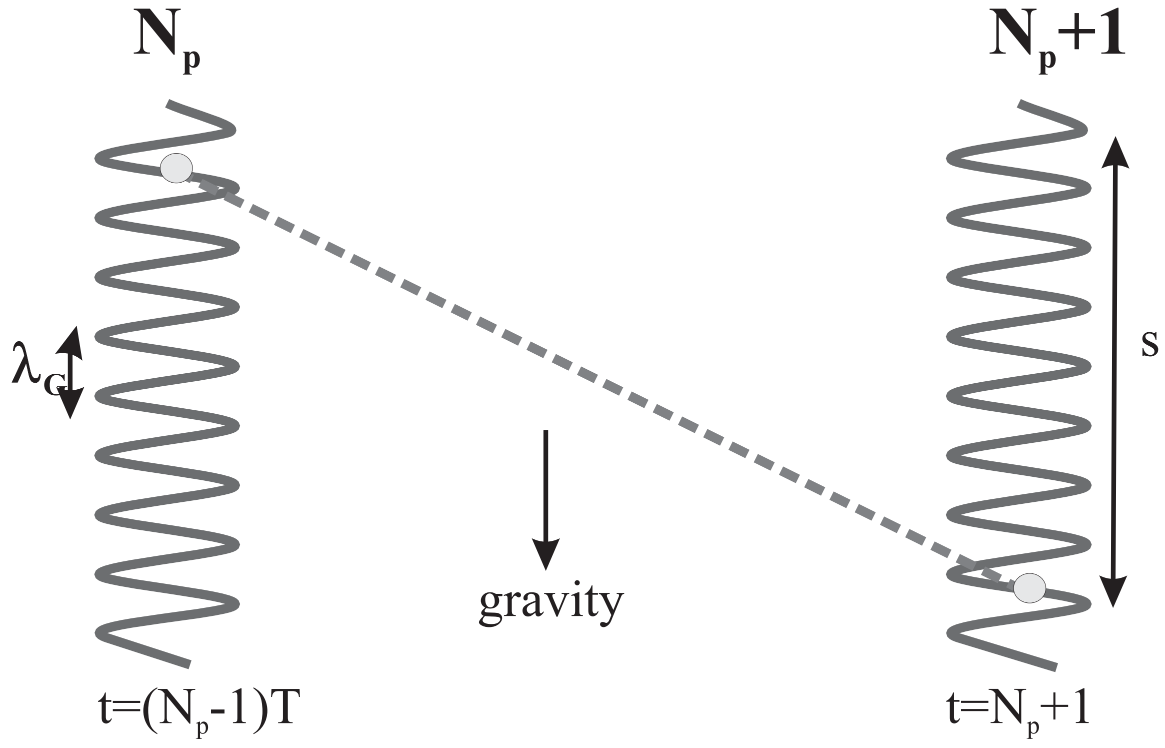

Figure 4.2. A schematic depicting the classical dynamics where time increases to the right. In order for a particle to remain in an accelerator mode, the distance which the accelerator moves between pulses, must be a whole multiple of the spatial period of the potential.

pulse. The velocity imparted by each pulse will then be

$$v_R = \frac{U_{max}}{2m} \sin\,(Gx) G \triangle t. \tag{4.1}$$

Only under the condition that the particle receives the same kick from every pulse will its momentum increase linearly with pulse number and remain in an accelerator mode. To find such a classical accelerator mode, we need to determine if there is a particular time interval between pulses, T, where the particle always returns to the same position within a period of the potential. In other words we need to find a value of T for which the distance the particle moves between successive pulses, s, is an integer number of spatial periods of the sinusoidal potential. This is equivalent to the condition

$$s = (N_p l' + l)\lambda_G, \tag{4.2}$$

where l and l' are integers and N_p is the number of the pulse. Note that the integer multiple of λ_G has been split into a factor dependent on pulse number and a separate factor, independent of pulse number. The distance, s, can be calculated from classical mechanics. At the time of the N_pth pulse $t = (N_p - 1)T$, so that the velocity gained due to the gravitational acceleration is $v_g = v_i + g(N_p + 1)T$. The velocity gained from the kicks of the potential is $v_k = N_p v_R$, where v_k is a recoil velocity. Thus between the N_pth and $(N_p + 1)$th pulse the particle moves a distance

$$s = (gT^2 + v_R T)N_p + (v_i T - \frac{1}{2} g T^2). \tag{4.3}$$

Equating this to Eq. 4.2, we find that for an accelerator mode,

$$\begin{aligned} gT^2 + v_R T &= l'\lambda_G & (4.4) \\ viT - \frac{1}{2} gT^2 &= l\lambda_G. & (4.5) \end{aligned}$$

Hence we can find the pulse separation times T for which a certain initial velocity class v_i is continually kicked into the same gradient of the potential. These particles will gain momentum linearly with pulse number and will be in a long-lived accelerator mode.

4.1.2 Interference model

The interference model for quantum accelerator modes is the quantum mechanical analog of the above idea. Cold atoms are used instead of classical particles and the sinusoidal potential can be created with a standing wave of off-resonant light. In this theory the laser cooled atoms' de Broglie wave packet is assumed to spread out over many periods of the standing wave. Through the light shift the standing wave potential can be written as,

$$H = \frac{\hat{p}^2}{2m} + mg\hat{z} - \frac{U_{max}}{2}[1+\cos(Gx)]\sum_{N_p}\delta(t-N_pT), \tag{4.6}$$

with $G = 2k$, the grating vector, and k the light wave vector. The Delta function in the third term indicates that the potential is on for a very short time such that atoms effectively do not move while the potential is on (Raman-Nath regime) with the net effect being to populate different momentum states according to the following relation (see figure 4.3),

$$|\psi\rangle = \sum_{n=-\infty}^{\infty} i^n J_n(\phi_d)|p_n\rangle, \tag{4.7}$$

where J_n is the nth order Bessel function of the first kind and $\phi_d = U_{max}\triangle t/(2\hbar)$, where $\triangle t$ is the duration of each, now finite pulse. Note that ϕ_d determines the relative populations in the diffraction orders after each pulse is applied. The phase accumulated in the momentum order $|p_q\rangle$, between the N_pth and (N_p+1)th pulse with respect to the phase in the state $|p_0\rangle$ is given by,

$$\phi_q - \phi_0 = \frac{\hbar G^2}{2m}Tq^2 + v_iGTq + gGT^2N_p\, q, \tag{4.8}$$

where v_i is the initial velocity of the atom, and q is the total number of grating recoils ($\hbar G$) that the atoms has gained up to and including the N_pth pulse, m is the atomic mass and T is the time between pulses. The first term in Eq. (4.8) is the phase evolution due to the extra momentum q. The second and third terms are the contributions of the initial velocity and the gravitational acceleration to the phase evolution. According to Eq. (4.8) the phase difference between two *adjacent* momentum states from one pulse to another is given by,

$$\phi_q - \phi_{q-1} = \frac{\hbar G^2}{2m} T(2q-1) + v_i G T + g G T^2 N_p. \tag{4.9}$$

We now impose the requirement that this phase difference be an integer multiple of 2π, a necessary constraint leading to constructive interference and the creation of a QAM. The above equation can be divided into two parts: one containing the terms q and N_p (which change with time) and another which is determined by the initial conditions. Thus,

$$\begin{aligned} \frac{\hbar G^2}{m} T q + g G T^2 N_p &= 2\pi q l && (4.10) \\ v_i G T - \frac{\hbar G^2}{2m} T &= 2\pi l', && (4.11) \end{aligned}$$

where l and l' are integers. These equations can be rearranged to find $p_i = m v_i$ (the initial momentum) and q (the momentum gained by the atoms participating in the accelerator modes),

$$\begin{aligned} p_i &= (\frac{l'}{\alpha} + \frac{1}{2}) \hbar G && (4.12) \\ q &= \frac{N_p}{\gamma} \frac{\alpha^2}{(l-\alpha)}, && (4.13) \end{aligned}$$

where $\gamma = \hbar^2 G^3 / 2\pi m^2 g$. The parameter α is defined as, $\alpha = T/T_{\frac{1}{2}}$ where $T_{\frac{1}{2}}$, the half Talbot time, is given by,

$$T_{\frac{1}{2}} = \frac{2\pi m}{\hbar G^2}. \tag{4.14}$$

It can also be seen from Eq. (4.9) that

$$\phi_{q+1} - \phi_q = \phi_q - \phi_{q-1} + 2\pi\alpha, \tag{4.15}$$

which implies that only a narrow range of diffraction orders around q can maintain the rephasing condition. This becomes even more critical as α increases.

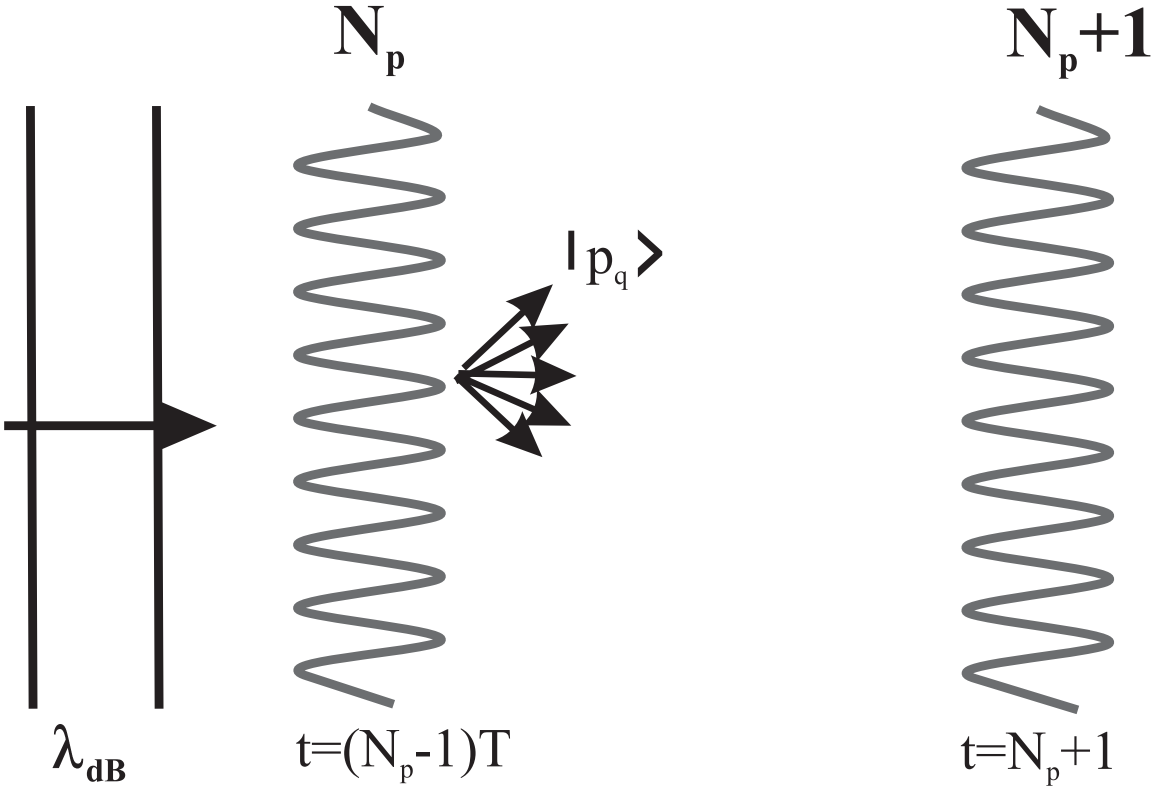

Figure 4.3. Schematic diagram showing the quantum mechanical picutre of the QAM process. Here the potential acts as a thin phase grating and diffracts the incident de Broglie wave. If the accelerator mode is to exist, several adjacent momentum states must rephase at the time of the following pulse.

4.1.3 ϵ-classical theory and higher-order modes

To study the ϵ-classical theory we start by writing the Hamiltonian of Eq. (4.6) in dimensionless units. We introduce the dimensionless variables,

$$\begin{aligned} x &= 2k_L z \\ p' &= \frac{p}{2\hbar k_L} \\ t' &= \frac{4k_L^2}{m} \\ H' &= \frac{m}{4(\hbar k_L)^2} H \end{aligned} \tag{4.16}$$

and set Planck's constant to one. The rescaled Hamiltonian will now take the following form (dropping the primes),

$$H = \frac{\hat{p}^2}{2} - \frac{\eta}{\tau}\hat{x} + k\cos(x)\sum_{N_p}\delta(t - N_p\tau), \tag{4.17}$$

where

$$k = \frac{V_0}{\hbar} \qquad\qquad \tau = \frac{4\hbar k_L^2 T}{m} \qquad\qquad \eta = \frac{mgT}{2k_L\hbar} \tag{4.18}$$

and the dynamics are now fully characterized by the dimensionless parameters k, τ , η. Note that the (1) in front of the cosine in Eq. (4.6) has also been dropped because it leads only to an uninteresting phase factor.

Due to of the appearance of gravity in the Hamiltonian of Eq. (4.17), there is no spatial symmetry and as such, the quasimomentum (the fractional part of the momentum) is not conserved. Thus, it would seem appropriate to measure the momentum in the free falling frame, namely to replace $\hat{p} - \frac{\eta}{\tau}\hat{t}$ by $\hat{p}$. This results in the spatial periodic Hamiltonian

$$H = \frac{(\hat{p} + \frac{\eta}{\tau}\hat{t})^2}{2} - \frac{\eta}{\tau}\hat{x} + k\cos(x)\sum_{N_p}\delta(t - N_p\tau), \tag{4.19}$$

Dynamics generated by this Hamiltonian conserve quasimomentum. Note that this Hamiltonian couples only momentum eigenstates whose momenta differ by an integer.

The study of the system described by Eq. (4.19) starts with decomposing the total momentum

$$p = \xi + \beta \tag{4.20}$$

where ξ and β are defined as the integer and the fractional (quasi-momentum) part of p respectively. With the above definition, the evolution is equivalent to that of a superposition of independent kicked rotors, each characterized by a different value of β. Such a rotor is called a β-rotor, and its one step evolution operator is

$$\hat{U}_\beta(t) = e^{-ik\cos(\hat{\theta})} e^{-i(\frac{\tau}{2})(\hat{N}+\beta+\eta t)^2} \tag{4.21}$$

where

$$\tau = x \bmod 2\pi \hat{N} = i\frac{d}{d\theta} \tag{4.22}$$

For $\beta = \eta = 0$ the result will be the usual kicked rotor. However, with gravity present ($\eta \neq 0$), the most surprising experimental result was that an appreciable fraction of atoms were found to accelerate (in the free falling frame). This acceleration was observed for various values of the experimental parameter, τ, around integer multiples of 2π. This is a quantum resonance effect that is more robust than the usual quantum resonances, and has no counterpart in the classical limit of Eq. (4.19). We now describe an explanation for this effect [76]. Assuming that the value of τ is close to a resonant value $2\pi l$, where l is a positive integer and the kicking strength is large compared to the kinetic and potential energy of the particle, we can write

$$\begin{aligned} \tau &= 2\pi l + \epsilon \\ k &= \frac{\tilde{k}}{\epsilon} \end{aligned} \tag{4.23}$$

with small ϵ. Using the identity, $e^{-iln^2} = e^{-il\pi n}$, the evolution operator, Eq. (4.21), takes the form

$$\hat{U}_\beta(t) = e^{-(i/|\epsilon|)\tilde{k}\cos(\hat{\theta})} e^{-(i/|\epsilon|)\hat{H}_\beta(\hat{I},t)} \tag{4.24}$$

where

$$\hat{I} = |\epsilon|\hat{N} = -i|\epsilon|\frac{d}{d\theta}$$

$$\begin{aligned} \hat{H}_\beta(\hat{I},t) &= \pm\frac{\hat{I}^2}{2} + \hat{I}[\pi l + \tau(\beta + t\eta) + \frac{\eta}{2}] \\ \pm &\equiv \frac{\epsilon}{|\epsilon|}. \end{aligned} \tag{4.25}$$

Treating $|\epsilon|$ as the pseudo-Planck's constant Eq. (4.24) appears as the the so-called ϵ-quantization of the following classical map

$$I_{t+1} = I_t + \tilde{k}\sin(\theta_t + 1), \qquad \theta_{t+1} = \theta_t \pm I_t + \pi l + \tau(\beta + t\eta + \eta/2) \tag{4.26}$$

Consequently, the small $|\epsilon|$ asymptotic of the quantum β rotor is equivalent to a quasiclassical approximation based on the evolution determined by the map of Eq. (4.26), called the ϵ-classical dynamics. We emphasize that the ϵ-classical limit $\epsilon \longrightarrow 0$ has nothing in common with the real classical limit $\hbar \longrightarrow 0$. Making the transformation

$$J_t = I_t \pm I_t + \pi l + \tau(\beta + t\eta + \eta/2) \tag{4.27}$$

we can remove the explicit time dependence to get

$$J_{t+1} = J_t + \tilde{k}\sin(\theta_{t+1}) + \tau\eta, \qquad \theta_t + 1 = \theta_t \pm J_t \, mod \, 2\pi \tag{4.28}$$

The map of Eq. (4.26) can have period-p fixed points. If these fixed points are stable they will be surrounded by islands of stability. If the atomic wave packet has a sizable overlap with one of these islands, its momentum will grow linearly with number of kicks according to,

$$q = q_0 - N_p\Big(\frac{\eta\tau}{\epsilon} + \frac{2\pi\mathfrak{j}}{\mathfrak{p}\epsilon}\Big) \tag{4.29}$$

These QAMs are classified according to their order $\mathfrak{p}$ and jumping index $\mathfrak{j}$. A fixed point $(\mathfrak{p}, \mathfrak{j})$ occurs at $J_0 = 2\pi\mathfrak{j}/\mathfrak{p}$ and $\theta_0 = \theta_i$. Figure 4.4 depicts phase space portraits of Eq. (5.1). A (1,0) stable fixed point occurs at $J_0 = 0$ in Fig. 4.4(a) where as, stable points with indexes (10,1) appear in Fig. 4.4(b). As can be seen, a stability island surrounds these stable fixed points, the first one giving rise to a primary QAM and the second giving rise to a higher order QAM.

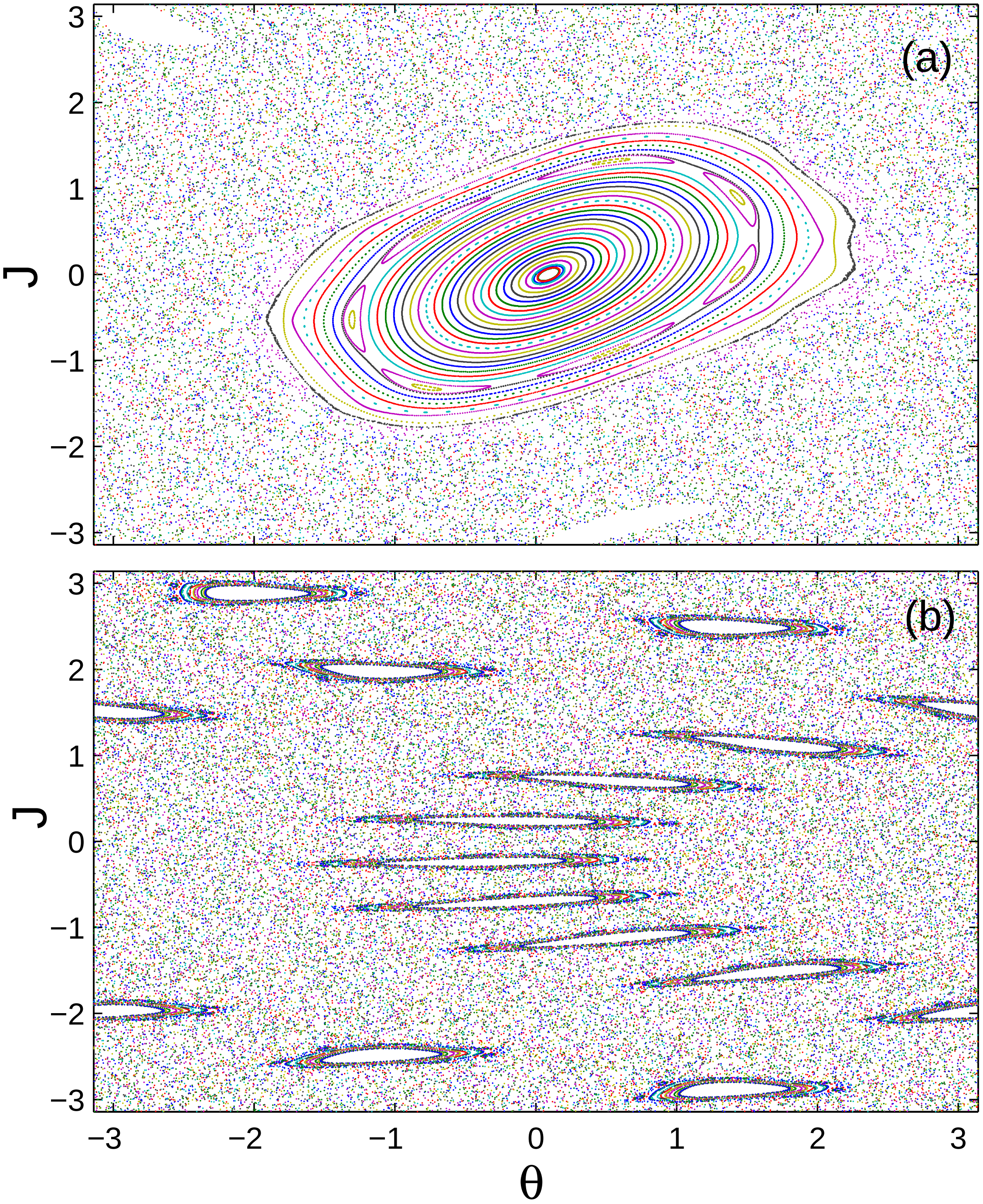

Figure 4.4. Phase space for the map of Eq. (4.28) with (a) $\phi_d = 1.4$ and $T = 29.5\mu$s. A stable fixed point with $(\mathfrak{p}, \mathfrak{j}) = (1, 0)$ exists at $J = 0$ and $\theta = 0.0887$. (b) $\phi_d = 1.4$ and $T = 66.3\mu$s. A stable fixed point with $(\mathfrak{p}, \mathfrak{j}) = (10, 1)$ exists in the cell which gives rise to a higher order QAM.

4.1.4 Generalized interference model

In this section we demonstrate that the stability of a fixed point in the ϵ-classical theory is equivalent to the constructive interference condition between two neighboring diffraction states in the interference model. We start with Eq. (5.2) and rewrite it in the following form,

$$\frac{J_{N_p}}{|\epsilon|} = \epsilon P + \pi\ell + \tau(\beta + N_p\eta + \eta/2) \tag{4.30}$$

Where P is the integer part of the momentum in units of $\hbar G$ after the N_pth pulse is applied.

As mentioned earlier the $\mathfrak{j}$=0 stable fixed point of this map is at $J = 0$ and does not change after applying any number of kicks. By definition, P in Eq. (4.30) is the total momentum acquired by the fixed point from the pulses. This is equivalent to the definition of q in the interference model allowing us to replace P with q in the following discussion. Also, since β is conserved, its value is determined by the initial velocity via $\beta = mv_i/\hbar G$. Substituting these results and definitions of τ, η and $\epsilon = \hbar G^2 T/m - 2\pi l$ into Eq. (4.30) we have,

$$\frac{\hbar G^2}{2m}T2q - 2\pi ql + \pi l + (TGv_i + gGT^2N_p + \frac{1}{2}GgT^2) = 0, \tag{4.31}$$

Working in the free falling frame introduces the last term into the equation. In the lab frame Eq. (4.31) reduces to Eq. (4.9) up to a constant phase factor of $\pi l - \hbar G^2 T/2m$. In other words the existence of a stable fixed point in the ϵ-classical theory produces the same equation for the formation of a QAM as the interference theory. We now use this insight to see how the interference model needs to be modified in order to explain higher order QAMs. A $(\mathfrak{p}, \mathfrak{j})$ fixed point appears at $J_0 = 2\pi\mathfrak{j}/\mathfrak{p}$ and gains $2\pi\mathfrak{j}/\mathfrak{p}$ momentum units for each iteration, so at the N_pth pulse the total momentum of the fixed point in Eq. (4.31) becomes $(2\pi\mathfrak{j}/\mathfrak{p})N_p$. Splitting this equation in a similar manner to Eq. (4.10) of the interference model we have,

$$\frac{\hbar G^2}{2m}T2q + gGT^2N_p = 2\pi ql + \frac{2\pi\mathfrak{j}}{\mathfrak{p}}N_p \tag{4.32}$$

This gives the same expression for the total momentum gained by a QAM after the N_pth kick as Eq. (4.29), which was derived for the ϵ-classical model. Therefore for a QAM with indexes $(\mathfrak{p},\mathfrak{j})$ the phase difference between two neighboring momentum states can only be an integer multiple of 2π when $\frac{\mathfrak{j}}{\mathfrak{p}}N_p$ is an integer. Hence N_p must be an integer multiple of $\mathfrak{p}$. This concept can be generalized even further to explain the QAMs at higher order quantum resonances where $\tau = 2\pi(a/b)$ with a and b positive integer numbers. For QAMs at these resonant times the rephasing happens between momentum diffraction orders that are separated by $b\hbar G$. Hence rewriting Eq. (4.9) for the momentum states of q and $q-b$ we have,

$$\phi_q - \phi_{q-b} = \frac{\hbar G^2}{2m}T(2qb + b^2) + v_i GTb + gGT^2N_pb. \tag{4.33}$$

Once again separating Eq. (4.33) into two time dependent and independent parts, the momentum gain of a QAM and the initial condition required for a QAM to exist at higher order resonances are given by the following,

$$\begin{aligned} q &= \frac{N_p}{\gamma}\frac{a^2b}{l' - ab} && (4.34)\\ p_i &= (\frac{l}{ab} - \frac{1}{2b})\hbar G && (4.35)\end{aligned}$$

To summarize, we have generalized the interference model to explain the higher order QAMs. We have shown that the higher order accelerator modes are generated by the rephasing of neighboring diffraction momentum states after multiple pulses. Furthermore, the model was extended to the QAMs at higher order quantum resonances by showing that they are generated by rephasing between momentum states with certain separations set by the quantum resonance time. The relation between this model and the pseudo-classical model was established. This was accomplished by showing that the constructive interference between momentum states populated by the pulsed light determines the stability island's existence in the pseudo-classical phase space.

CHAPTER 5

EXPLORING THE PHASE SPACE OF THE QUANTUM DELTA KICKED ACCELERATOR

5.1 Introduction

For more than a century the study of chaotic phenomena has been recognized as being crucial in the development of a fuller understanding of nature. In the previous chapter we reviewed the main theoretical models investigating the QAMs, a much celebrated and studied system in the field of chaos. In this chapter we present our experimental observations of the QAMs and show how the theoretical model we expanded upon agrees with our experiment.

An important aspect in studies involving quantum chaos which was missing until relatively recently was experimental scrutiny of quantum systems which in the classical limit exhibit chaotic behavior. The field was given a boost and gained much momentum since laser cooling techniques gave scientists a valuable tool to lower the temperature of atoms to new limits. Once a system was set up to achieve a cold atomic cloud, the next step was to find a way of applying a periodic force on the cold atoms. In short, what was needed was the equivalent of the classical kicked rotor in quantum mechanics. The fact that light could exert force on atoms was a well known scientific fact by the time the Oxford group [70] first observed quantum accelerator modes in 1999. There, they subjected ultra cold cesium atoms to a pulsed standing wave of off-resonant light.

It should be noted here that in the theoretical description of the QDKR the effective value of Planck's constant scales with the time between the pulses [140,141]. Therefore, to investigate classical correspondence in which $\hbar \rightarrow 0$, the time between pulses needs to be close to zero. However, for technical reasons this value can not be made arbitrarily small in experiments.

Perhaps the simplest way of experimentally realizing the QDKA is by applying the pulsed standing wave in the direction of gravity [70,73]. This experiment has led to the discovery of quantum accelerator modes (QAMs) near the resonance times. As we mentioned in the previous chapter, one of the most important characteristics of QAMs is that they are comprised of atoms which show a linear momentum growth with pulse number in a freely falling frame [70]. It has been shown that the QAMs are quantum nondissipative counterparts of mode locking [142]. They have also been suggested for use in the preparation of well defined initial conditions for quantum chaos experiments [143]. FGR attributed the QAMs to the existence of stability islands in the pseudo-classical phase space. These studies have shown that this underlying phase space has a complex structure which is highly sensitive to the experimental parameters. However, the broad momentum distribution of the laser cooled atoms which have been used so far to study this system have prevented the examination of the local structures in the phase space.

In this chapter we report our results on the realization of QAMs using a Bose-Einstein condensate (BEC) of Rubidium 87 atoms and the exploration of the pseudo-classical phase space structure of the QDKA. Figure 5.1 shows experimentally observed momentum distributions as a function of the number of standing wave pulses applied to a BEC. This figure demonstrates that the QAM gains momentum linearly as the number of pulse increases. This is the first time that it has been possible to determine that the QAM is made up of several distinct momentum states as originally postulated in Ref. [73]. This quantization of momentum is observable because the initial momentum uncertainty of the condensate was much smaller than two photon recoils.

According to the ϵ-classical model (see previous chapter), for pulse periods close to integer multiples of the half Talbot time, $T_\ell = \ell \times 2\pi m/\hbar G^2 (= \ell \times 33.3\mu s$ for Rb87

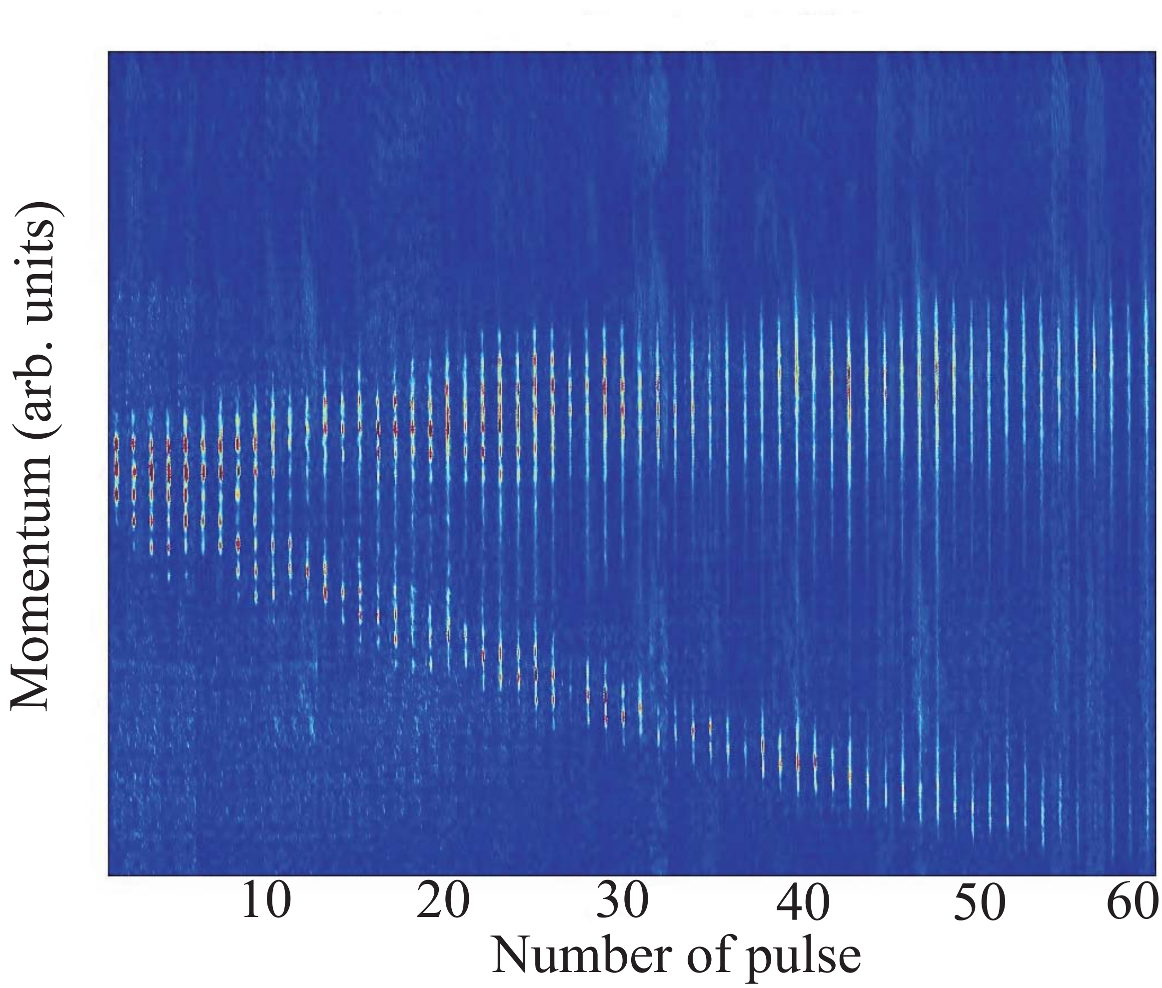

Figure 5.1. Experimental momentum distributions showing a QAM in a BEC exposed to a series of kicks from a standing light wave in the free falling frame. The kicking period was 61 μs and $phi_d \approx 3$. The momentum distributions are displaced as a function of the number of kicks. The accelerator mode is the collection of momentum states that appear to move towards the lower right.

atoms) the system can be described by the classical map [76],

$$\begin{aligned} \theta_{n+1} &= \theta_n + \mathrm{sgn}(\epsilon) J_n \\ J_{n+1} &= J_n - K\sin(\theta_{n+1}) + \mathrm{sgn}(\epsilon)\tau\eta, \end{aligned} \tag{5.1}$$

where $\epsilon = 2\pi\ell(T/T_\ell - 1)$ is a small number, ℓ is any positive integer number, and $K = |\epsilon|\phi_d$. The dimensionless J and θ parameters are defined as,

$$\begin{aligned} \theta &= G\,x \bmod(2\pi) \\ J_n &= I_n + \mathrm{sgn}(\epsilon)[\pi\ell + \tau(\beta + n\eta + \eta/2)] \end{aligned} \tag{5.2}$$

where $p/(\hbar G) = I/|\epsilon| + \beta$, β is the fractional momentum, $\tau = \hbar T G^2/m$, and $\eta = mg'T/(\hbar G)$. Figure 5.2 shows a typical phase space portrait for the map of Eq. (5.1) with $\phi_d = 1.4$, $T = 29.5\mu$s and $\epsilon = -0.72$. Perhaps the most important feature of this plot is the existence of a stable fixed point surrounded by an island of stability. If the size of these islands is large enough to capture a significant fraction of the wavepacket they give rise to observable accelerator modes. According to this model the momentum gain of an atom in a period $\mathfrak{p}$ accelerator mode after n kicks is given by,

$$q = n\Big[\frac{\eta\tau}{\epsilon} + \frac{2\pi\mathfrak{m}}{\mathfrak{p}|\epsilon|}\Big], \tag{5.3}$$

where $\mathfrak{m}$ is an integer and $(\mathfrak{p}, \mathfrak{m})$ specifies a particular accelerator mode [72,76,142].

For an atom to appear in an accelerator mode, the initial conditions are a crucial factor to be considered. The limited range of conditions that can produce a QAM is a consequence of the fact that the stability islands do not cover the whole unit cell of the phase space. Furthermore, the initial momentum required for an accelerator mode to emerge is periodic. This can be seen by using Eq. (5.2) and the fact that J has a periodicity of 2π. This is equivalent to a momentum periodicity of $\Delta p = 2\pi\hbar G/\tau$. Observing this phase space structure requires that the atomic momentum distribution be narrower than $2\pi\hbar G/\tau$. This implies a temperature of ≈ 450 nK for Rb87 atoms exposed to a pulsed standing wave of 390 nm wavelength

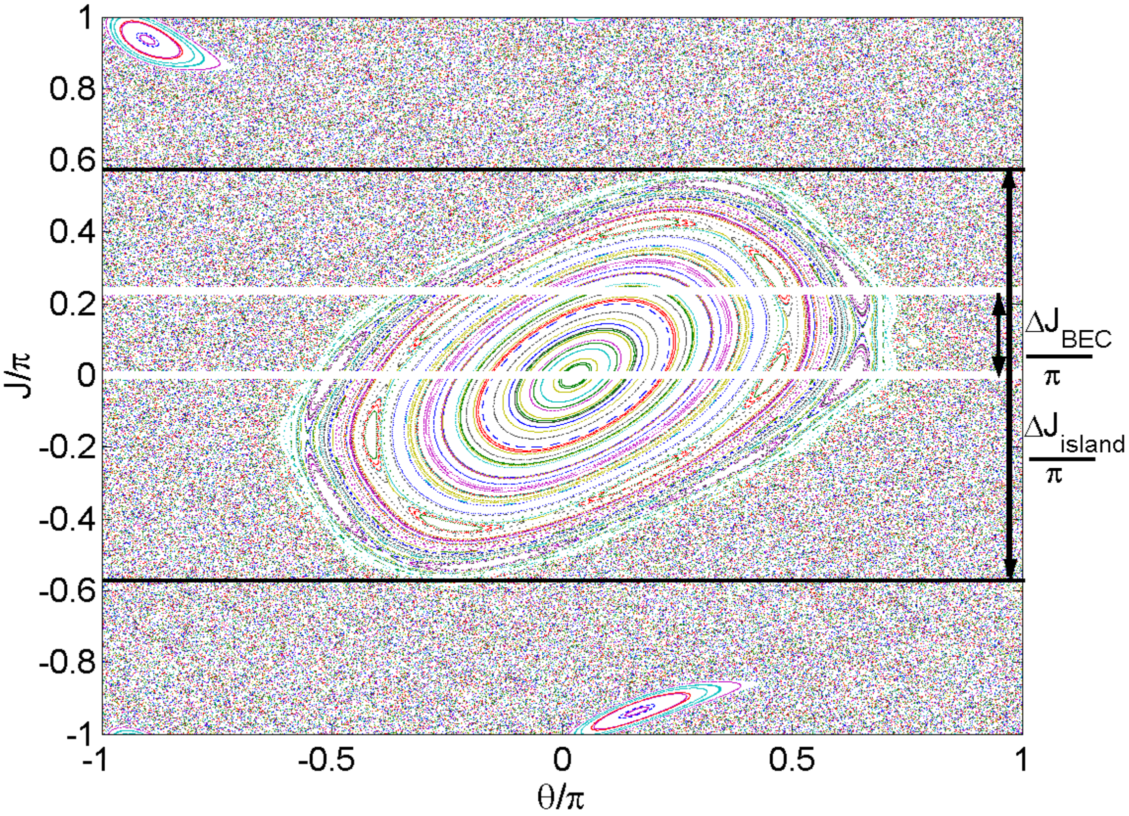

Figure 5.2. Phase space unit cell for the QDKA map of Eq. (5.1) with $\phi_d = 1.4$ and $T = 29.5$ μs. A stable fixed point with $(\mathfrak{p}, \mathfrak{m}) = (1, 0)$ exists at $J = 0$ and $\theta = 0.0887$. This stable fixed point is surrounded by the stability island in which the quantum accelerator mode will be created if the atomic initial conditions are inside the island. The momentum width of the condensate, ΔJ_{BEC} and the stability island ΔJ_{island}, are shown with the solid white and black lines respectively.

and pulse period close to the Talbot time ($\ell = 2$). To this extent, a BEC is an ideal candidate [144]. The momentum width of our condensate is shown with two white lines in Fig. 5.2. Note that this width is smaller than the momentum extent of the island, indicating that the momentum resolution of the experiment is more than sufficient to clearly detect and identify a stability island from the chaotic background. However, for experiments utilizing cold thermal atomic samples, the momentum distribution is significantly wider than $\hbar G$. Although this wide momentum distribution makes it relatively easy to observe the accelerator modes, there is no direct way of examining the structure of the phase space.

In order to explore the phase space of the kicked accelerator using BEC, the experimental setup described in detail in Chapter 3 was used. Briefly speaking a pure condensate with $\sim$ 50000 atoms in the $5S_{1/2}F = 1, m_F = 0$ state was created in an optical trap of a CO_2 laser. The CO_2 laser was then turned off and after a variable time interval the kicking potential was turned on. Varying this time allowed the BEC to fall under the influence of gravity, thus changing the momentum of the condensate at the commencement of the kicks. The kicking beam size was 1 mm, large enough to ensure that ϕ_d did not change appreciably while the BEC was interacting with the series of kicks. The phase modulation depth, ϕ_d, was inferred by noting the population of the first and zeroth order momentum states after one pulse and comparing the results to Eq. 4.7. The temporal profile of the standing wave light was controlled by periodically switching the AOM on in order to create a sequence of pulses each 250ns in length. The momentum distribution was measured using a time of flight method. Meaning the condensate expanded for a controlled time interval, typically 9 ms, and was then destructively imaged using an absorptive technique.

To observe the pseudo-classical phase space structure of the QAMs, a series of data were taken for pulse periods near both half-Talbot and Talbot times. Figure 5.3 shows a typical data set taken at (a) $T = 61\mu$s and (b) $T = 72.2\mu$s pulse separations for different values of the BEC's initial momentum. These times occur on either side

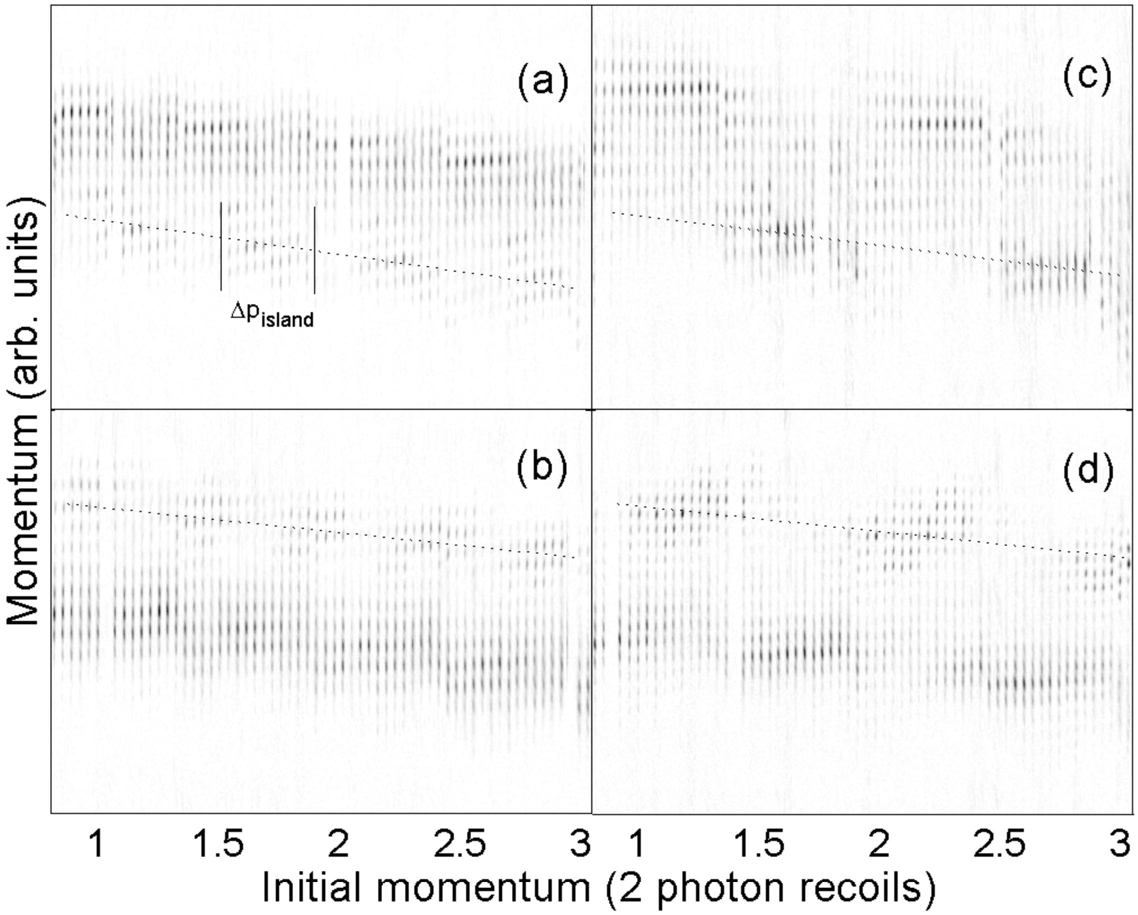

Figure 5.3. Experimental momentum distributions showing the sensitivity of the QAMs to the initial conditions. The data was taken after applying 10 kicks with time intervals of (a) 61 μs (b) 72.2 μs and 30 kicks with time intervals of (c) 28.5 μs, and (d) 37.1 μs between the pulses. The initial velocity was changed by applying the kicking potential with variable time delays after releasing the condensate from the CO_2 laser. The slope of the data seen in this figure is caused by the momentum gain due to gravity. The doted lines denote the position of the QAM. Note that Δp_{island} is related to the size of the stability islands by $\Delta p_{island} = \hbar G \Delta J_{island}/\tau$

of the Talbot time at $T = 66.6\mu$s. The data in Fig. 5.3 was created by horizontally stacking 60 time-of-flight images of the condensate, each for a different initial momentum. These data confirm the periodicity of the QAMs with momentum. Furthermore, the data of Fig. 5.3 provides a direct way to validate the theoretical prediction of the island size. To do so, the data of Fig. 5.3 was summed along the initial momentum axis. Δp_{island} was then determined by measuring when the height of the QAM had dropped to 1/e of its maximum value. The experimental and theoretical values for the momentum extent of the islands are given in Fig. 5.4, near (a) half-Talbot and (b) Talbot times. The theoretical values were inferred by plotting the map of Eq. (5.1) for the corresponding experimental values of K. The circle and asterisk signs are the experimental and theoretical values for ΔJ_{island} (as defined in Figs. 5.2 and 5.3). It can be seen that the experimental values are very close to the theoretical predictions. Note that for values of $K > 2$ at half-Talbot time, the stability island elongates in J and becomes narrow in θ. This behavior reduces the effective overlap between the BEC's wavefunction and the stability island and consequently the QAMs were not visible in Fig. 5.4(b) for higher values of K.

Figure 5.3 also shows that there can be little overlap between the initial conditions that will populate a QAM at two different values of T. This behavior particularly affects what happens in experiments in which the momentum distribution is measured as the pulse period is scanned across a resonance time. Unlike the experiments with cold atomic samples where the QAMs on both sides of a resonance could be populated [70], in the case of the condensate, only the QAMs which have significant overlap with the condensate wavefunction will be observable. This can be seen in Fig. 5.5, where we performed a scan of pulse period across the Talbot time for two different initial momenta. The initial momentum for Fig. 5.5(a) was set to $1.2\hbar G$ such that the QAMs were efficiently loaded at pulse periods near $T = 72\mu$s, whereas in Fig. 5.5(b), the initial momentum was set at $1.5\hbar G$ to mainly populate the QAMs around pulse periods near $T = 61\mu$s. QAMs with indices $(\mathfrak{p}, \mathfrak{m})$ =(1,0) appear at

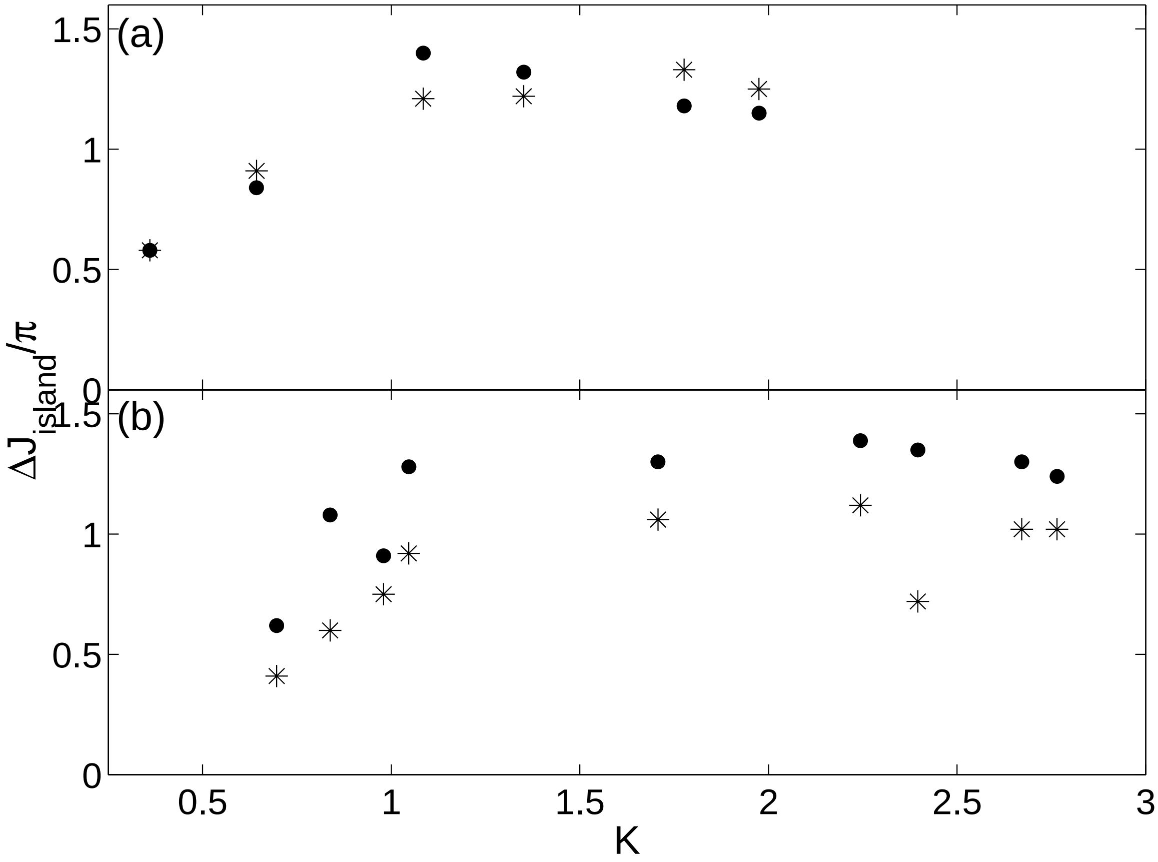

Figure 5.4. Experimental data showing the momentum range in which the QAMs appear and the corresponding theoretical predictions. (a) shows the experimental (circle) and theoretical (asterisk) values for $\Delta J_{\mathrm{i}sland}$ near half-Talbot time and (b) show the same quantities near Talbot time. Figure 5.3 illustrates the method used to experimentally infer $\Delta J_{\mathrm{i}sland}$.

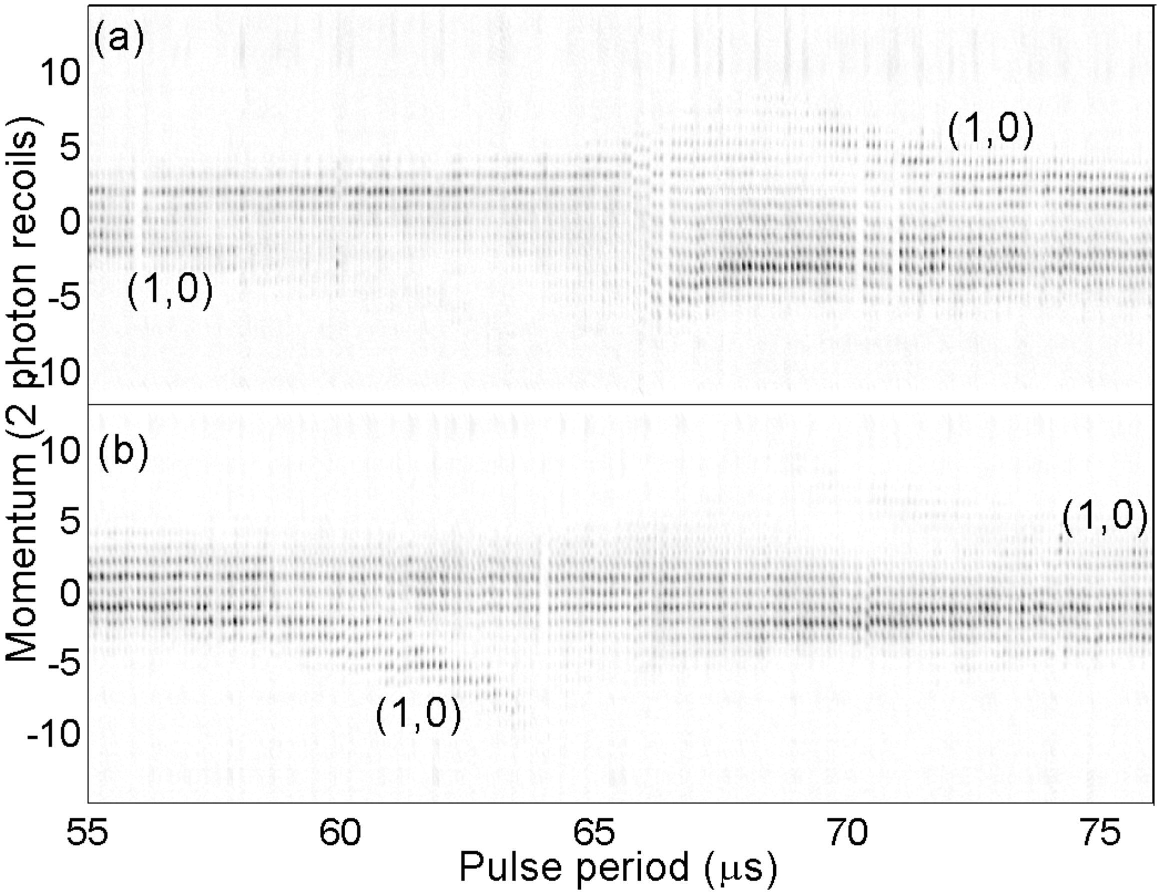

Figure 5.5. Experimental momentum distributions showing controllable loading of the $(\mathfrak{p}, \mathfrak{m})$ =(1,0) QAMs. The data was taken by applying 10 kicks for a range of kicking pulse periods. In (a) the initial momentum was set to $1.2\hbar G$ so as efficiently create QAM at pulse periods greater than the Talbot time while in (b) the initial condition was set to $1.5\hbar G$ to efficiently create QAM at pulse periods smaller than the Talbot time.

pulse periods greater than the Talbot time in Fig. 5.5(a), whereas in Fig. 5.5(b) the (1,0) QAM mostly appears at pulse periods smaller than the Talbot time. Note that this is the first time that it has been possible to selectively populate an island at a particular position in phase space.

5.2 Experimental observation of higher order QAMs

As mentioned earlier the main advantage of using a BEC to realize the QDKA is the improved momentum resolution which allows the observation of the individual momentum states produced by the pulses of the standing wave. Therefore such experiments provide a direct method to examine the validity of the interference model. Figure 5.1 shows the observed QAMs near Talbot time where the time interval between the kicks was 61 μs. This figure shows that mainly three neighboring momentum states comprise the QAM and almost maintain their population while gaining momentum from the kicks. According to the interference model, these are the momentum states that can rephase at the next kick with a higher momentum. This argument becomes stronger at pulse separations near the quarter-Talbot time where $b = 2$, and hence according to the interference model the rephasing happens between momentum states separated $b\hbar G = 2\hbar G$. Hence the momentum states with $2\hbar G$ separations should be populated in the QAM. Recently we have been able to observe QAMs near the quarter-Talbot time. Figure 5.6 shows an example of such data in which the QAM appeared when the time interval between the kicks was 15.8 μs. The dotted lines in this figure indicate that rephasing happens between states with $2\hbar G$ separations, in good agrement with the prediction of the model. Another aspect of the theory is given by Eq.(4.35) which indicates a ladder structure for the initial momentum required for observing QAMs. Although existence of this structure has been observed with cold atoms [71] and BEC, [138] it has been confined to kicking separations close to Talbot and half-Talbot time. According to Eq. 4.35 this periodicity

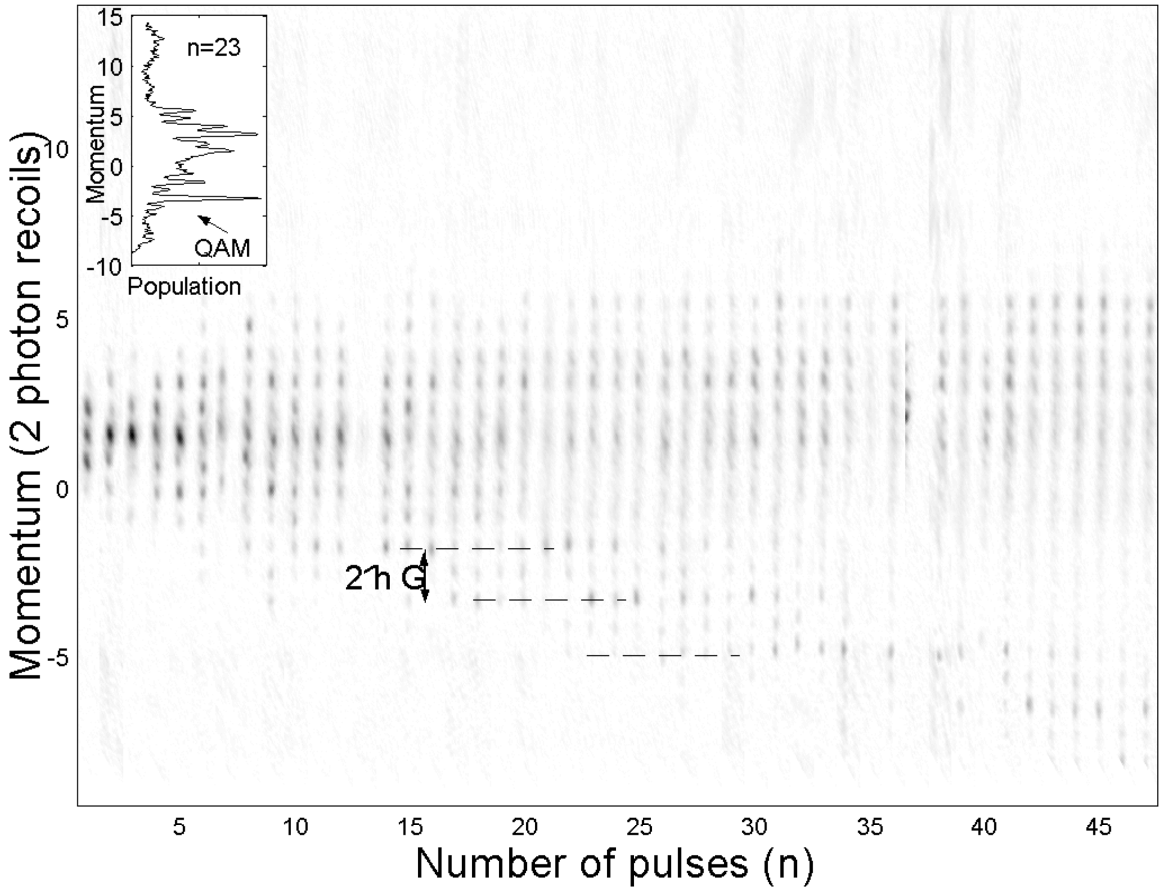

Figure 5.6. Experimental data showing the quantum accelerator modes near quarter-Talbot time where the time interval between the kicks was 15.8 μs. The data shown was created by horizontally stacking 47 time of flight images of the condensate, each 8.9 ms after a certain number of kicks (horizontal axis) applied to the BEC. Note the jumping of the diffraction orders by 2 as the kicks increase

TABLE 5.1. Parameters for the interference model for different kicking time intervals. The predicted and observed periodicity of the QAMs with initial momentum are given in last two columns.

Kicking period	$\alpha \approx$	a/b	b	Δp_i theory	Δp_i observed
Talbot	2	2	1	$\frac{\hbar G}{2}$	$\frac{\hbar G}{2}$
Half-Talbot	1	1	1	$\hbar G$	$\hbar G$
Quarter-Talbot	$\frac{1}{2}$	$\frac{1}{2}$	2	$\hbar G$	$\hbar G$

in the initial momentum depends on the kicking period as $\Delta p_i = \hbar G/ab$. To observe this periodicity a series of data were taken at Talbot, half-Talbot and quarter Talbot times with a constant number of kicks but variable initial momentum. The initial momentum of the condensate was changed by turning off the CO_2 laser and applying the kicking potential after a variable time interval during which the BEC gained momentum under the influence of gravity. Figure 5.7 shows three data sets taken at (a) $T = 15.8\mu s$ (b) $T = 37.1\mu s$ and (c) $T = 61\mu s$ pulse separations for different values of the BEC's initial momentum. The data in Fig. 5.7 was created by horizontally stacking 60 time-of-flight images of the condensate, each for a different initial momentum. The theoretical predictions and the observed periodicity of the momentum deduced from Fig. 5.7 are summarized in Table 5.1 which indicates good agreement between the predictions of the model and experiments. The periodicity of the QAMs was deduced from the separation between the QAMs as shown in Fig. 5.7.

In conclusion our experiments have demonstrated the feasibility of observing quantum accelerator modes using a BEC. We were able to examine the underlying pseudo-classical phase space structure of the quantum delta kicked accelerator. Quantum accelerator modes near quarter-Talbot time were also observed for the first time. These observations allowed us to validate the interference model and its predictions for the periodicity of the QAMs with the initial momentum of the BEC at Talbot,

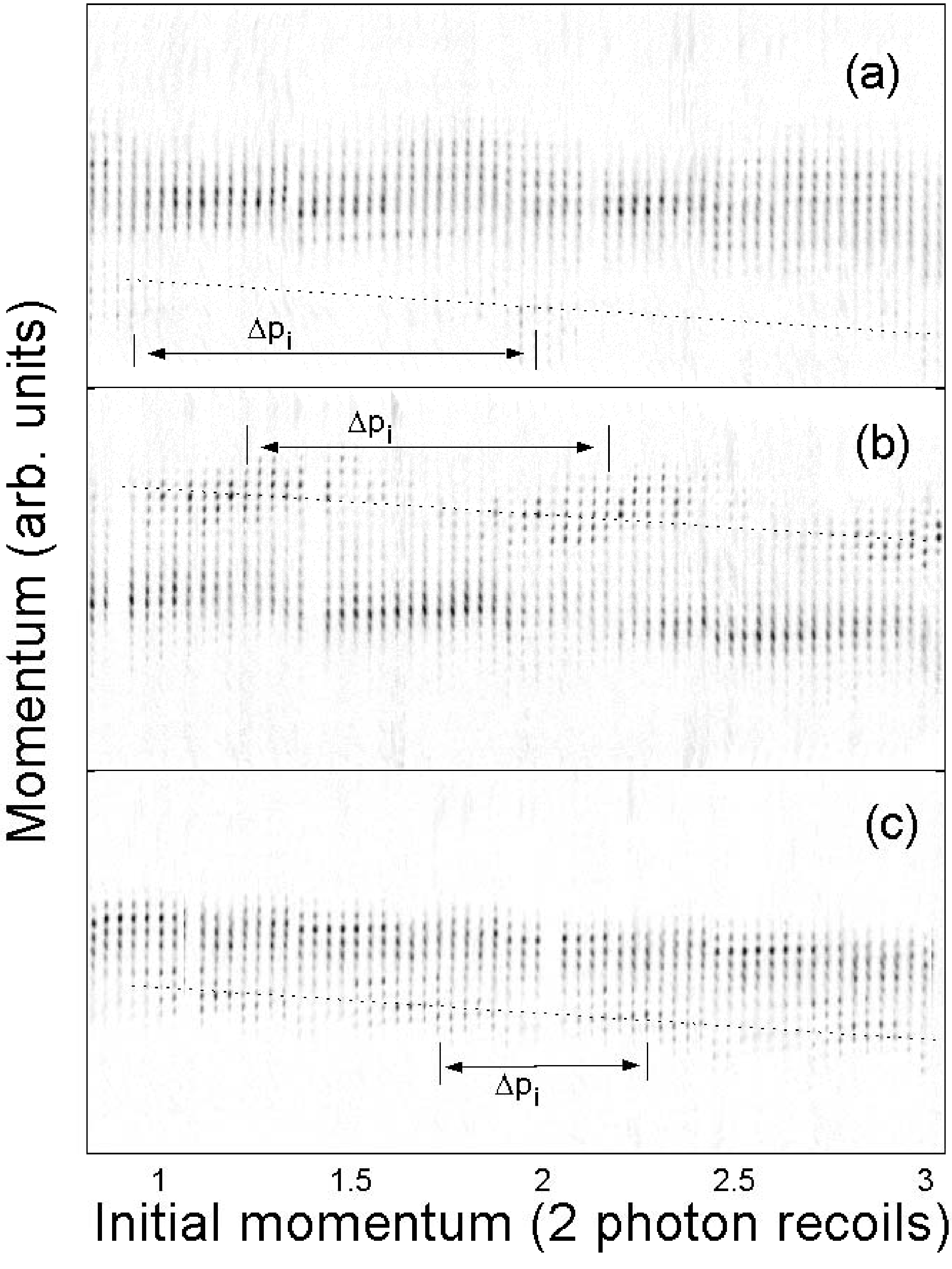

Figure 5.7. Experimental data showing the periodicity of quantum accelerator modes with initial momentum. The data is taken after applying 50 kicks with a pulse interval of (a) 15.8μs, (b) 30 kicks with 37.1μs and (c) 10 kicks with 61μs which are close to near quarter-Talbot, half-Talbot and Talbot time.The larger number of kicks at the half-Talbot and Talbot time was necessary due to the smaller momentum transfer per pulse. QAMs are the group of atoms propagating towards the lower right of the figure and the dashed lines are drawn to guide the eye

half-Talbot and quarter-Talbot time. These experiments pave the way towards further investigation of more complex systems like the kicked harmonic oscillator [145,146] and dynamical tunneling [147,148] that have received little study. This experiment also opens the door to experimental observation of many phenomena related to quantum chaos. For example, the high momentum resolution of the experiment could bring the possibility of observing bifurcation of the stability islands to a practical level. This should lead to a better understanding of the transition to chaos in a quantum system.

CHAPTER 6

CONCLUSION AND OUTLOOK

In this thesis, the results for the first observation of quantum accelerator modes using a Bose-Einstein condensate has been presented. To facilitate the stable creation of BEC we changed the optical trap geometry from a two crossed optical beam configuration to a single beam configuration. By varying the beam size from wide to tight, the optical dipole traps' loading and evaporative cooling efficiencies were improved respectively. This was accomplished by passing the laser beam creating the optical trap through an expanding telescope with one of the lenses mounted on a translation stage before it enters the vacuum chamber.

To realize the quantum delta kicked rotor, spatially corrugated off resonance pulses were used as the kicking potential to import momentum to the condensate. This system also allowed us to experimentally observe the quantum accelerator modes for the first time. We also confirmed the existence of stability islands in the phase space of the quantum delta kicked rotor

We further studied the creation mechanism of the QAMs with an interference model. We showed that the coordinates of stable fixed points on the phase space portrait of the semi-classical treatment of the QDKR is equivalent to the constructive interference condition between the neighboring momentum states populated by diffraction of the BEC off the kicking pulses. By establishing this relation between the two models we were able to generalize the interference model to predict the nature of the QAMs at higher order quantum resonances. These theoretical predictions were validated with observation of the higher order QAMs reported in Chapter 5 of this thesis.

6.1 Future Directions

The experimental and theoretical tools developed in this thesis allows the next generation of experiments to advance the study of the quantum delta kicked rotor. For example, one can study the effect of the mean-field energy of the BEC in the stability of the QAMs. The mean-field energy can be manipulated using Feshbach resonance.

The quantum kicked harmonic oscillator (QDKHO) which has been studied only theoretically is another system that can be realized with the setup developed in this thesis by kicking the BEC with the optical trap on. For certain experimental parameters the phase space of the QDKHO has a stochastic web structure that spreads all over the phase space. A point on this web can be accelerated infinitely along the the channels of the web even for an infinitesimal value of the kicking strength. Studying such systems will help us to investigate the foundations of quantum chaos.

BIBLIOGRAPHY

1. Jürgen Moser,"Is the Solar Stable?" Neue Zurcher Zeitung, (1975).

2. Jürgen Moser, Stable and Random Motions in Dynamical Systems (Princeton University Press, Princeton, 1973).

3. Jürgen Moser,"Is the Solar System Stable?" Math. Intell. **1**, 65 (1978).

4. Michael Tabor, Chaos and Integrability in Nonlinear Dynamics: An Introduction (Wiley, New York, 1989).

5. Leon Glass, Alvin Shrier, and Jacques Bélair, "Chaotic cardiac rhythms," in Chaos, Arun V. Holden, Ed. (Princeton University Press, Princeton, 1986).

6. Reuben H. Simoyi, Alan Wolf, and Harry L. Swinney, "One-Dimensional Dynamics in a Multicomponent Chemical Reaction," Phys. Rev. Lett. **49**, 245 (1982).

7. W.M. Schaffer and M. Kot, "Differential systems in ecology and epidemiology," in Chaos, Arun V. Holden, Ed. (Princeton University Press, Princeton, 1986).

8. Tien-Yien Li and James A. Yorke, "Period Three Implies Chaos," Am. Math. Monthly **82**, 985 (1975).

9. Boris V. Chirikov, "Time-Dependent Quantum Systems," in Chaos and Quantum Physics: Proceedings of the Les Houches Summer School, Session LII, 1-31 August 1989,M.-J. Giannoni, A. Voros, and J. Zinn-Justin, Eds. (North-Holland, Amsterdam, 1991).

10. Robert C. Hilborn, Chaos and Nonlinear Dynamics: An Introduction for Scientists and Engineers (Oxford University Press, Oxford, 1994).

11. Robert L. Devaney, An Introduction to Chaotic Dynamical Systems, second ed. (Addison-Wesley, Reading, 1989).

12. George Sugihara and Robert M. May, "Nonlinear forecasting as a way of distinguishing chaos from measurement error in time series," Nature **344**, 734 (1990).

13. A.A. Tsonis and J.B. Elsner, "Nonlinear prediction as a way of distinguishing chaos from random fractal sequences," Nature **358**, 217 (1992).

14. Fritz Haake, Quantum Signatures of Chaos, second ed. (Springer-Verlag, Berlin, 2001).

15. S.A. Gardiner, J.I. Cirac, and P. Zoller, "Quantum Chaos in an Ion Trap: The Delta-Kicked Harmonic Oscillator," Phys. Rev. Lett. **79**,4790 (1997).

16. S.A. Gardiner, Quantum Measurement, Quantum Chaos, and BoseEinstein Condensates, Doctoral dissertation, LeopoldFranzensUniversitat Innsbruck (2000).

17. Rüdiger Schack and Carlton M. Caves, "Hypersensitivity to Perturbations in the Quantum Bakers Map," Phys. Rev. Lett. **71**, 525 (1993).

18. Rüdiger Schack, Giacomo M. DAriano, and Carlton M. Caves,"Hypersensitivity to Perturbations in the quantum kicked top," Phys. Rev. E **50**, 972 (1994).

19. B.V. Chirikov, F.M. Izrailev, and D.L. Shepelyansky ,"Dynamical Stochasticity in Classical and Quantum Mechanics," Sov. Sci. Rev. C **2**, 209 (1987).

20. M. Toda and K. Ikeda, "Quantal Lyapunov Exponent," Phys. Lett. A **124**, 165 (1987).

21. Ronald F. Fox and T.C. Elston, "Chaos and the quantum-classical correspondence in the kicked pendulum," Phys. Rev. E **49**, 3683 (1994).

22. Boon Leong Lan, "Wave-packet initial motion, spreading, and energy in the periodically kicked pendulum," Phys. Rev. E **50**, 764 (1994).

23. Boris V. Chirikov, "The Problem of Quantum Chaos,"in Quantum Chaos: Proceedings of the Eighth Chris Engelbrecht Summer School on Theoretical Physics, Blydepoort, Eastern Transvaal, South Africa, 1324 January 1992,W.Dieter Heiss, Ed. (Springer- Verlag, Berlin, 1992).

24. P.W. Milonni, J.R. Ackerhalt, and H.W. Galbraith, "Chaos in the Semiclassical N-Atom Jaynes-CummingsModel: Failure of the Rotating-Wave Approximation," Phys. Rev. Lett. **50**, 966 (1983). Also **51**, 1108(E) (1983).

25. Fred Cooper, John F. Dawson, Dawn Meredith, and Harvey Shepard, “Semiquantum Chaos,” Phys. Rev. Lett. **72**, 1337 (1994).

26. R. Blümel and W.P. Reinhardt, “Chaos in Atomic Physics” (Cambridge University Press, 1997).

27. Lina E. Reichl, ”The Transition to Chaos”second edition Springer (2004).

28. A.J. Lichtenberg and M.A. Lieberman, “Regular and chaotic Dynamics” Springer-Verlag, New York (1992).

29. A.A. Chernikov, R.Z. Sagdeev, D.A. Usikov, M.Yu. Zakharov, and G.M. Zaslavsky, Nature **326**, 559 (1987).

30. F. Borgonovi and L. Rebuzzini, Phys. Rev. E **52**, 2302 (1995).

31. M. Frasca, Phys. Lett. A **231**, 344 (1997).

32. G.P. Berman, V.Yu. Rubaev, and G.M. Zaslavsky, Nonlinearity **4**, 543 (1991); T. Hogg and B.A. Huberman, Phys. Rev. A **28**, 28 (1983).

33. E.J. Galvez, B.E. Sauer, L. Moorman, P.M. Koch, and D. Richards, “Microwave Ionization of H Atoms: Breakdown of Classical Dynamics for High Frequencies,” Phys. Rev. Lett. **61**, 2011 (1988).

34. J.E. Bayfield, G. Casati, I. Guarneri, and D.W. Sokol, “Localization of Classically Chaotic Diffusion for Hydrogen Atoms in Microwave Fields,” Phys. Rev. Lett. **63**, 364 (1989).

35. Peter M. Koch, “Microwave ionization of excited hydrogen atoms: How nonclassical local stability brought about by scarred separatrix states is affected by broadband noise and by varying the pulse envelope,” Physica D **83**, 178 (1995).

36. R. Blümel and W.P. Reinhardt, Chaos in Atomic Physics (Cambridge University Press, Cambridge, 1997).

37. Peter M. Koch, “Experimental evidence for the influence of scars in hydrogen atoms driven by strong magnetic fields,” Chaos **2**, 131 (1992).

38. J.E. Bayfield, S.Y. Luie, L.C. Perotti and M.P. Skrzypkowski, “Ionization steps and phase-space metamorphoses in the pulsed microwave ionization of highly excited hydrogen atoms,” Phys. Rev. A **53**, R12 (1996).

39. Dominique Delande, “Chaos in Atomic and Molecular Physics,” in Chaos and Quantum Physics: Proceedings of the Les Houches Summer School, Session

LII, 131 August 1989, M.-J. Giannoni, A. Voros, and J. Zinn-Justin, Eds. (North-Holland, Amsterdam, 1991).

40. D. Delande, "Quantum Chaos in Atomic Physics," in Coherent Atomic Matter Waves: Proceedings of the Les Houches Summer School, Session LXXII, 27 July 27 August 1999, R. Kaiser, C. Westbrook, and F. David, Eds. (Springer-Verlag, Berlin, 2001).

41. U. Eichmann, K. Richter, D. Wintgen, and W. Sandner, "Scaled-Energy Spectroscopy and Its Relation with Periodic Orbits," Phys. Rev. Lett. **61**, 2438 (1988).

42. J. Main, G. Wiebusch, and K.H. Welge, "Spectroscopy of the classically chaotic hydrogen atom in magnetic fields," Comm. At. Mol. Phys. **25**, 233 (1991).

43. Martin C. Gutzwiller, Chaos in Classical and Quantum Mechanics (Springer- Verlag, New York, 1990).

44. H.-J. Stöckmann, Quantum Chaos: An Introduction (Cambridge University Press, Cambridge, 1999).

45. C.M. Marcus, A.J. Rimberg, R.M. Westervelt, P.F. Hopkins, and A.C. Gossard, "Conductance Fluctuations and Chaotic Scattering in Ballistic Microstructures," Phys. Rev. Lett. **69**, 506 (1992).

46. T.M. Fromhold, L. Eaves, F.W. Sheard, M.L. Leadbeater, T.J. Foster, and P.C. Main, "Magnetotunneling Spectroscopy of a Quantum Well in the Regime of Classical Chaos," Phys. Rev. Lett. **72**, 2608 (1994).

47. P.B. Wilkinson, T.M. Fromhold, L. Eaves, F.W. Sheard, N. Miura, and T. Takamasu, "Observation of scarred wavefunctions in a quantum well with chaotic electrons dynamics," Nature **380**, 608 (1996).

48. D. Weiss, M.L. Roukes, A. Menschig, P. Grambow, K. vonKlitzing, and G. Weimann, "Electron Pinball and Commensurate Orbits in a Periodic Array of Scatterers," Phys. Rev. Lett. **66**, 2790 (1991).

49. D. Weiss, K. Richter, A. Menschig, R. Bergmann,H. Schweizer, K. von Klitzing, and G. Weimann, "Quantized Periodic Orbits in Large Antidot Arrays," Phys. Rev. Lett. **70**, 4118 (1993).

50. M.F. Crommie, C.P. Lutz, D.M. Eigler, and E.J. Heller, "Quantum Corrals," Physica D **83**, 98 (1995).

51. H.-J. Stöckmann and J. Stein, " 'Quantum' Chaos in Billiards Studied by Microwave Absorption," Phys. Rev. Lett. **64**, 2215 (1990).

52. S. Sridhar, "Experimental observation of scarred eigenfunctions of chaotic microwave cavities," Phys. Rev. Lett. **67**, 785 (1991).

53. L. Sirko, Sz. Bauch, Y. Hlushchuk, P.M. Koch, R. Blümel, M. Barth, U. Kuhl, and H.-J. Stöckmann, "Observation of dynamical localization in a roughmicrowave cavity," Phys. Lett. A **266**, 331 (2000).

54. C. Dembowski, H.-D. Gräf, A. Heine, R. Hofferbert, H. Rehfeld, and A. Richter, "First Experimental Evidence for Chaos-Assisted Tunneling in a Microwave Annular Billiard," Phys. Rev. Lett. **84**, 867 (2000).

55. C. Dembowski, H.-D. Gräf, A. Heine, T. Hesse, H. Rehfeld, and A. Richter, "First Experimental Evidence of a Trace Formula for Billiard Systems Showing Mixed Dynamics,"Phys. Rev. Lett. **86**, 3284 (2001).

56. Claire Gmachl, Federico Capasso, E.E. Narimanov, Jens U. Nöckel, A. Douglas Stone, Jérôme Faist, Deborah L. Sivco, and Alfred Y. Cho, "High-Power Directional Emission from Microlasers with Chaotic Resonators," Science **280**, 1556 (1998).

57. C. Ellegaard, T. Guhr, K. Lindemann, H.Q. Lorensen, J. Nygård, and M. Oxborrow, "Spectral Statistics of Acoustic Resonances in Aluminum Blocks," Phys. Rev. Lett. **75**, 1546 (1995).

58. T. Neicu, K. Schaadt, and A. Kudrolli, "Spectral properties of amixed system using an acoustical resonator," Phys. Rev. E **63**, 026206 (2001).

59. R. Blümel, I.H. Davidson,W.P. Reinhardt, H. Lin, and M. Sharnoff,"Quasilinear ridge structures in water surface waves," Phys. Rev. A **45**, 2641 (1992).

60. A. Kudrolli, Mathew C. Abraham, and J.P. Gollub, "Scarred patterns in surface waves," Phys. Rev. E **63**, 026208 (2001).

61. P.A. Chinnery and V.F. Humphrey, "Experimental visualization of acoustic resonances within a stadium-shaped cavity," Phys. Rev. E **53**, 272 (1996).

62. Baruch Fischer, Amir Rosen, Alexander Bekker, and Shmuel Fishman, "Experimental observation of localization in the spatial frequency domain of a kicked optical system," Phys. Rev. E **61**, R4694 (2000).

63. Amir Rosen, Baruch Fischer, Alexander Bekker, and Shmuel Fishman, “Optical kicked system exhibiting localization in the spatial frequency domain, ” J. Opt. Soc. Am. B **17**, 1579 (2000).

64. F.L. Moore, J.C. Robinson, C.F. Bharucha, B. Sundaram, and M.G. Raizen, Phys. Rev. Lett. **75**, 4598 (1995).

65. C. Ryu, M.F. Andersen, A. Vaziri, M.B. d’Arcy, J.M. Grossman, K. Helmerson, and W.D. Phillips, Phys. Rev. Lett. **96**, 160403 (2006).

66. F.L. Moore, J.C. Robinson, C. Bharucha, P.E. Williams, and M.G. Raizen, Phys. Rev. Lett. **73**, 2974 (1994).

67. J. Ringot, P. Szriftgiser, J.C. Garreau, and D. Delande Phys. Rev. Lett. **85**, 2741 (2000).

68. H. Ammann, R. Gray, I. Shvarchuck, and N. Christensen, Phys. Rev. Lett. **80**, 4111 (1998).

69. G.J. Duffy, S. Parkins, T. Müller, M. Sadgrove, R. Leonhardt, and A.C. Wilson, Phys. Rev. E. **70**, 056206 (2004).

70. M.K. Oberthaler, R.M. Godum, M.B. D’Arcy, G.S. Summy, and K. Burnett, Phys. Rev. Lett. **83**, 4447 (1999).

71. M.B. dArcy, R.M. Godun, D. Cassettari, and G.S. Summy, Phys. Rev. A **67**, 023605 (2003).

72. S. Schlunk, M.B. dArcy, S.A. Gardiner, and G.S. Summy, Phys. Rev. Lett. **90**, 124102 (2003).

73. R.M. Godun, M.B. D’Arcy, M.K. Oberthaler, G.S. Summy, and K. Burnett, Phys. Rev. A **64**, 013411 (2000).

74. R.M. Godun, M.B. d’Arcy, and G.S. Summy, K. Burnet Contemporary Physics **42**, 77 (2001).

75. M.B. d’Arcy, R.M. Godun, G.S. Summy, I. Guarneri, S. Wimberger, S. Fishman, and A. Buchleitner, Phys. Rev. E **69**, 027201, (2004).

76. Shmuel Fishman, Italo Guarneri, and Laura Rebuzzini, J. Stat. Phys. **1**10, 911 (2003); Shmuel Fishman, Italo Guarneri, and Laura Rebuzzini Phys. Rev. Lett. **89**, 084101 (2002).

77. P. Ahmadi, B.P. Timmons, and G.S. Summy, Phys. Rev. A **72**, 023411 (2005).

78. M.H. Anderson, J.R. Ensher, M.R. Matthews, C.E. Wieman and E.A. Cornell, Science **269** 198 (1995).

79. K.B. Davis, M.-O. Mewes, M.R. Andrews, N.J. Van Druten, D.S. Durfee, D.M. Kurn, and W. Ketterle, Phys. Rev. Lett. **75** 3969 (1995).

80. W.D. Phillips, Rev. Mod. Phys. **70** 721 (1998).

81. E.A. Cornell and C. Weiman, Rev. Mod. Phys. **74** 875 (2002).

82. Paul D. Lett, Richard N. Watts, Christoph I. Westbrook, and William D. Phillips, Phys. Rev. Lett. **61** 169 (1988).

83. A. Aspect, E. Arimondo*, R. Kaiser, N. Vansteenkiste, and C. Cohen-Tannoudji, Phys. Rev. Lett. **61** 826 (1988).

84. M. Kasevich and S. Chu, Phys. Rev. Lett. **69** 1741 (1992).

85. Andrew J. Kerman, Vladan Vuletic, Cheng Chin, and Steven Chu, Phys. Rev. Lett. **84** 439 (2000).

86. Dian-Jiun Han, Steffen Wolf, Steven Oliver, Colin McCormick, Marshall T. DePue, and David S. Weiss, Phys. Rev. Lett. **85** 724 (2000).

87. Charles S. Adams, Heun Jin Lee, Nir Davidson, Mark Kasevich, and Steven Chu, Phys. Rev. Lett. **74** 3577 (1995).

88. K.M. O'Hara, M.E. Gehm, S.R. Granade, S. Bali, and J.E. Thomas, Phys. Rev. Lett. **85** 2092 (2000).

89. H. Engler, T. Weber, M. Mudrich, R. Grimm, and M. Weidemller, Phys. Rev. A. **62** 031402(R) (2000).

90. Tetsuya Ido, Yoshitomo Isoya, and Hidetoshi Katori, Phys. Rev. A. **61** 061403(R) (2000).

91. D.J. Han, Marshall T. DePue, and David S. Weiss, Phys. Rev. A. **63** 023405 (2001).

92. D.M. Stamper-Kurn, H.-J. Miesner, A.P. Chikkatur, S. Inouye, J. Stenger, and W. Ketterle, Phys. Rev. Lett. **81** 2194 (1998).

93. D.M. Stamper-Kurn, M.R. Andrews, A.P. Chikkatur, S. Inouye, H.-J. Miesner, J. Stenger, and W. Ketterle, Phys. Rev. Lett. **80** 2027 (1998).

94. H.-J. Miesner, D.M. Stamper-Kurn, J. Stenger, S. Inouye, A.P. Chikkatur, and W. Ketterle, Phys. Rev. Lett. **82** 2228 (1999).

95. D.M. Stamper-Kurn, H.-J. Miesner, A.P. Chikkatur, S. Inouye, J. Stenger, and W. Ketterle, Phys. Rev. Lett. **83** 661 (1999).

96. B.P. Anderson and M.A. Kasevich, Science **282** 1686 (1998).

97. M.D. Barrett, J.A. Sauer, and M.S. Chapman, Phys. Rev. Lett. **87** 010404 (2001).

98. Tino Weber, Jens Herbig, Michael Mark, Hanns-Christoph Nägerl, Rudolf Grimm, Science **299** 232 (2003).

99. Toshiya Kinoshita, Trevore Wenger, and David S. Weiss, Phys. Rev. A. **71** 011602(R) (2005).

100. Peyman Ahmadi,*Investigating Optical Atom Traps For Bose-Einstein Condensate*,Doctoral dissertaion, Oklahoma State University (2006)

101. S.N. Bose, Z. Phys. **26**, 178 (1924).

102. A. Einstein, Stizber.Kgl. Preuss. Akad. Wiss. 261 (1924).

103. A. Einstein, Stizber. Kgl. Preuss. Akad. Wiss. 3 (1925).

104. P. Lebedev, Ann. Phys. (Leipzig) **6**, 433 (1901).

105. E.F. Nichols, and G.F. Hul, "A preliminary communication on the pressure of heat and light radiation," Phys. Rev. **1**7, 26 1903.

106. R. Frisch, "Experimenteller Nachweis des Einstenschen Strahlungsru ckstosses," Z. Phys. **8**6, 42 1933.

107. A. Ashkin, "Atomic-beam deflection by resonance radiation pressure," Phys. Rev. Lett. **2**5, 1321 1970.

108. G.A. Askar'yan, "Effects of the gradient of a strong electromagnetic beam on electrons and atoms," Sov. Phys. JETP **15**, 1088 1962.

109. V. Letokhov, "Narrowing of the Doppler width in a standing light wave," Pis'ma Zh. Eksp. Teor. Fiz. 7, 348, JETP Lett. **7**, 272 (1968).

110. T. Hänsch, and A. Schawlow, "Cooling of gases by laser radiation," Opt. Commun. **1**3, 68 1975.

111.D. Wineland, and H. Dehmelt, "Proposed $10^{14}\Delta\nu < \nu$ laser fluorescence spectroscopy on TI† mono-ion oscillator III," Bull. Am. Phys. Soc. **2**0, 637 1975.

112.A. Ashkin, "Trapping of atoms by resonance radiation pressure," Phys. Rev. Lett. **4**0, 729 1978.

113.H.J. Metcalf and P. van der Straten. Laser Cooling and Trapping. Springer-Verlag, New York (1999).

114.W.D. Phillips. Laser Cooling and Trapping of Neutral Atoms. Noble Lecture, December 8, (1997).

115.H. Hess, Bull. Am. Physc. Soc. **30** 854 (1985).

116.H.F. Hess, Phys. Rev. B. **34** 3476 (1986).

117.H. Hess, G.P. Kochanski, M.J. Doyle, N. Masuhara, D. Kleppner, and T. Greytak, Phys. Rev. Lett. **59** 672 (1987).

118.W. Petrich, M.H. Anderson, J.R. Ensher, and E.A. Cornell, "Fortheenth International Conference on Atomic Physics", Boulder, Colorado, 1994, Book of Abstracts, 1m-7.

119.C.C. Bradly, C.A. Sackett, J.J. Tollet, and R.G. Hulet, Phys. Rev. Lett. **75** 1686 (1995).

120.K.B. Davis, M.-o. Mewes, M.A. Joffe, M.R. Andrews, and W. Ketterle, Phys. Rev. Lett. **74** 5202 (1995).

121.S. Chu, J.E. Bjorkholm, A. Ashkin, and A. Cable, Phys. Rev. Lett. **57** 314 (1986).

122.J.D. Miller, R.A. Cline, and D.J. Heizen, Phys. Rev. A. **47** R4567 (1993).

123.J.M. Doyle, J.C. Sandberg, I.A. Yu, C.L. Cesar, D. Kellepner, and T.J. Greytak, Phys. Rev. Lett. **67** 603 (1991).

124.J.M. Doyle, J.C. Sandberg, I.A. Yu, C.L. Cesar, D. Kellepner, and T.J. Greytak, Phys. B. **13** 194 (1994).

125.K.B. Davis, M.O. Mewes, and W. Ketterle, Appl. Phys. B. **60** 155 (1995).

126.M. Holland, J. Williams, K. Coakley and J. Cooper, Quantum Semiclass. Op. **8** 571 (1996).

127.H. Wu, C.J. Foot, J. Phys. B. **29**, L321 (1996).

128.K.M. O'Hara, M.E. Gehm, S.R. Granade, and J.E. Thomas, Phys. Rev. A. **64**, 051403(R) (2001).

129.S. Friebel, C. D'Andrea, J. Walz, M. Weitz, and T.W. Hänsch, Phys. Rev. A. **57** R20 (1998).

130.Y. Takasu, K. Maki, K. Komori, T. Takano, K. Honda, M. Kumakura, T. Yabuzaki, and Y. Takahashi, Phys. Rev. Lett. **91** 040404 (2003).

131.S.R. Granade, M.E. Gehm, K.M. O'Hara, and J.E. Thomas, Phys. Rev. Lett. **88** 120405 (2002).

132.G. Cennini, G. Ritt, C. Geckeler, and M. Weitz, Phys. Rev. Lett. **91** 240408 (2003).

133.K.M. O'Hara, S.R. Granade, M.E. Gehm, and J.E. Thomas, Phys. Rev. A. **63** 043403 (2002).

134.N. Friedman, L. Khaykovich, R. Ozeri, and N. Davidson, Phys. Rev. A. **61** 031403(R) (2000).

135.V. Milner, J.L. Hanssen, W.C. Campbell, and M.G. Raizen Phys. Rev. Lett. **86** 1514 (2001).

136.O. Svelto, Principles of Lasers, fourth ed. (Springer, New York, 1998).

137.G. Cennini, G. Ritt, C. Geckeler, and M. Weitz, Phys. Rev. Lett. **91**, 240408 (2003).

138.G. Behinaein, V. Ramareddy, P. Ahmadi, and G.S. Summy, Phys. Rev. Lett. **97**, 244101 (2006).

139.A.J. Lichtenberg and M.A. Lieberman, Regular and Stochastic Motion (Springer-Verlag, New York, Heidelberg, Berlin, 1983).

140.W.H. Oskay, D.A. Steck, V. Milner, B.G. Klappuf, M.G. Raizen, Opt. Comm. **179**, 137 (2000).

141.M. Sadgrove, S. Wimberger, S. Parkins, and R. Leonhardt, Phys. Rev. Lett. **94**, 174103 (2005).

142.A. Buchleitner, M.B. d'Arcy, S. Fishman, S.A. Gardiner, I. Guarneri, Z.-Y. Ma, L. Rebuzzini, G.S. Summy, Phys. Rev. Lett. **96**, 164101 (2006).

143.M.B. d'Arcy, R.M. Godun, D. Cassettari, and G.S. Summy, Phys. Rev. A **67**, 023605 (2003).

144.L. Deng, E.W. Hagley, J. Denschlag, J.E. Simsarian, Mark Edwards, Charles W. Clark, K. Helmerson, S.L. Rolston, and W.D. Phillips, Phys. Rev. Lett. **83**, 5407 (1999).

145.S.A. Gardiner, D. Jaksch, R. Dum, J.I. Cirac, and P. Zoller, Phys. Rev. A **62**, 023612 (2000).

146.G.J. Duffy, A.S. Mellish, K.J. Challis, and A.C. Wilson, Phys. Rev. A **70**, 041602(R) (2004).

147.W.K. Hensinger *et al.*, Nature **412**, 52 (2001).

148.D.A. Steck, W.H. Oskay, and M.G. Raizen, Science **293**, 274 (2001).

VITA

GHAZAL BEHIN AEIN

Candidate for the Degree of

Doctor of Philosophy

Thesis: Quantum chaos with a Bose-Einstein condensate

Major Field: Physics

Biographical:

Personal Data:Born in Shiraz, Iran, on July 23, 1971, the daughter of Noreddin and Masoomeh Behinaein.

Education:Graduated from Somayeh High School, Shiraz, Iran in May 1987; received Bachelor of Science degree in Physics from Shiraz University, Shiraz, Iran in May 1996. Completed the requirements for the Doctor of Philosophy degree with a major in Physics at Oklahoma State University in July 2007.

Professional Memberships:American Physical Society.

Name: Ghazal Behin Aein Date of Degree: July, 2007

Institution: Oklahoma State University Location: Stillwater, Oklahoma

Title of Study: Quantum chaos experiments with a Bose-Einstein condensate

Pages in Study: 106 Candidate for the Degree of Doctor of Philosophy

Major Field: Physics

Scope and Method of Study:The purpose of this research was to experimentally study a quantum delta-kicked accelerator utilizing a Bose Einstein condensate (BEC) of Rb87 atoms. An all optical method was chosen to create a BEC. Generalization of the quantum theory of the quantum accelerator modes to include the higher order QAM's observed in cold atomic systems was also among the topics studied in this research.

Findings and Conclusions:The underlying pseudoclassical phase space structure of the quantum delta-kicked accelerator was experimentally explored. This was achieved by exposing a Bose-Einstein condensate to a spatially corrugated potential created by pulses of an off-resonant standing light wave. For the first time quantum accelerator modes were realized in such a system. By utilizing the narrow momentum distribution of the condensate the discrete momentum state structure of a quantum accelerator mode was observed. These experiments allowed us to directly measure the size of the structures in the phase space of the delta-kicked accelerator.

We also found that the phase space structures in the pseudoclassical model are given by the interference of the different momentum diffraction orders of the matter wave from standing light waves. This discovery allowed us to generalize the quantum theory of accelerator modes to explain higher order accelerator modes observed in cold atomic systems.

ADVISOR'S APPROVAL Dr. Gil Summy